CONTROL OF FLUCTUATING RENEWABLE ENERGY SOURCES: ENERGY QUALITY & ENERGY FILTERS

by

YAN, ZUANHONG

A thesis submitted to

The University of Birmingham

for the degree of

DOCTOR OF PHILOSOPHY

Department of EESE,

School of Engineering

The University of Birmingham

Feb 2018

Dedicated to

My Wife, Sze Yau Wong

My Mother, Caiyun Wang

and

My first child

ABSTRACT

This doctoral study discusses how to control fluctuating renewable energy sources at converter, unit, and system layers to deliver smoothed power output to the grid. This is particularly relevant to renewable power generation since the output power of many kinds of renewable energy sources have huge fluctuations (e.g. solar, wind and wave) that needs to be properly treated for grid integration. In this research, the energy quality is developed to describe the friendliness and compatibility of power flows/waveforms to the grid, by contrast with the well-known concept of power quality which is used to assess the voltage and current waveforms.

In Chapter 1&2, a background introduction and a literature review of studied subjects are presented, respectively. In Chapter 3, the problem of determining the PI parameters in dq decoupling control of voltage-source converter (VSC) is studied based on a state-space model. The problems of the conventional method when there is insufficient interface resistance are addressed. New methods are proposed to overcome these drawbacks. In Chapter 4&5, energy quality and the energy filters (EFs) are proposed as tools to assess and manage power fluctuations of renewable energy sources. The proposed EFs are energy storage control systems that could be implemented on a variety of energy storage hardware. EFs behave like low-pass filters to the power flows. Finally, in Chapter 6, as an application example of renewable power plant with energy filter control and smoothed power output, a master-slave wave farm system is proposed. The wave farm system uses enlarged rotor inertia of electric machines as self-energy storage devices.

ACKNOWLEDGEMENT

I would like to express my deep appreciation and gratitude to my supervisor Prof. Xiao-Ping Zhang for his invaluable helps, supports and guidance during my PhD study.

I want to thank my wife for her everlasting love, support and being with me in the hard days. I also want to thank my mother for her love, financial support and much more beyond through these years.

I want to thank my colleagues and friends in my research group for all the helpful and inspiring discussions. I want to particularly mention the following names: Zhao Xianxian, Xue Ying, Yang Conghuan, Guan Rui, and Wang Puyu. Thank you.

Finally, my gratitude goes to Mr. Richard Baines, whose efforts of proofreading this thesis improve its readability. This thesis was also partly copy edited for conventions of language, spelling and grammar by Janet's Proofreading Service.

CONTENTS

LIST OF FIGURES

LIST OF TABLES

LIST OF ABBREVIATION

AWS	Archimedes wave swing
BESS	battery energy storage system
CAES	compressed air energy storage
DFIG	doubly-fed induction generator
EES	electrical energy storage
FES	flywheel energy storage
EF	energy filter
SEF	series energy filter
PEF	parallel energy filter
HEF	hybrid energy filter
HVDC	high voltage direct current
HTS	high-temperature superconducting
IM	induction machine
LVRT/FRT	low voltage ride-through/ fault ride-through
LPF	low-pass filter
MPPT	maximum power point tracking
MAF	moving average filter
MTDC	multi-terminal DC (grid)
OWC	oscillating wave column
PCC	point of common coupling
PMLG	permanent magnet linear generator
PMSG/PMSM	permanent magnet synchronous generator/machine
PHS	pumped-hydro storage

PSO	particle swarm optimization
PTO	power take-off
RTDS	real-time digital simulator
SMES	superconducting magnetic energy storage
SoC	state of charge
TES	thermal energy storage
TPHD	total power harmonic distortion
VSC	voltage source converter
WEC	wave energy conversion

CHAPTER 1 INTRODUCTION

Abstract- This chapter presents a background introduction of the integration and control of fluctuating renewable energy sources and its relationship with electrical energy storage. The research motivations and objectives are stated. At the end of the chapter, the structure of the whole thesis is outlined.

1.1 Research Backgrounds and Motivations

1.1.1 Roles of Renewable Energy Sources in a Global View

Global power generation is experiencing a grand transformation from a conventional profile, in which the fossil fuel take the majority, to a multi-source profile, in which a variety of power sources make significant contributions, and renewable energy plays an especially important role. According to Bloomberg New Energy Finance's long-term economic forecast of the world's power sector [1], to 2040, renewable energy sources will take over 50% of global electricity generation, in which solar and wind will take 34%. For this reason, increasing interest, from both academia and industry, is focused on the study of the problems in developing renewable energy sources. Despite efforts for several decades, this topic is still far from being fully discussed.

Fossil fuels are not sustainable, mainly, for two reasons. First, reserves are limited and will become uneconomic to recover and use. Secondly, CO_2 emitted by burning fossil fuels is a significant cause for global warming and climate change. This problem is recognized as a critical global challenge to human beings by most of the countries in the world. International

efforts have been made and a variety of legal documents have been signed to set objectives for the reduction of CO_2 emissions.

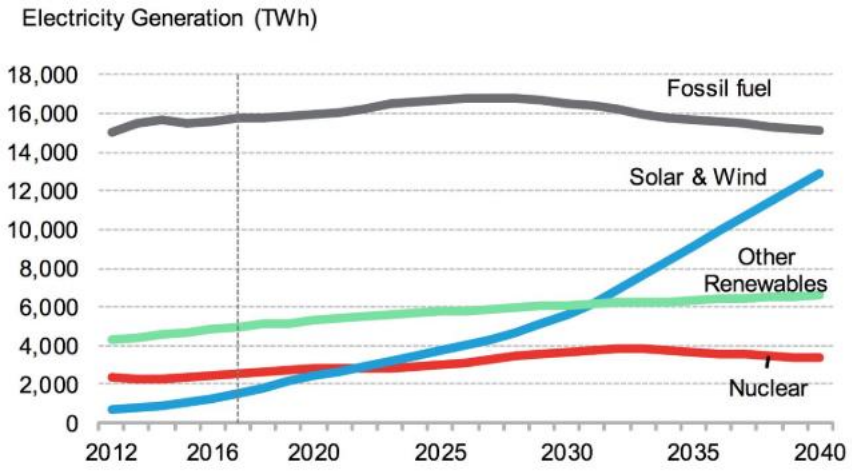

Fig. 1.1 Global electricity generation mix to 2040 [1]

Non-fossil fuel energy sources mainly consist of nuclear and renewable energy. The former can be classified into two groups: fission and fusion energy. Fission energy has already been well commercially utilized for power generation and is also a promising contributor to future power generation. However, fission power generation suffers three drawbacks: 1) like fossil fuels, nuclear fuel resources are limited, on Earth; 2) nuclear waste disposal is problematic, and; 3) the public is concerned about security, causing political obstacles to its development. Fusion energy is widely considered as the "ultimate solution" of the power supply, however, current developments in fusion power generation are still very far from any commercial application. Consequently, power generation is based on multiple sources, including conventional and advanced fossil fuel generation, fission nuclear power, and a variety of renewable power sources.

1.1.2 Fluctuating Renewable Energy Sources

In this study, an energy source is called **variant** if the raw power to be transferred into electricity is variable and uncontrollable. This change of the prime mover power is called **variation**, which involves two aspects: **fluctuation** and **intermittency**. Briefly speaking, fluctuation is a short-term power variation, while intermittency is the long-term variation and availability.

Mainstream renewable energy consists of the following six types: solar, wind, ocean power (in which the wave and tidal power takes the majority), hydropower, geothermal, and biomass/biofuel. In this doctoral study, the focus is on fluctuating renewable energy including the solar, wind and wave. Tidal power is intermittent but not fluctuating and all the rest are stable and controllable power sources without variation.

The increasing penetration of fluctuating renewables and consequent injection of fluctuating power to the grid raises many problems that must be properly handled. It causes frequency variations, voltage flickers, thermal excursions and the over-rating of electrical devices. These problems are becoming worse in a weak grid with increased use of renewable energy sources. To remove these technical obstacles to the development of fluctuating renewable energy, electrical energy storage (EES) technologies are more and more frequently studied and used. These studies are still insufficient for the complex scenarios of fluctuating energy sources and current implementation has been at a small scales and an early stage.

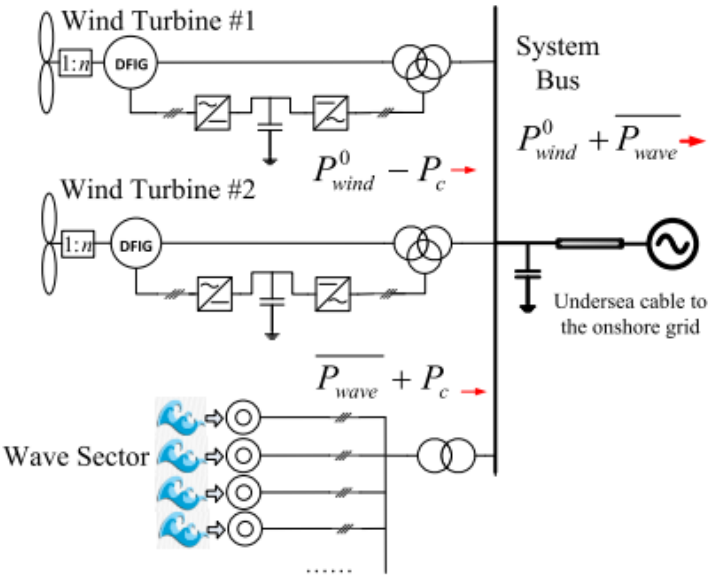

Fig. 1.2 A wind-wave farm with a large number of renewable power generation units

With the purpose of increasing the power capacity, the overall system efficiency and to decrease the capital cost, it is becoming popular to build renewable power generation in a large system with many single power generation units. This is called a farm, power plant or power station in different contexts (e.g. wind farm, wind power plant, wave farm, solar farm). An example of such a system is presented in Fig. 1.2. In such a renewable power plant, the controls are performed in three different layers, which are: the converter, the unit, and the system layer, as follows.

At the converter layer, the primary control objective is to either 1) make the real and reactive power (P&Q) of the converter track the power references or 2) regulate the AC frequency and voltage at the point of common coupling according to the control references given by the unit layer control. The latter one is more usual in grid-side converters.

At the unit layer, the control objective is to operate each one of the single power generation units optimally, for example, to maximize the raw power captured by controlling torque, speed, real or reactive power at the primary side. The references determined at this layer would be used in the converter control as discussed above. The quality of the output power, on a single-unit basis, also needs to be controlled at this layer.

At the system layer, the co-ordination of multiple power generation units, the power quality and the external characteristics of the whole plant are to be considered. Besides the power generation units, a renewable power plant could include auxiliary devices such as EES, fault ride through (FRT) devices and reactive power compensators to improve the overall performances of the system, and the operation of these auxiliary devices is also part of the system layer control.

There are problems worth studying in any of these three layers, especially in an EES-integrated system. A review of these problems is presented in Chapter 2.

1.1.3 EES Systems for the Grid-integration of Fluctuating Renewable Energy Sources

As has been mentioned, electrical energy storage (EES) is a promising solution for the integration of fluctuating renewables. It could be used for frequency and voltage support, power smoothing, and FRT support. The state-of-the-art EES technologies could be classified into six groups according to the forms of the stored energy: potential mechanical, chemical, thermal, kinetic mechanical, electrochemical, and electric-magnetic field storage. In this research, they are further classified into two families: light-storage and heavy-storage.

Light-storage includes flywheel energy storage systems (FESS), electric-magnetic field storage such as the supercapacitor and superconducting magnetic energy storage (SMES), and a group of high-efficiency small-scale batteries. Generally speaking, light-storage is relatively small-scaled but with high cycle efficiency, which is defined as the ratio of the whole electric power output to the input, and fast response. Its typical power capacity is 0.1-10 MW and the discharging time at the rated power is from seconds to no more than 1 hour. The cycle efficiency of light-storage could be over 90%, and the response time is from milliseconds to no more than one synchronous period of the grid. However, most light-storage, except batteries, suffers the drawback of large self-discharge [36], which limits their potentials in long-term applications. Due to these characteristics, light-storage is more suitable for short-term applications that require smaller capacity but fast response and high efficiency, such as power quality support, ride through capability, and bridging power supply.

Heavy-storage includes mechanical potential storage (e.g. pumped-hydro storage PHS, under sea storage or compressed air energy storage CAES), chemical storage (e.g. hydrogen storage, for fuel cells), thermal energy storage (TES), and a package of utility-scale batteries including flow batteries. Heavy-storage can be arranged at scale for long-term applications, and its self-discharge is very low to almost zero. Its power capacity is from several MWs to over 100 MW, and the typical discharging time at the rated power is from hours to one day. The drawbacks of heavy-storage are its low round-trip efficiency and slow response. The typical efficiency is from about 50% (for CAES, TES or hydrogen fuel cells) to no more than 85% (PHS), and the response time is between seconds and minutes. Besides, it is inconvenient for some kinds of the heavy-storage to interact with the electrical system with bi-directional power flow. For example, in CAES, fuel cells and most TES, the charging and

discharging processes are achieved by different and separated energy conversion devices. For these reasons, heavy-storage is more suitable for long-term and large scale applications such as time shifting, load levelling, black-start for nuclear units, and standing reserve.

It is acknowledged that there is no strict distinction between light- and heavy-storage and these two EES families overlap in their middle-range. For example, the Li-ion battery could be regarded as either a light- or heavy-storage device, depending on its power and energy capacity, which actually enjoys the advantages of both families. Yet still, this classification is useful in these discussions of the fluctuation and intermittency of renewable energy. In Chapters 5 & 6, a more detailed discussion reveals that light-storage is suitable, in a renewable power plant, for handling fluctuation, while heavy-storage is suitable for intermittency.

1.2 Research Objectives

This doctoral study considers the EES-integrated variant renewable power plant and alleviation of the problems caused by the fluctuating power flows of renewable energy sources and aims to facilitate large scale renewable power generation in the future. This work is to study and provide solutions to the control and grid-integration of a fluctuating renewable power plant in three layers, as discussed below.

In the converter layer, this research is to investigate how to determine the PI control parameters in the widely used dq decoupling control of VSC with sufficient mathematical insights based on a state-space model.

In the unit layer, the integration and control methods of EES are to be studied with the purpose of suppressing short-term power fluctuations. A family of EES control system called the energy filter is proposed, which virtually works as low-pass filters of power flows.

In the system layer, rather than a simple combination of power generation units, a fluctuating renewable power plant is supposed to be a whole system with its own external characteristics for the grid. Wind and solar farms have already been commercially developed but very limited work has been done on developing a wave farm with EES integration. It is also proposed to study the value of energy filter control on wave farms.

1.3 Outline

The outline of this thesis is arranged as follows. The literature review is given in **Chapter 2**. **Chapter 3** studies different methods of PI parameters determination in the dq decoupling control of VSC converters. This knowledge lays the foundation of the renewable power generation and control.

Chapter 4 discusses the characteristics of the typical time series of solar, wind and wave power generation without integrated EES in terms of their fluctuation and intermittency. Based on these observations, the conventional concept of power quality used to describe voltage and current waveforms is generalized to the concept of energy quality to describe the waveform of a variant power flow. This is a precursor to Chapter 5.

Chapter 5 proposes the Energy Filter (EF), which is an EES control system for short-term energy quality control and that could be implemented based on a variety of light-storage systems. Case studies of the EF are presented for different applications.

Chapter 6 proposes a wave farm system with a master-slave structure based on the knowledge developed in previous chapters. The control methods of the proposed system are discussed comparatively and system simulations are presented.

Chapter 7 concludes this research, highlights the contributions and indicates the extent of work that could be conducted in the future.

CHAPTER 2 LITERATURE REVIEW

Abstract- This chapter presents the background knowledge and literature review of the subjects covered in this research. Firstly, previous studies are reviewed for the discussion of the determination of PI parameters, in Chapter 3. Secondly, the mainstream electrical energy storage (EES) systems and the power smoothing control methods are reviewed in preparation for the development of the Energy Filter in Chapter 5. Finally, studies of wave power generation are reviewed in preparation for Chapter 6.

2.1 PI Parameters in Controllers of VSC

VSC-based power electronics are more and more popular in a smart grid preparing for the future. They are widely used in DFIG systems, VSC HVDC, back-to-back converters, STATCOM, etc. [2-3][26]. Dq decoupling controls are commonly used in these devices, which are based on the dynamic model of VSC and can control the real and reactive power independently. The stability and performances of a dq decoupling controller largely depends on the parameters of PI controllers in the control loops as shown in Fig. 2.1. For this reason, the determination of PI parameters is a significant problem, which demands the determination of the proportional and integral gains of the PI controllers to achieve the desirable performance [4].

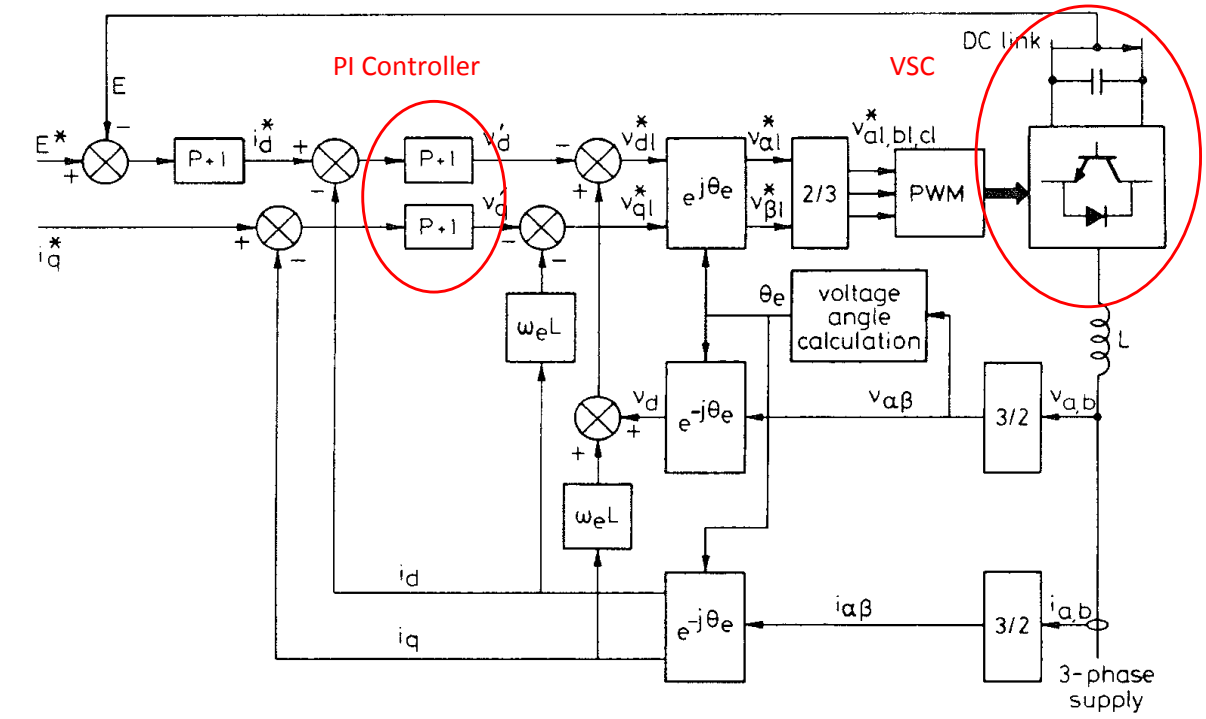

Fig. 2.1 A typical control system of VSC and the PI controllers in the inner loop [3]

There are two solutions to this problem. One is PI tuning, which dates back to a comparative study in 1995 [5] of the gain and phase margins of nine well-known PI tuning methods at that time. For the latest studies in this area from the control community, [6] proposed a new adaptive GSA-based tuning method to optimize the PI controllers for servo systems with reduced parametric sensitivity and improved stability and robustness. [7] proposed a self-tuning method for fuzzy PI controllers. Other PI tuning methods include the multi-objective optimisation of PI tuning [8] and the particle swarm optimization (PSO) method [9], which is later applied to the optimum design of VSC-based HVDC system [10]. However, these control theories are seldom directly applied to the VSC controls because, in such engineering problems, the assumptions made in the development of control theories are usually no longer

applicable. Methods developed specially for the VSC system control include: the PSO tuning method for DC voltage control of grid-connected solar PV systems [11]; the PSO-based on-line tuning method for the PI controller of induction-motor drive [12] and the linearized biogeography-based tuning method for direct-drive PMSG wind generation systems [13]. The distinctive advantage of PI tuning is that it does not need all the information of the controlled plant. The tuning process must, however, be implemented on a trial-and-error basis, which could be time consuming and costly and there is a lack of insight into the controlled plant in these methods.

Another solution is the PI parameters calculation. Unlike PI tuning, which does not need to know all of the plant information, this method calculates the PI parameters according to the plant parameters and the given control objectives. When the all plant information is known, in comparison with PI tuning, the PI parameters calculation is more desirable because the control objectives could be more accurately achieved and it presents more insights into the control system. The zero-pole cancelling method has been widely used, recently, to calculate PI parameters, which have been used on an MTDC grid [14-16] and energy storage systems based on VSC [17-19]. However, the risk of a cancelled pole, in this method, has never been addressed with sufficient theoretical analysis. This risk together with the instability problem raised when there is insufficient interface resistance of the VSC is studied in Chapter 3.

2.2 EES for Smoothing the Fluctuating Renewable Power

2.2.1 Long-term and Short-term Variations of Renewable Power

Most renewable power generation units want to transfer as much of their raw power, as can

be harnessed, into electricity. For this reason, the electrical power output of these units cannot be arbitrarily controlled but depends on the real-time strength of the variant natural resources, which are intermittent and fluctuating. This is the distinctive difference between renewable and traditional power plants. Variations in renewable power are both short-term (seconds to minutes) and long-term (hours to days). Long-term power variation and availability is called the intermittency, which is the variation of the average power level through hours and days. In previous studies [20-22], the problems of secondary frequency regulation, caused by renewable power intermittency, and power balance methods using electrical energy storage (EES) have been discussed. Short-term power variation is called fluctuation, which is the real-time variation of power flows in short times, i.e. from seconds to minutes. Wave power is a good example, emphasising the difference between power intermittency and fluctuation. Wave power fluctuation is huge (0-2.0 per unit, period 5-12s), although long-term average wave power is more available and predictable than solar and wind energy [23]. The power fluctuation raises problems of voltage flicker, thermal excursions, primary frequency regulations, and wasted equipment capacities in PV [24] and wave generation [25] systems. It is desirable to eliminate or suppress power fluctuations at the point of common coupling (PCC). There are also power fluctuations on the load side when the loads are pulsating. For example, in microgrids, distributed renewable generation could be operated in parallel with pulsating loads [27]. In the above systems, especially when the local grid is weak, it is desirable to eliminate or suppress power fluctuations on the load side.

2.2.2 Controls of EES to Smooth Power Fluctuation

Control systems of electrical energy storage (EES) are useful tools to manage power

fluctuation on both the generation and load sides. Many papers have studied the control of EES. This topic has two branches: one is about how to control the output power of an EES system; to track a given reference, and a variety of methods have been comparatively studied [28]; Another branch of this topic, which is more complicated and important, is about how to determine the control reference. This problem is usually treated as a multiple-objective optimization problem in long-term applications. A mixed-integer-linear program method is proposed to optimize the hourly operations of EESs in [20]. This method is also used to minimize the energy cost and optimize the operations of EES-integrated microgrids [21]. A semi-Markov model is proposed, to predict the solar power variation in a day, to optimize the EES control. However, these long-term optimization methods do not concern the real-time control of EES to eliminate or suppress the power fluctuation.

For short-term applications, real and reactive power are controlled in real-time. An adaptive control of superconducting magnetic energy storage (SMES) [29], a battery energy storage system (BESS) under fuzzy neural network control [30] and a self-inertia control of the DFIG using DC capacitor storage [31] are proposed to smooth the output power of wind farms. In [32], short-term EES control is studied; to improve the FRT capability of wind farms based on SMES. A model predictive control of BESS is proposed to smooth power fluctuation in the electrical power system of ships [33]. Control of a supercapacitor-based EES, to smooth marine current generation [34], is studied. The charging stations of electric vehicles are used to smooth the power fluctuation in the local grid [35].

2.2.3 Flywheel Storage Systems, Lithium-ion Batteries, Supercapacitors and SMES

Implementation of any grid-side power control method must be based on a specific kind of energy storage system. Until recently, the mainstream EES systems include: pumped-hydro storage, compressed air energy storage, liquid air energy storage, thermal energy storage, flywheel energy storage (FES), Li-ion batteries, flow batteries, a pack of conventional batteries (lead-acid, NiCd, NiMH, etc.), high-temperature batteries (NaS, ZEBRA), capacitors and supercapacitors, superconducting magnetic energy storage system (SMES), fuel cells and other chemical energy storage [36]. This thesis focuses on three of them: FES, Li-ion batteries, and supercapacitors because their fast response and high round-trip efficiency makes them suitable for short-term power smoothing and, therefore, compatible for the energy filters proposed in Chapter 5.

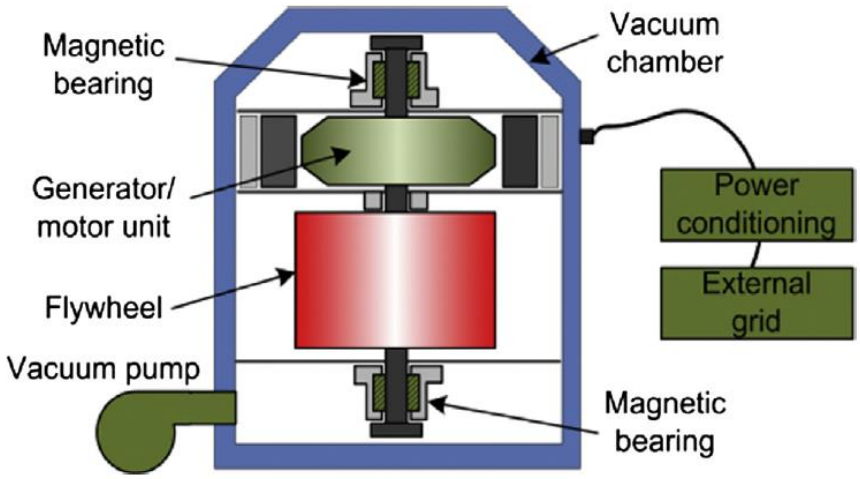

Fig. 2.2 Main structure of a flywheel energy storage system [36]

A modern FES system consists of 5 parts: a flywheel, a vacuum chamber, a bearing system, a generator, and a power converter as shown in Fig. 2.2. FES systems can be classified into two groups: low-speed FES rotating below 6,000 rpm usually using steels, and high-speed FES rotating at up to ~10^5 rpm using advanced materials such as carbon fibre. For FES system,

the rated power is 0.1-20 MW [37][38], and the rated energy capacity is from 5.0 kWh [37] up to 5.0 MWh [38]. Accordingly, the rated discharging time is 1-15 minutes. Its round-trip efficiency, defined as the ratio of the total power output over the input is 90%-95% [39], and the response time is smaller than one synchronous period (20ms) [40].

Through global investments and research efforts, Li-ion batteries are becoming superior over other EES technologies, not only due to their high efficiency and fast response, but also because they can be made in large and even at utility-scale for long-term storage applications. Li-ion batteries use lithium metal oxide as the cathode and graphitic carbon as the anode in which the Li atoms are stored. The electrolyte is usually made of organic liquid with lithium salts to transport the ions, and, in the latest research, progresses has been made on the development of Li-ion batteries with solid state electrolyte to further increase the energy density and improve safety [41]. Power converters are commonly used in Li-ion BESS to control power flow, DC voltage levels and for DC-AC conversion. For Li-ion batteries, the rated power is from small scale, 5.0 kW, to a utility-scale, up to 100MW [42][43]. The rated energy capacity is 0.004-10 MWh [43][44]. The rated discharge-time is usually no more than one hour. Compared with other batteries, the Li-ion batteries have a much higher round-trip efficiency of 90%-97% [45]. The response time of Li-ion BESS is smaller than 5ms [46].

Supercapacitors, also named as ultracapacitors, are made in an electric double-layer structure to significantly increase their capacitance. Like BESS, power converters are commonly used in supercapacitor-based storage systems and DC-DC converters are used to link the supercapacitors to a DC coupling point with a stable voltage. The capacitance of supercapacitors is from ~100F to ~1000F, and the rated voltage of a single module is from serval volts to ~50V in different applications [47][48]. The rated power can be made up to

~0.3 MW [49], while its rated energy capacity is relatively low at about 0.5kWh [39]. Accordingly, the rated discharging time of supercapacitors is usually shorter than 60 seconds; they are, therefore, only suitable for very short-term applications. The efficiency of supercapacitor-based storage systems is usually about 95% [48][50] and up to 97% [45]. The response time is below 5 milliseconds [40].

From the above review, the three EES systems considered in this research have the following similarities. 1) These systems use VSC power converters to control the charging/discharging power flows with similar controllers based on PI control and dq decoupling; 2) they are fast-response storage systems with response time of milliseconds; and 3) they have high cycle efficiencies of about 95% or more. In terms of the energy capacity and the rated discharging time, the descending order of these three EES systems is: Li-ion batteries (up to 10 MWh, 1 hour) > FES systems (~1 MWh, 15 mins) > Supercapacitors (0.5 kWh, 1 min).

2.3 Wave Power Generation

Wave energy attracted increasing attention during the past decade. Compared with other types of renewables, wave power is more predictable, available, continuous, and of higher power density [51]. To date, several pilot projects have been put into operation, especially along the west coast of Europe (Portugal, France, UK, Norway, etc.) and the northwest coast of the USA [52-56], where the wave power density is the highest on Earth thanks to the open sea environment and the Westerlies (a geographical belt in the middle latitudes; dominated by prevailing westerly winds). Unlike the well-developed and commercialized wind power technologies, wave power generation technologies are still at an early development stage without a clear convergence in their prototype design. In this study, the following four

aspects of wave power generation technology is reviewed: 1) the interaction between waves and power take-off devices (PTOs); 2) designs of the wave power generation units, which include the PTOs and the electric machines; 3) the control methods of the wave power generation unit for maximizing the wave power captured and integration to the grid; and 4) the impacts of the wave power generation on the grid and relevant power quality issues.

2.3.1 Wave-PTO Interactions

Waves are generated by the wind blowing across the surface of large bodies of water, e.g. oceans and seas. The wind is generated by the uneven heating of the Earth's surface by the Sun. The wave power density in hot spots is in the order of 10~100 kW/m, while the wind and solar power density is about 0.1~1 kW/m^2 [57]. For regular waves, in deep water, the wave power per length of crest is

$$P_{wave,density} = \frac{\rho g^2 H^2 T}{32\pi} \tag{2.1}$$

where ρ is the seawater density, g the gravitational acceleration, H the significant wave height which is the mean value of the highest 1/3 waves, and T the wave period (4~20s). Note that the wave period is approximately linearly related to the height, so the wave power density is approximately proportional to the cube of the wave height. This feature is similar to the wind power density being proportional to the cube of the wind speed.

For point absorbers and buoy-based WEC, there are five kinds of forces to be considered in the wave-PTO interactions: the wave excitation force F_e, the radiation force F_r related to the device velocity, the mechanical and fluid friction force F_f, the buoyancy-gravity force F_b, and the PTO force F_{pto} as the manipulated input of the system. In Newton's law, the basic

dynamic of the PTO device is

$$-F_b - F_f + M\ddot{z} = F_e + F_r + F_{pto} \tag{2.2}$$

Details of each term are presented in [58][59]. With the assumptions of linear wave and small motions, the buoyancy-gravity force F_b is proportional to the displacement of the buoy z, and the friction force F_f is proportional to $\dot{z}$, thus the left side of (2.2) can be viewed as a mass-damper-spring system. ON the right side of the equation, $F_e + F_r$ is the disturbance induced by the incident wave and F_{pto} is the load force controlled at the electrical side. [58] studies the control of a real 1/50 scaled point absorber with the friction forces ignored. [59] brings the nonlinear hydrodynamics into the wave power generation and develops and validates a nonlinear model including the friction forces.

The wave-PTO interactions discussed above are mainly applicable to the buoy-based WEC systems which are known as the point absorbers. For the OWC, there is no direct interaction between the wave and the PTO device, whose mechanical dynamics are, however, very similar to a wind turbine. Hinged contour devices, such as Pelamis, use hydraulic modules to take off the wave power and there is no direct interaction between the wave and the generator. In the latter cases, sinusoidal power inputs with characteristics of typical wave spectrums are used in studies of control methods at the electrical sector [60][61].

2.3.2 Power Generation Unit: Mechanical PTOs and Electric Machines

A wave power generation unit has two components: the mechanical PTO device, and the electric machine. In comparison with mature wind and solar power generation technologies, there is a lack of convergence of wave PTOs. Existing prototypes can be classified in the

following 4 categories as shown in Fig. 2.3. Details of each category have been presented in previous reviews [53][56][61].

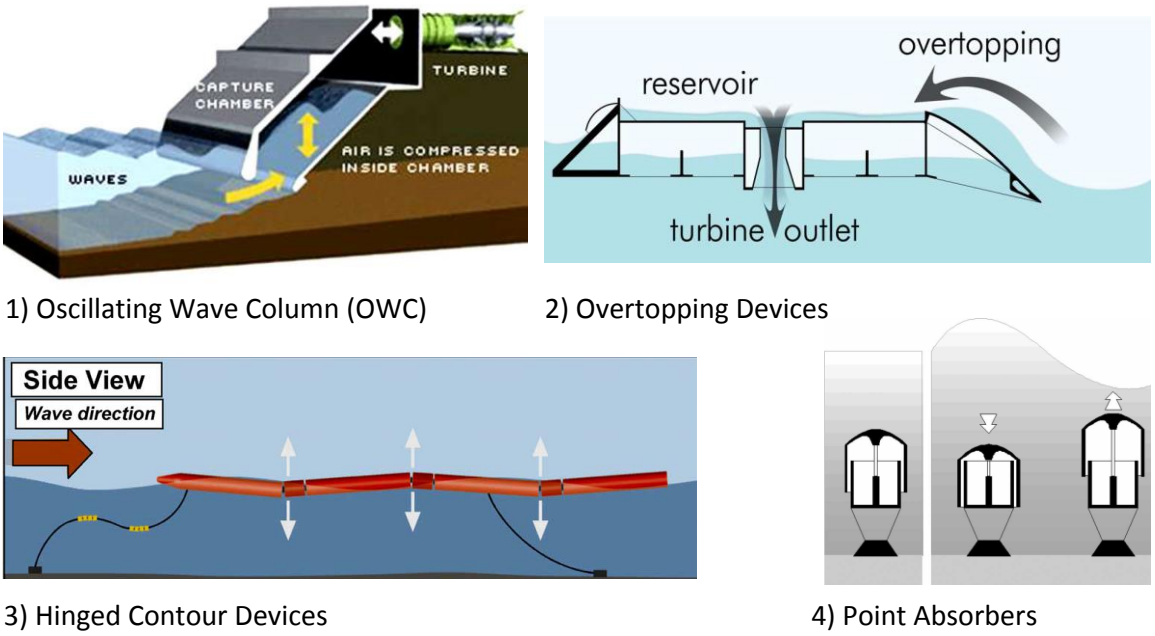

Fig. 2.3 Mainstream power take-off devices for wave energy conversion [56][61]

1) The oscillating wave column (OWC) transfers wave energy to kinetic energy of the air in a chamber and then drives the turbine-generator in a similar manner to wind power generation. Wells-turbines are popular and rotate in one direction, regardless of the direction of the air flow.

2) Overtopping devices work as a floating dam of seawater. The wave surges into the device from the top of a reservoir, maintaining a water level difference to drive a rotating electric machine. In practice, this is the least popular design among the four kinds.

3) Hinged contour devices (e.g. Pelamis) create forces and moments to generate

power from the relative rotational movements of hinged floating blocks.

4) Point absorbers. Archimedes Wave Swing (AWS) is one popular example of a large family. In comparison with hinged contour devices, this kind creates forces from the vertical linear movements of a floating block to a fixed end.

These mechanical PTO devices feature three important differences: 1) how the wave power is captured; 2) whether the generator is directly driven by the PTO or indirectly driven through a hydraulic module; and 3) does it uses linear or rotating machines. Hydraulic modules are more often to be seen in hinged contour devices and point absorbers. Linear electric machines are especially popular in point absorbers. These features have fundamental impacts on the mechanical designs and the grid-side power quality of the power generation unit.

2.3.3 Control Methods of WEC and Their Impacts on the Grid

The control of electric machines is a key factor in increasing the efficiency of wave-energy conversion. Current studies focus on the control of linear machines in point absorbers and the turbines in OWC devices. For linear machines, the PTO force must be controlled in phase with the speed of translators to maximize the converted power. In this principle, a maximum power point tracking (MPPT) control method of WEC is proposed in [69]. In [70], the PTO force of directly driven point absorbers is controlled with a resistance emulation approach to maximize the captured wave energy. [71] applied a gravitational search algorithm (GSA) to the optimization of PI control parameters in an AWS system to integrate it in a DC microgrid. [72] proposed a nonlinear model predictive control method for PMLG; for wave energy conversion, to increase the power absorption in irregular wave conditions. In OWCs, the Wells turbine is commonly used, which is specially designed to generate single directional

torque under bi-directional airflow. The MPPT control of Wells turbines is similar with that of DFIG systems for wind power generation. This problem is addressed in previous papers [73-75]. The core problem is to control the rotational speed of the turbine according to the varying speed of the airflow in the chamber, to maximize the captured power.

In addition to increasing the efficiency of energy conversion, grid-side power quality is another critical problem in WEC. There are two significant issues: the quality of the voltage and current waveforms and the smoothness of the injected power. The former is especially important for linear generator based WECs because the phase order is changing and in these systems each power generation unit needs a full rated converter. The latter problem is related to frequency variation, voltage flicker and the transient stability of the local grid [56]. The impacts of a medium-size wave farm on grids of different strength are studied in [76] using real time-series data of an experimental OWC device. It identifies flicker generated by the wave farm as an issue of integration, while in that study the wave farm can be safely connected when the grid impedance angle is greater than 50 degrees [76]. A similar result is found in [77], showing that for acceptable levels of flicker, there is a minimum permitted angle of grid impedance. [77] also developed a simplified method to estimate the flicker level induced by a wave farm. [78] reported the impacts of a real grid-connected wave farm project of the Pacific Marine Energy Centre in the U.S. The negative impacts mainly include frequency variation, harmonics, flicker, and low voltage ride-through (LVRT) capability. [79] studied using a unified power flow controller to integrate a parallel combined wind and wave farm with improved power quality.

2.3.4 Challenges of the WEC Technologies

So far, studies of wave power generation are limited to the topics of electric machine design for wave power generation and maximizing the power take-off (PTO) efficiency of a single machine [67-75][80-81]. Designs of a direct-drive linear switched reluctance machine [82], tubular linear generators, and a double-sided permanent magnet linear generator [83] are discussed in previous papers. On the other hand, there are few studies of grid side power quality especially in wave farms. Papers focusing on maximum PTO result in poor power quality to the grid without relevant discussions. When linear machines are used, their pulsating movement leads to a huge power fluctuation (0~2.0 p.u.) and usually a varying phase order in every wave period [69-71][84-85]. The operation and stability of a single wave generator (aggregated wave farm) with an aggregated wind farm in parallel using external flywheel storage was studied in [86], in which the active-power smoothing problem was also covered. In [87], a new wave power transmission method was proposed applying series connected generation units. The energy storage in wave farms was generally discussed in [88][89] with no specific storage device or control method. The former concerned the dimensioning of energy storage and cables, in which it was stated that the power fluctuation raised by wave farms, with little or no device or control method, may cause problems in the grid. The latter conducted a case study of wave farms with a very simple model of energy storage for power quality improvement.

Given this background, there are two requirements of future wave energy generation technologies. Firstly, the energy must be exploited on a wave farm basis with its own features and behaviours, as a whole, rather than a simple summation of individual wave generation machines. Secondly, in addition to a high PTO efficiency at the prime mover side, we would need to ensure a grid-friendly power quality at the electrical side, including good waveforms

for voltages and currents, controllable power factor, and smoothed power flows using power converters. The existing power converter based solutions have two major problems: (a) the cost and complexity of a wave farm are significantly increased with the increasing number of power converters, and (b) the captured wave power could change significantly between zero and megawatts in a typical wave period of 5~12s, which may even be aggravated for bigger wave farms. These power fluctuations cause thermal excursions, frequency variations, voltage flickers, and other instabilities in the local grid. In addition, over-rated converters are needed to tolerate the peak power flow. Although in principle, the increasing number of wave generation machines in a wave farm would be helpful to smooth the total power output to some extent, it is still necessary to integrate a so-called **energy buffer** - an energy storage device with fast charging/discharging capability in a timescale of a typical wave period of 5~12s on a wave-to-wave basis. The conventional energy buffer solutions and their drawbacks are:

1) ***Natural energy buffer***: in an over-topping device like the Wave Dragon, no artificial energy storage is built but the wave power is naturally buffered by its water reservoir. OWC is similar, where the air chamber acts as natural energy storage. In this solution, there is no active control of the energy storage and the power smoothing effect is poor.

2) ***Hydraulic energy buffer***: examples include the Pelamis in which the high-pressure accumulator can smooth the power flow to the generator by storing and releasing the energy with its mechanical control, by manifolds, however, it is difficult and complicated to provide accurate mechanical control compared with electrical solutions.

3) ***Electrical energy buffer***: For those PTO devices with which it is difficult to integrate a

mechanical energy buffer, studies have been conducted on electrical solutions such as batteries or capacitors. These solutions are, however, largely limited by the short cycle life of the batteries and the space required by the capacitors on an off-shore platform. Moreover, both the machine and the rectifier must be over-rated to tolerate the peak power since the power is only smoothed in the electrical sector on, or after, the DC link.

CHAPTER 3 CONTROL PARAMETERS DETERMINATION OF VSC WITH INSUFFICIENT INTERFACE RESISTANCE

Abstract- This chapter discusses the converter layer control of fluctuating renewable power as the fundamental of the integration and control of renewable energy sources. The modelling and controls of VSC systems connected to different plants (the grid, PMSM, IM stator, DFIG rotor) are presented for the convenience of the following discussions of fluctuating power generation. A popular conventional method for the determination of PI parameters for a VSC controller, known as the zero-pole cancelling method, is investigated based on a state space model and related problems of a lack of interface resistance are indicated. Two new methods are proposed to solve these problems, which are validated through simulations and case studies.

3.1 Modelling and Control of the VSC-based Electrical Driving Systems

Electrical driving systems, based on Voltage Source Converters (VSC) are the fundamentals of many renewable power plants including solar, wind and most wave power generation. The control system consists of three modules: the converter, the controlled plant, and the controller. The models of VSC control systems are described in the classical dq reference frame. In this study, as fundamental knowledge of renewable power generation, these models are briefly reviewed in terms of their different controlled plants: the grid, permanent magnetic

synchronous machines (PMSM), induction machines (IM), and doubly-fed induction generators (DFIG). Switching dynamics in 0.2-0.5ms are not considered in these models, and it is assumed that the actual output voltages of the converter perfectly follow the references given by the controller.

3.1.1 VSC Connected to the Grid

In a VSC-based power generation unit, the inverter is connected to the point of common coupling via a transformer. By simplifying the transformer as an equivalent short-circuit impedance, the plant model is described by Fig. 3.1 and (3.1)-(3.3).

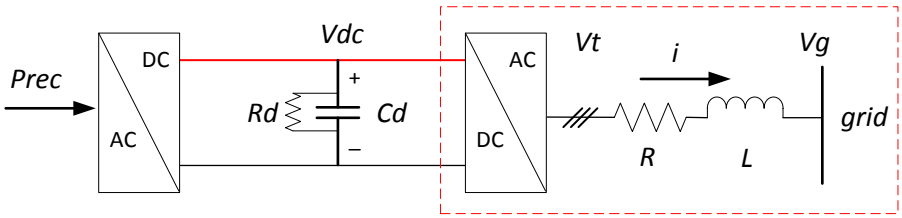

Fig. 3.1 The plant model of a VSC inverter connected to the grid

$$v_{td} = Ri_d + L\frac{d}{dt}i_d - \omega L i_q + v_{gd} \tag{3.1}$$

$$v_{tq} = Ri_q + L\frac{d}{dt}i_q + \omega L i_d \tag{3.2}$$

$$(P_{grid}, Q_{grid})^T = \frac{3}{2}v_{gd}(i_d, i_q)^T \tag{3.3}$$

The d-axis of the reference frame is aligned with v_g so there is no v_{gq} in the q-axis equation. In this plant model, $(i_d, i_q)^T$ are the state variables, $(v_{td}, v_{tq})^T$ the manipulated inputs, and v_{gd} the disturbance. From this point of view, this plant model is a second-order nonlinear

system because there is a time-variant coefficient ω. However, for convenience in most engineering practices, the cross-coupling term ωLi is treated as a disturbance like v_{gd}, both of which would be compensated for in the controller since they are easily measurable. This operation is known as dq decoupling. After decoupling, the plant model becomes two independent d and q-axis first-order systems, and is popularly controlled by an output feedback PI controller.

The above discussion only covers how to manipulate the converter voltage to make the current follow the current reference, which is known as the inner loop control. By contrast, the outer loop control manipulates the current reference, with the assumption that the inner loop is much faster than the outer loop so the actual currents perfectly follow their references, to control the real and reactive power. When the d-axis is aligned with the grid voltage v_{gd}, the d-axis controls the real power *P* and the q-axis controls the reactive power *Q*.

For the outer loop controls of both axis, there are *PQ* direct control and indirect control methods. The PQ direct control is straightforward since the real and reactive power is proportional to $(i_d, i_q)^T$ respectively once v_{gd} is measured. In this case, there would be no need for additional PI controllers in the outer loop. However, in many previous studies the PI controllers are still used in a PQ directly controlled outer loop without further explanations or discussions on how the PI parameters affects the control system dynamics. This is rather confusing, and I hold suspect that it is because those authors don't really understand why a PI controller should be there, or not.

The indirect outer loop control achieves other control objectives by controlling PQ. Examples include DC voltage control of d-axis, AC frequency control of d-axis, and AC voltage control

of q-axis. In any of these, the outer loop PI controllers are necessary. Here, the outer loop control consists of the DC voltage control of d-axis and the zero-reactive power control (direct Q control with a zero reference) of q-axis and is discussed because it is the most popular case in VSC-based renewable power generation. To control the DC voltage of VSC by controlling the real power we need to know the converter model, and a simple version of it is

$$P_{rec} - P_{inv} = \frac{C_d}{2}\frac{d}{dt}v_{dc}^2 + \frac{1}{R_d}v_{dc}^2 \tag{3.4}$$

$$P_{inv} = P_{grid} = v_{gd}i_d \tag{3.5}$$

This model ignores the conversion losses, which is reasonable since most of VSC devices have efficiencies of over 97%, in normal operations and at rated load capacity. With appropriate measurements and compensations of v_{gd} and P_{rec}, this model can be viewed as a first-order linear system with the state variable v_{dc}^2, and the outer loop controller controls v_{dc}^2 by manipulating i_d reference.

Based on all the discussions above, the controller for grid-connected VSC is presented in Fig. 3.2.

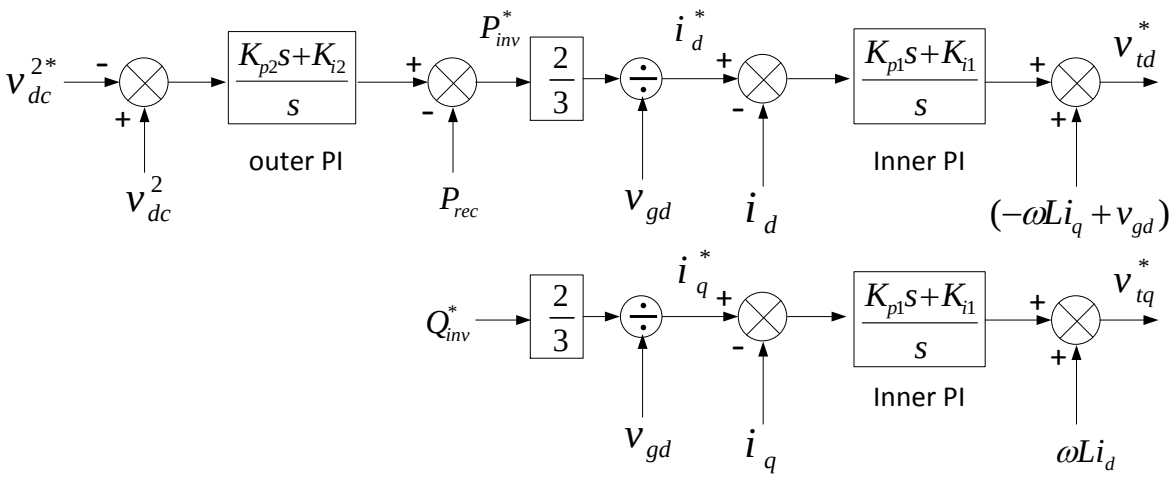

Fig. 3.2 The controller diagram of the VSC connected to a local grid

Overall, the control system of grid-connected VSC is relatively simple, but it reveals the important framework of the VSC control systems including: the inner and outer loops, the dq decoupling and disturbance compensation, and the PQ direct and indirect controls. As will be seen, the control systems of VSC connected to other plants are in the same framework, and consequently the correlated control problems may be solved by unified solutions.

3.1.2 VSC Connected to the PMSM

To control the PMSM we need to know its model. For concise expressions, space phasors $X = x_d + jx_q$ are used to combine the d and q-axis equation as the real and imaginary part of a single complex equation. In the synchronous reference frame, the model of a PMSM is

$$V_s = R_s I_s + \frac{d}{dt}\psi_s + j\omega_r \psi_s \tag{3.6}$$

$$\psi_s = \psi_f + L_s I_s \tag{3.7}$$

$$T_{em} = \frac{3}{2} p\left(\psi_{fd} \cdot i_{sq}\right) \tag{3.8}$$

The d-axis is aligned with the permanent magnet flux ψ_{fd}. Since $\psi_f = \psi_{fd}$ is a constant, by substituting ψ_s into the voltage equation, we have

$$v_{sd} = R_s i_{sd} + L_s \frac{d}{dt} i_{sd} - \omega_r L_s i_{sq} \tag{3.9}$$

$$v_{sq} = R_s i_{sq} + L_s \frac{d}{dt} i_{sq} + \omega_r L_s i_{sd} + \omega_r \psi_{fd} \tag{3.10}$$

These two equations are comparable to (3.1) and (3.2) with similar terms such as the manipulated inputs $(v_{sd}, v_{sq})^T$, the state variables $(i_{sd}, i_{sq})^T$, the cross coupling terms and the disturbance $\omega_r \psi_{fd}$. So it has a very similar structure of the inner loop control with the grid-connected VSC. As for the outer loop, the primary control objective, the electromagnetic torque T_{em} is proportional to i_{sq}, so the q-axis is in charge of the direct torque or power control. The d-axis controlling i_{sd} is in charge of the stator voltage or the stator reactive power control. A common practice is setting a zero reference of i_{sd} to minimize the currents flowing through the converter. In these cases, again there is no need of PI controllers in the outer loop.

Based on the discussions above, the controller of the PMSM-connected VSC is presented in Fig. 3.3.

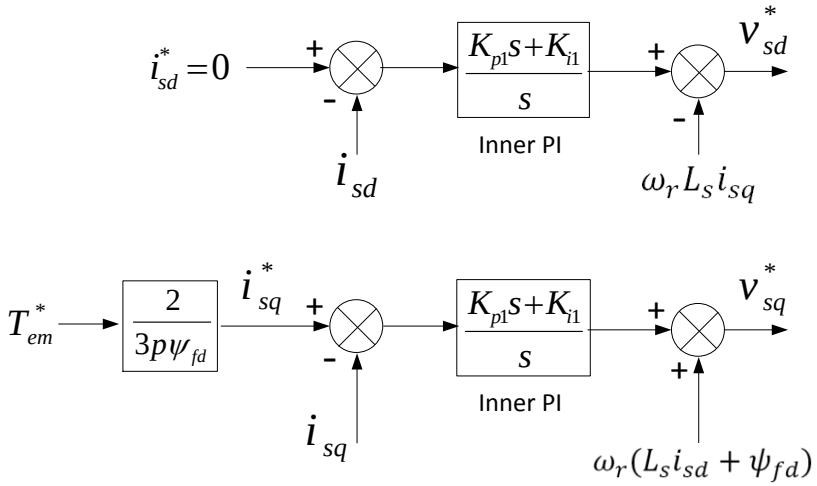

Fig. 3.3 The controller diagram of the VSC connected to a PMSM

3.1.3 VSC Connected to the Stator of IM

The model of induction machines is more complicated than the PMSM model because there are additional rotor windings dynamics. In the synchronous reference frame with the d-axis aligned with the rotor flux ψ_{rd}, the IM model consists of voltage and flux equations and the torque equation is

$$V_s = R_s I_s + \frac{d}{dt}\psi_s + j\omega_s \psi_s \tag{3.11}$$

$$V_r = R_r I_r + \frac{d}{dt}\psi_r + j(\omega_s - \omega_r)\psi_r \tag{3.12}$$

$$\psi_s = L_s I_s + L_m I_r \tag{3.13}$$

$$\psi_r = L_m I_s + L_r I_r \tag{3.14}$$

$$T_{em} = \frac{3L_m}{2L_r} p(\psi_{rd} \cdot i_{sq}) \tag{3.15}$$

Since the rotor winding of an IM is short-circuit, the rotor voltage V_r in this model is zero. For the convenience of the controller development, it is desirable to express the voltage equations using the state vector $(I_s, \psi_r)^T$. From a linear transformation of (3.13) and (3.14), we have

$$I_r = \frac{1}{L_r}(\psi_r - L_m I_s) \tag{3.16}$$

$$\psi_s = \frac{L_m}{L_r}\psi_r + \sigma L_s I_s \tag{3.17}$$

where $\sigma = 1 - \frac{L_m^2}{L_s L_r}$ is the inductance coefficient. By substituting ψ_s into (3.11) and ignoring the dynamic of the rotor flux ψ_r, we have the stator voltage equations split into d and q-axis as

$$v_{sd} = R_s i_{sd} + \sigma L_s \frac{d}{dt} i_{sd} - \omega_s \sigma L_s i_{sq} \tag{3.18}$$

$$v_{sq} = R_s i_{sq} + \sigma L_s \frac{d}{dt} i_{sq} + \omega_s \sigma L_s i_{sd} + \omega_s \frac{L_m}{L_r}\psi_{rd} \tag{3.19}$$

As can be seen, the stator voltage equations of the IM are similar to those of the PMSM, only with the stator inductance L_s and the back EMF $\omega\psi_{fd}$ replaced with the terms σL_s and $\omega_s \frac{L_m}{L_r}\psi_{rd}$ respectively. The controller diagram of the IM-connected VSC is similar to that of the PMSM-connected VSC but with different decoupling terms and disturbance compensation. Notice that the derivation of this plant model and the controller are based on the assumption that the rotor flux ψ_r is a measurable constant, which is guaranteed by the rotor flux estimator [62].

Based on the discussions above, the controller of the IM-connected VSC is presented in Fig. 3.4.

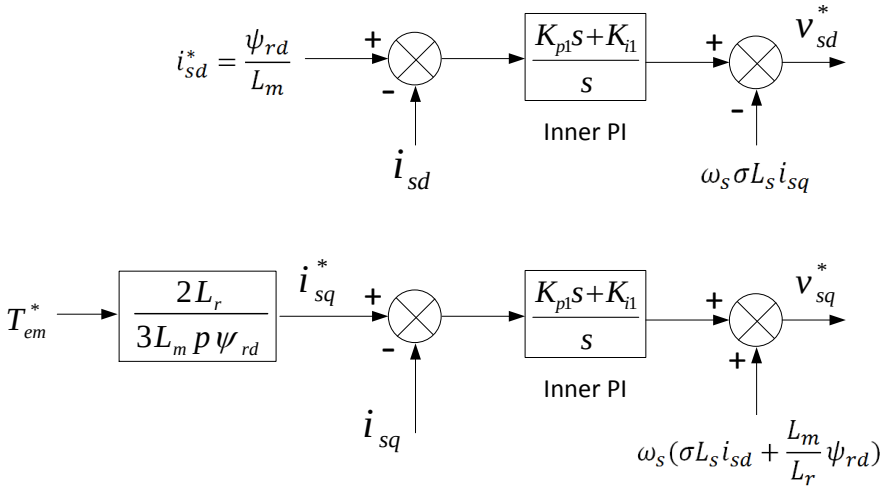

Fig. 3.4 The controller diagram of the VSC connected to the stator of an IM

3.1.4 VSC Connected to the Rotor of DFIG

In a DFIG system, the plant is also an induction machine but the VSC is connected to the rotor instead of the stator. For this reason, only a wound-rotor IM can be used in a DFIG system, not a squirrel-cage. The rotor voltages $(v_{rd}, v_{rq})^T$ are no longer zero but become manipulated inputs. The voltage and flux equations, for the plant model, are the same as (3.11)-(3.14) because it is also an induction machine but the torque equation would be a different expression for the feasibility and convenience of the variable measurements. There are two options of the d-axis alignment. One is the stator flux ψ_{sd} which is easier for torque control, and another one is the stator voltage v_{sd} which is easier for stator reactive power control. Comparative studies of these two alignment methods are given in [90] and [91]. In this review, the former condition is applied, thus the torque equation is

$$T_{em} = -\frac{3L_m}{2L_s} p(\psi_{sd} \cdot i_{rq}) \tag{3.20}$$

For convenience in developing the controller, it is desirable to express the voltage equations (3.11) and (3.12) using the state vector $(I_r, \psi_s)^T$. From a linear transformation of (3.13) and (3.14), we have

$$I_s = \frac{1}{L_s}(\psi_s - L_m I_r) \tag{3.21}$$

$$\psi_r = \frac{L_m}{L_s}\psi_s + \sigma L_r I_r \tag{3.22}$$

By substituting ψ_r into (3.12) and ignore the dynamic of the stator flux ψ_s, we have the rotor voltage equations split into d and q-axis as

$$v_{rd} = R_r i_{rd} + \sigma L_r \frac{d}{dt} i_{rd} - (\omega_s - \omega_r)\sigma L_r i_{rq} \tag{3.23}$$

$$v_{rq} = R_r i_{rq} + \sigma L_r \frac{d}{dt} i_{rq} + (\omega_s - \omega_r)\sigma L_r i_{rd} + (\omega_s - \omega_r)\frac{L_m}{L_s}\psi_{sd} \tag{3.24}$$

As can be seen, this plant model is similar with the models of PMSM and IM but with two major differences. First, it is manipulating the voltage and controlling the current on the rotor instead of the stator as in PMSM and IM. Second, it has different decoupling terms $(\omega_s - \omega_r)\sigma L_r[-i_{rq}, i_{rd}]^T$ and q-axis disturbance $(\omega_s - \omega_r)\frac{L_m}{L_s}\psi_{sd}$. Note that the plant model and controller are derived on the assumption that the stator flux ψ_s is a measurable constant. This condition is indicated by the stator flux estimator [63].

In the outer loop, according to the torque equation, the torque is proportional to i_{rq} so the outer loop control of the q-axis is simply a gain. Since the stator of the DFIG is directly connected to the grid, the i_{rd} is usually manipulated as the excitation current to control the stator reactive power Q_s through an outer loop PI controller, because there is no simple linear relationship between them. The parameters of this outer loop PI controller need to be tuned.

Based on the discussions above, the controller of the rotor-side VSC of DFIG is presented in Fig. 3.5.

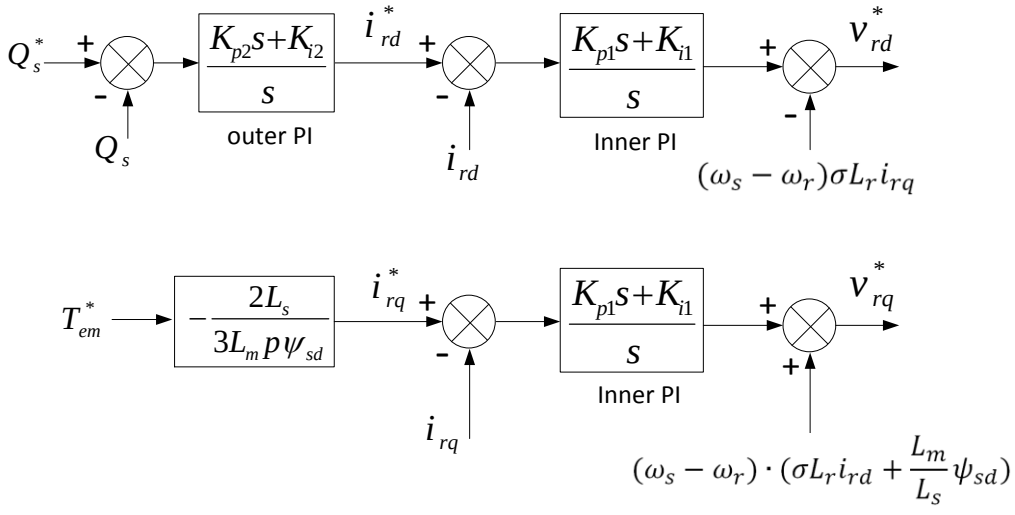

Fig. 3.5 The controller diagram of the VSC connected to the rotor of DFIG

3.2 The Zero-pole Cancelling Method and Its Risks

The zero-pole cancelling method is widely used to calculate the PI parameters. There is a risk of failure of this method when there is insufficient resistance between the VSC and the grid/machine. The studies presented in this and the following sections of this Chapter have been published in paper [64].

3.2.1 Zero-pole Cancelling in VSC Control Systems

The idea of the zero-pole cancelling method is using the zero of the PI controller to "cancel" the pole of the plant. However, the pole is not truly eliminated; it is only invisible from outside the PI control loop.

The plant in a VSC control system is presented in Fig. 3.6. *L* and *R* are the interface inductance and resistance that represents either the short-circuit impedance of the converter transformer when connected to the grid or the equivalent stator impedance when connected to an electric machine. The dq phasor equation of the plant is

$$L\frac{d}{dt}i = -Ri + (v_i - v_b) - j\omega Li \tag{3.25}$$

The variables in the above equation are complex numbers with real d and imaginary q components. As has been discussed in Section 3.1, the cross-coupling term is always eliminated by the dq decoupling control. Accordingly, the inner loop of the VSC control system is equivalently simplified and presented in Fig. 3.7.

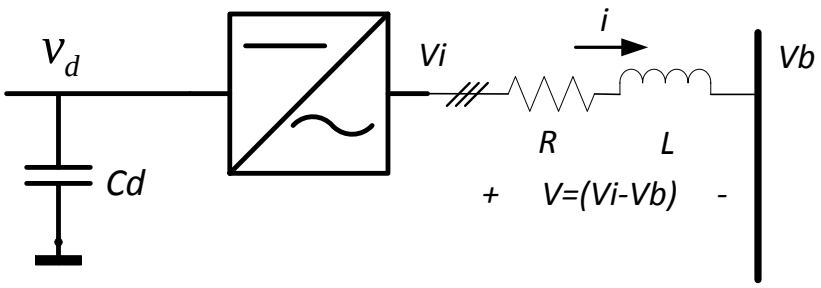

Fig. 3.6 The plant of a VSC control system

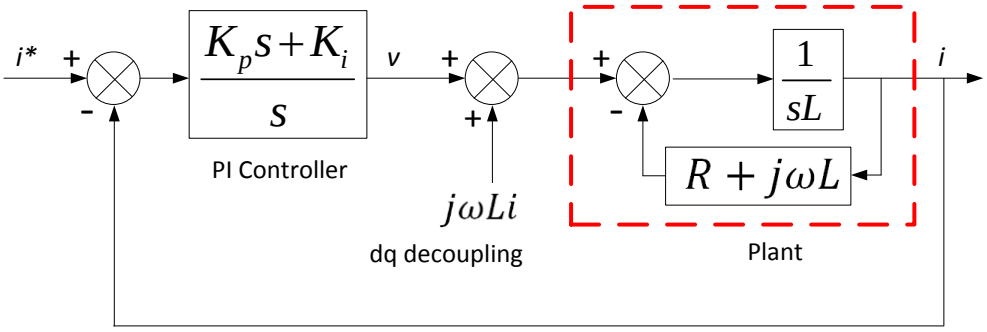

Fig. 3.7 The inner loop control of VSC

From Fig. 3.7, the simplified model of the VSC plant is first-order and the whole control system, including the inner loop PI controller, is second-order. To make the zero-point of the PI controller equals to the pole of the plant, the PI parameters must be

$$\begin{cases} K_p = \dfrac{L}{T} \\ K_i = \dfrac{R}{T} \end{cases} \tag{3.26}$$

By substituting (3.26) to Fig. 3.7, the close-loop transfer function of the control system is first-order

$$\frac{I(s)}{I^*(s)} = \frac{1}{Ts + 1} \tag{3.27}$$

therefore the PI parameters could be determined by (3.26) with a given time constant.

3.2.2 Hidden Dynamics Created by the Cancelled Pole

The control system in Fig. 3.7 is second-order, but only one pole

$$s_1 = -\frac{1}{T} \tag{3.28}$$

is shown by the transfer function (3.27). Another pole

$$s_2 = -\frac{K_i}{K_p} = -\frac{R}{L} \tag{3.29}$$

is missing in the transfer function due to zero-pole cancellation. However, the dynamics related to the cancelled pole cannot be truly eliminated but is still inside the system. It is referred to as the hidden dynamics, resulting from the cancelled pole. The hidden dynamics are usually undesirable because they are beyond the scope of the input-output relationships and can cause problems of controllability, observability, and stability of the system [92]. These problems should be studied using a state-space model. The state-space model of a VSC control system is

$$\frac{d}{dt}\begin{bmatrix} i \\ v \end{bmatrix} = A\begin{bmatrix} i \\ v \end{bmatrix} + Bu \tag{3.30}$$

$$y = i = C\begin{bmatrix} i \\ v \end{bmatrix} \tag{3.31}$$

$$u = \left(K_p\frac{d}{dt} + K_i\right)i^* \tag{3.32}$$

$$A = \begin{bmatrix} -\frac{R}{L} & \frac{1}{L} \\ -K_i + \frac{R}{L}K_p & -\frac{K_p}{L} \end{bmatrix} \tag{3.33}$$

$$B = [0\ 1]^T \tag{3.34}$$

$$C = [1\ 0] \tag{3.35}$$

By substituting (3.26) to (3.33) to apply the zero-pole cancelling method, the transfer matrix *A* becomes

$$A = \begin{bmatrix} -\frac{R}{L} & \frac{1}{L} \\ 0 & -\frac{1}{T} \end{bmatrix} \tag{3.36}$$

$$\det(sI - A) = \left(s + \frac{R}{L}\right)\left(s + \frac{1}{T}\right) \tag{3.37}$$

Both of the poles of the plant are presented by a state-space model and are, obviously, the same as those given by (3.28) and (3.29).

Applying similar diagonalization of the transfer matrix, the system model can be rearranged with a new state vector as

$$\frac{d}{dt}\begin{bmatrix} i + \frac{T}{L}v \\ v \end{bmatrix} = \begin{bmatrix} -\frac{R}{L} & 0 \\ 0 & -\frac{1}{T} \end{bmatrix}\begin{bmatrix} i + \frac{T}{L}v \\ v \end{bmatrix} + \begin{bmatrix} \frac{d}{dt} + \frac{R}{L} \\ \frac{L}{T}\frac{d}{dt} + \frac{R}{T} \end{bmatrix} i^* \tag{3.38}$$

In a diagonalized transfer matrix, the two new state variables are independent. Related to the pole $s_2 = -\frac{R}{L}$ cancelled in the transfer function (3.27), the hidden state variable is $x_h = i + \frac{T}{L}v$.

The tracking error of current is defined as

$$e = i - i^* \tag{3.39}$$

Using this error and assuming the current reference is a constant $\frac{d}{dt}i^* = 0$, (3.38) can be split into two equations

$$\frac{d}{dt}\left(e + \frac{T}{L}v\right) = -\frac{R}{L}\left(e + \frac{T}{L}v\right) \tag{3.40}$$

$$\frac{d}{dt}v = -\frac{1}{T}v + \frac{R}{T}i^* \tag{3.41}$$

These two equations are interpreted as follows. The state variable v converges at the time constant of T, while the state variable $(e + \frac{T}{L}v)$ converges to zero at the time constant of L/R. Either of the time constants can dominate the convergence of the current error e; depending on which one is bigger.

The controllability and observability of the control system are examined as below.

$$\det[\mathrm{AB\ B}] = \det\begin{bmatrix} \frac{1}{L} & 0 \\ -\frac{1}{T} & 1 \end{bmatrix} = \frac{1}{L} \neq 0 \tag{3.42}$$

$$\det\begin{bmatrix} CA \\ C \end{bmatrix} = \det\begin{bmatrix} -\frac{R}{L} & \frac{1}{L} \\ 1 & 0 \end{bmatrix} = -\frac{1}{L} \neq 0 \tag{3.43}$$

The non-zero results of (3.42)(3.43) demonstrate the controllability and the observability of the control system.

The theoretical research is concluded by (3.40)-(3.43). It proves the controllability and observability of the zero-pole cancelling method, however, the effects of the hidden dynamics are strongly affected by the value of *R*. There are three cases:

Case 1: $T > L/R$. The zero-pole cancelling method is applicable. The current error is dominated by the pole s_1 shown in the transfer function (3.27) and the hidden dynamics can be ignored.

Case 2: $L/R > T$. The variable $\left(e + \frac{T}{L}v\right)$ is slower than v and the convergence of the current error is dominated by the "cancelled" pole s_2. The real time constant of convergence is L/R but not T as given by (3.27).

Case 3: $R \to 0$. For example, when the VSC is connected to superconducting electric machines or transformers, the interface resistance goes to zero. In this case the voltage v converges to zero but the current error is no longer convergent and becomes vulnerable to the disturbance. The zero-pole cancelling method is not applicable.

3.3 Two New Methods to Calculate the PI parameters

In this study, two new methods to calculate the PI parameters are proposed and the risk of insufficient interface resistance is eliminated.

3.3.1 Virtual Resistance Method

The virtual resistance method uses an extra feedback of the current signal to the voltage reference to relocate the cancelled pole in the s-plane. The gain of the extra feedback loop is called the virtual resistance, which causes voltage drop but doesn't consume real power. In fact, as can be seen from section 3.4 and appendix A, a typical per-unit value of the virtual resistance is 0.0024, which is very small and would not cause serious, additional voltage drop. The control diagram of this method is presented in Fig. 3.8.

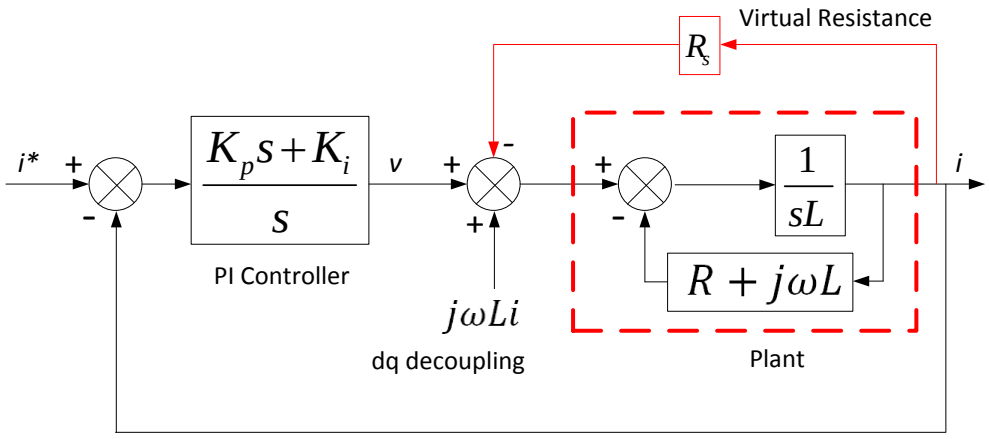

Fig. 3.8 The control diagram of the virtual resistance method

The plant parameter R is equivalently changed by this method to $(R + R_s)$. The PI parameters are calculated as

$$\begin{cases} K_p = \dfrac{L}{T} \\ K_i = \dfrac{R + R_s}{T} \end{cases} \tag{3.44}$$

The transfer function of the control system is the same as (3.27) with these parameters. Now the cancelled pole is

$$s_2 = -\frac{K_i}{K_p} = -\frac{R + R_s}{L} \tag{3.45}$$

Notice the virtual resistance R_s can be made big enough so that $T > L/(R + R_s)$ and Case 1 in subsection 3.2.2 is fulfilled.

3.3.2 The Second-Order Filter Control

The second-order filter control doesn't cancel the pole of the plant and there are no hidden dynamics. It makes the whole control system a second-order filter and calculates the PI parameters according to the desirable damping ratio ξ and natural frequency ω_n.

From Fig. 3.6, the close-loop transfer function can be written as

$$\frac{I(s)}{I^*(s)} = \frac{\dfrac{K_p}{L}s + \dfrac{K_i}{L}}{s^2 + \dfrac{(K_p + R)}{L}s + \dfrac{K_i}{L}} \tag{3.46}$$

There is a derivative term and a proportional term in the nominator of (3.46). For the step response of the system, the derivative term makes no impact on the steady state and only adds an extra overshoot on the transient response. Nor does it affect the stability of the system

because it is not related to the position of poles. Thus, the derivative term can be ignored by not considering the extra overshoot of the step response. It is also worth noting that, in engineering practices generally, a derivative term amplifies the noise. In this case, the order of the denominator is higher than that of the nominator, and the derivative term only exists, mathematically, in the nominator of (3.46). No derivative block really exists in the whole system, as shown in Fig. 3.6, so the noise would not be amplified by the whole system. When the derivative term $\frac{K_p}{L}s$ is ignored, (3.46) is in the form a standard second-order filter

$$H(s) = \frac{\omega_n^2}{s^2 + 2\xi\omega_n s + \omega_n^2} \tag{3.47}$$

The desirable damping ratio ξ and natural frequency ω_n are

$$\begin{cases} \xi = 1/\sqrt{2} \\ \xi\omega_n = \dfrac{1}{T} \end{cases} \tag{3.48}$$

This damping ratio is the minimum value that doesn't cause resonance. From equations (3.46)-(3.48), the PI parameters are calculated as

$$\begin{cases} K_p = \dfrac{2\sqrt{2}L}{T} - R \\ K_i = \dfrac{4L}{T^2} \end{cases} \tag{3.49}$$

3.4 Simulations and Demonstrations

We have discussed three methods to calculate the PI parameters in dq decoupling control of VSC, which are presented in (3.26)(3.44)(3.49). The common zero-pole cancelling method is

no longer applicable, without sufficient interface resistance, due to hidden dynamics. The above theoretical analysis is demonstrated by simulations on RTDS.

3.4.1 Simulation Model and Its Validation

As shown in Fig. 3.9, a test bed for PI parameters determination methods is developed based on the real grid model including the IEEE benchmark model of synchronous generators (governor ieee type 1, excitation ieee type ST1, IEE2ST PSS) as given in the library of RTDS [65]. The plant model consists of a STATCOM and a parallel time-variant reactive power consumption unit, which is represented by an induction motor with time-variant mechanical load in square wave in this study. The STATCOM is controlled to keep a unity power factor on the point of common coupling. In this case, the reactive power Q is directly controlled by the q-axis current, and thus the control performances are directly affected by the inner-loop PI parameters.

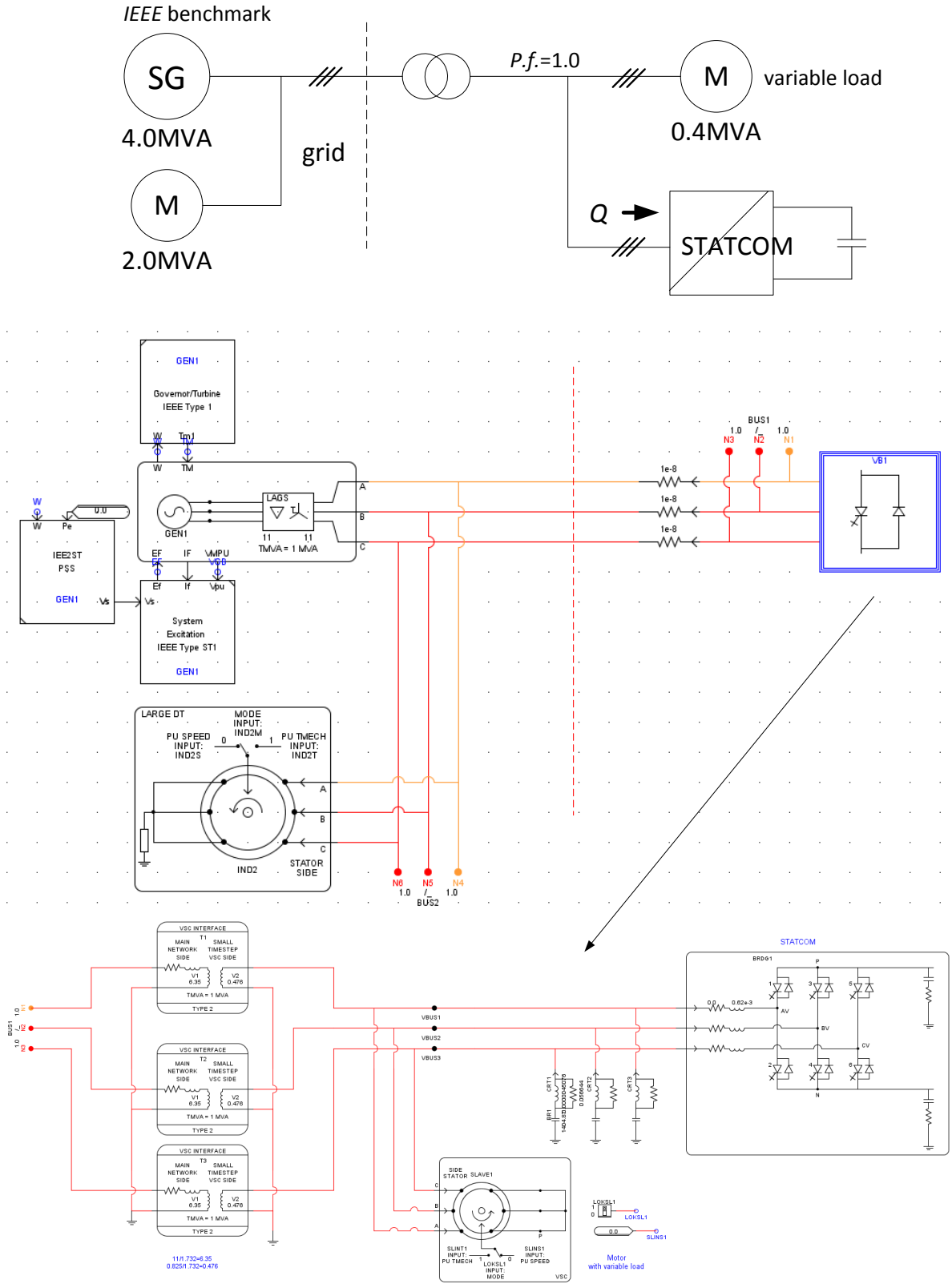

Fig. 3.9 The test bed of the PI parameters determination methods built on RTDS

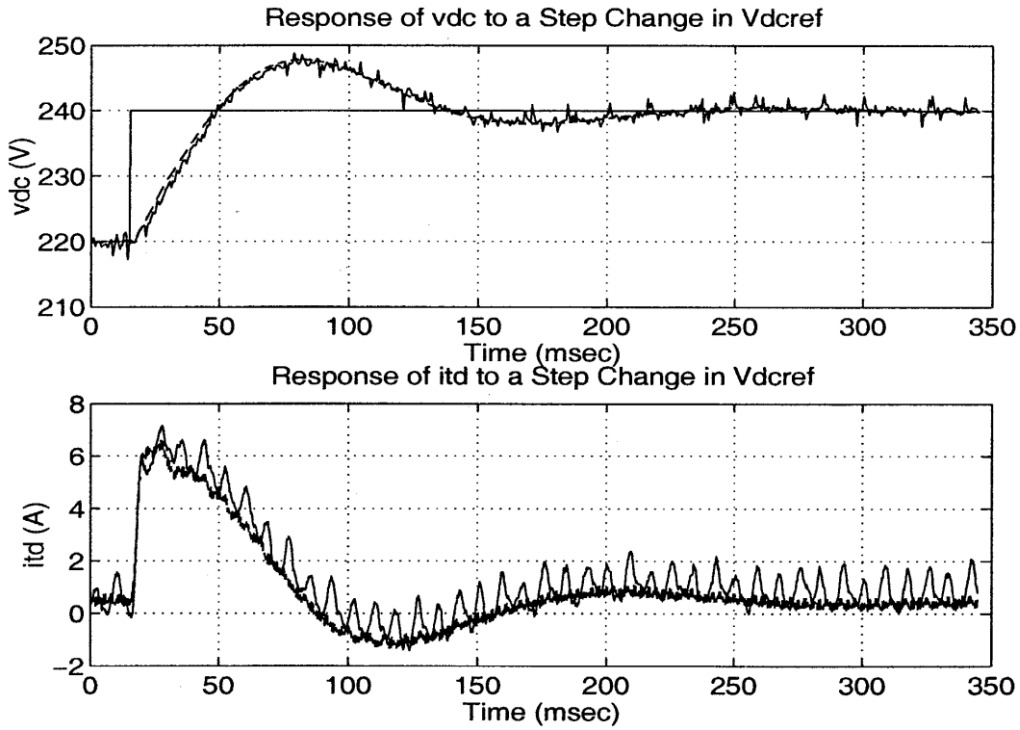

Fig. 3.10 DC voltage step responses of the benchmark system [66]

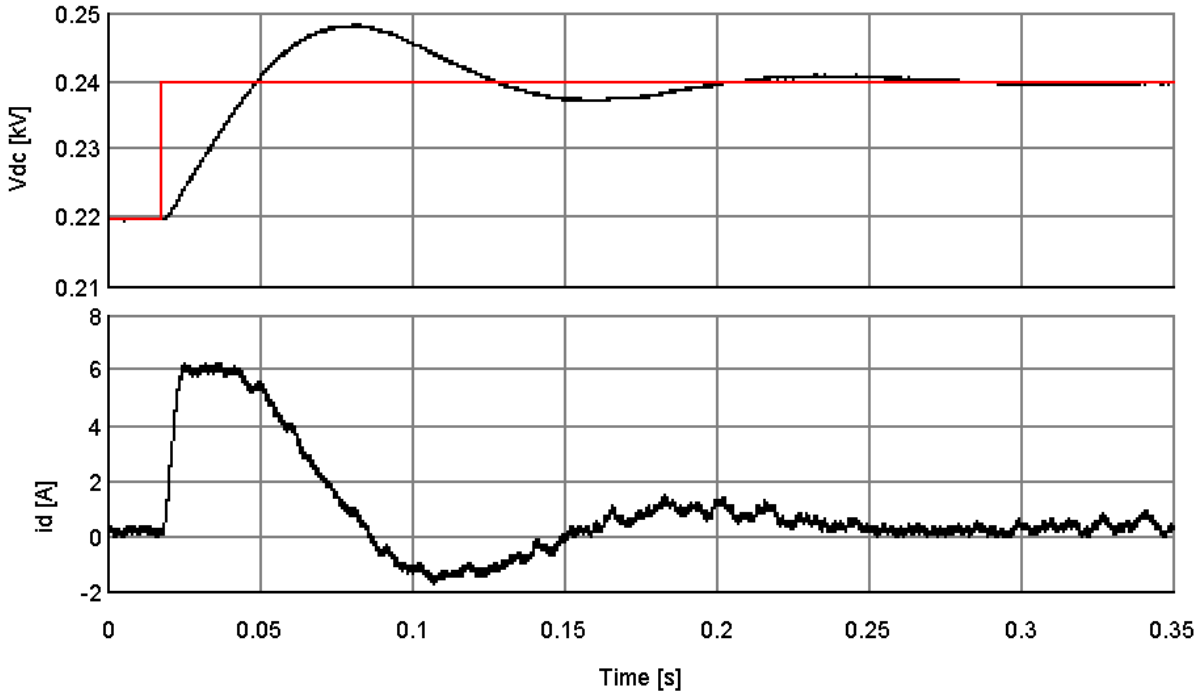

Fig. 3.11 DC voltage step responses of the developed model

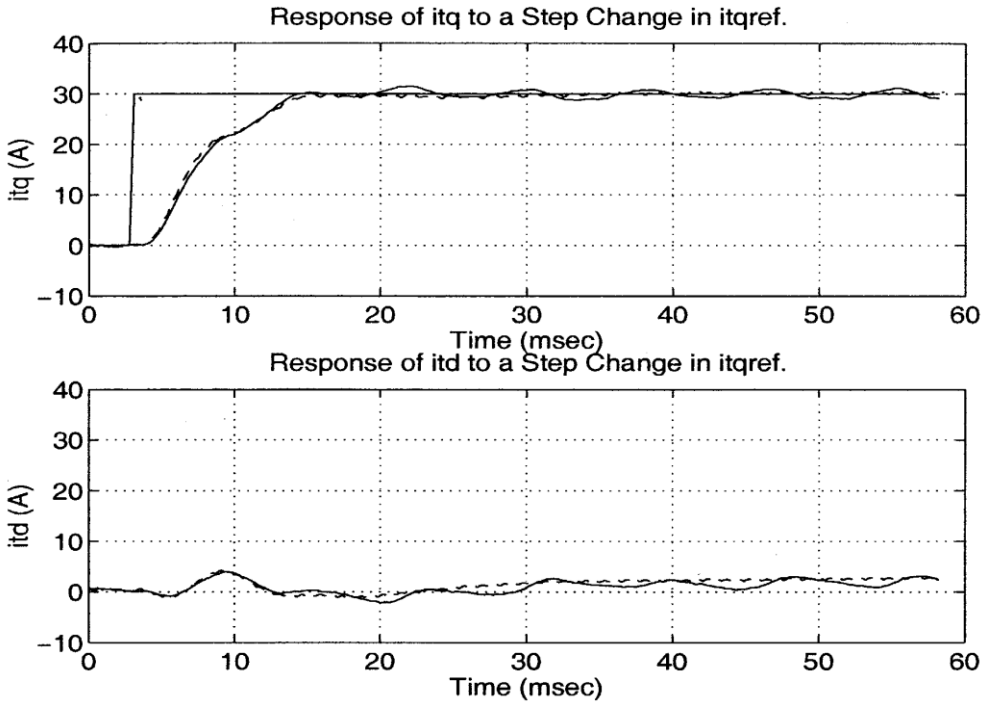

Fig. 3.12 Q-axis current step responses of the benchmark system [66]

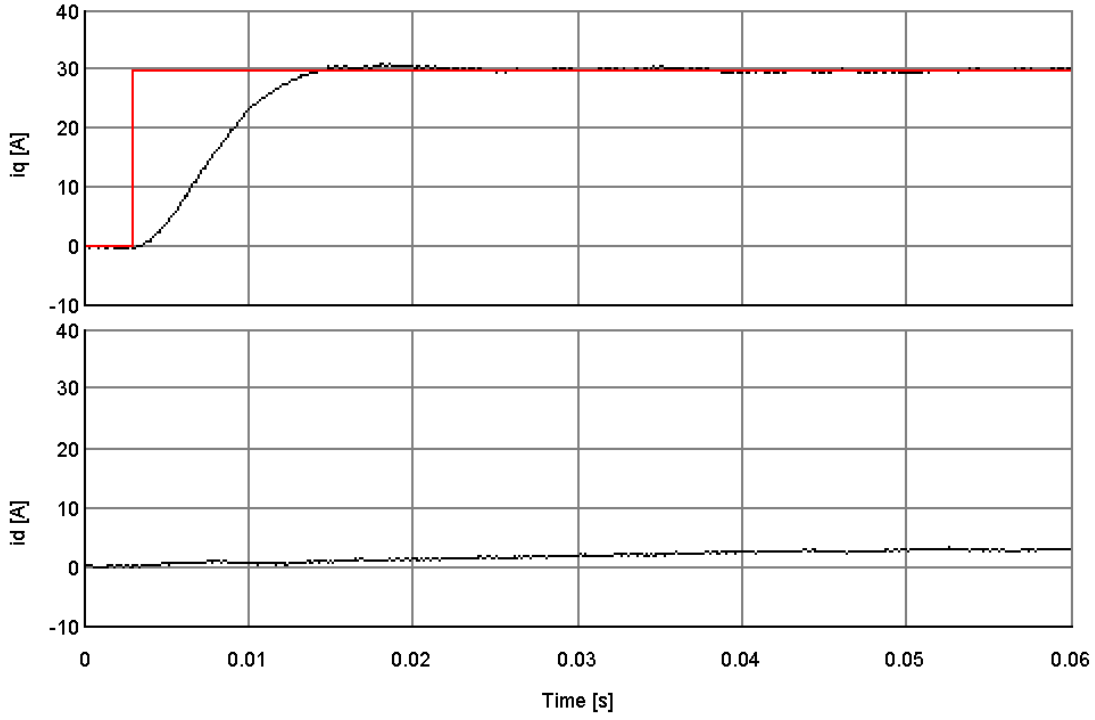

Fig. 3.13 Q-axis current step responses of the developed model

Fig. 3.10-3.13 present the validation of the simulation model. The RTDS simulation results are compared with the experiment and PSCAD simulation results of the STATCOM benchmark system [66]. All the system and control parameters are given by [66]. We are particularly interested in the capabilities of STATCOM to regulate its DC voltage and to control the q-axis current (and consequently, the reactive power). Fig. 3.10 and 3.11 show the responses of DC voltage and d-axis current to a step change of DC voltage reference given by the benchmark system and the developed model, respectively. Fig. 3.12 and 3.13 show the responses of d and q-axis currents to a step change of q-axis current reference given by the benchmark system and the developed model, respectively. The results show good agreement between the developed model and the benchmark system.

3.4.2 Simulation Results

The simulation conditions set out below. The interface inductance of the STATCOM is 0.62mH. The time constant of the inner loop control is 5ms. The rated capacity of the IEEE benchmark model of a synchronous generator is 4.0MVA, and that of the variable load machine is 0.4MVA. Details of the model parameters are presented in Appendix A. The STATCOM control has been discussed in Section 3.1.1.

The references and actual values of the current and reactive power of the STATCOM under different cases are shown in Fig. 3.14 and 3.15. The tracking error converges to zero slowly when a large time constant of L/R is dominant, because of the hidden dynamics. This transient process becomes longer with the reduction of R. When R is zero, the tracking error is no longer convergent and becomes a steady-state error under the zero-pole cancelling

method. Comparatively, the two proposed methods can still make the tracking error converge quickly at the time constant of T even when $R = 0$.

In conclusion, the simulation results show the effects of the hidden dynamics on the VSC control. With the reduction of the interface resistance, the convergence of the current error becomes slower, and the controlled outputs cannot track the references when there is no resistance. These results match the theoretical analysis. The simulation results also demonstrate that the two proposed methods can solve this problem.

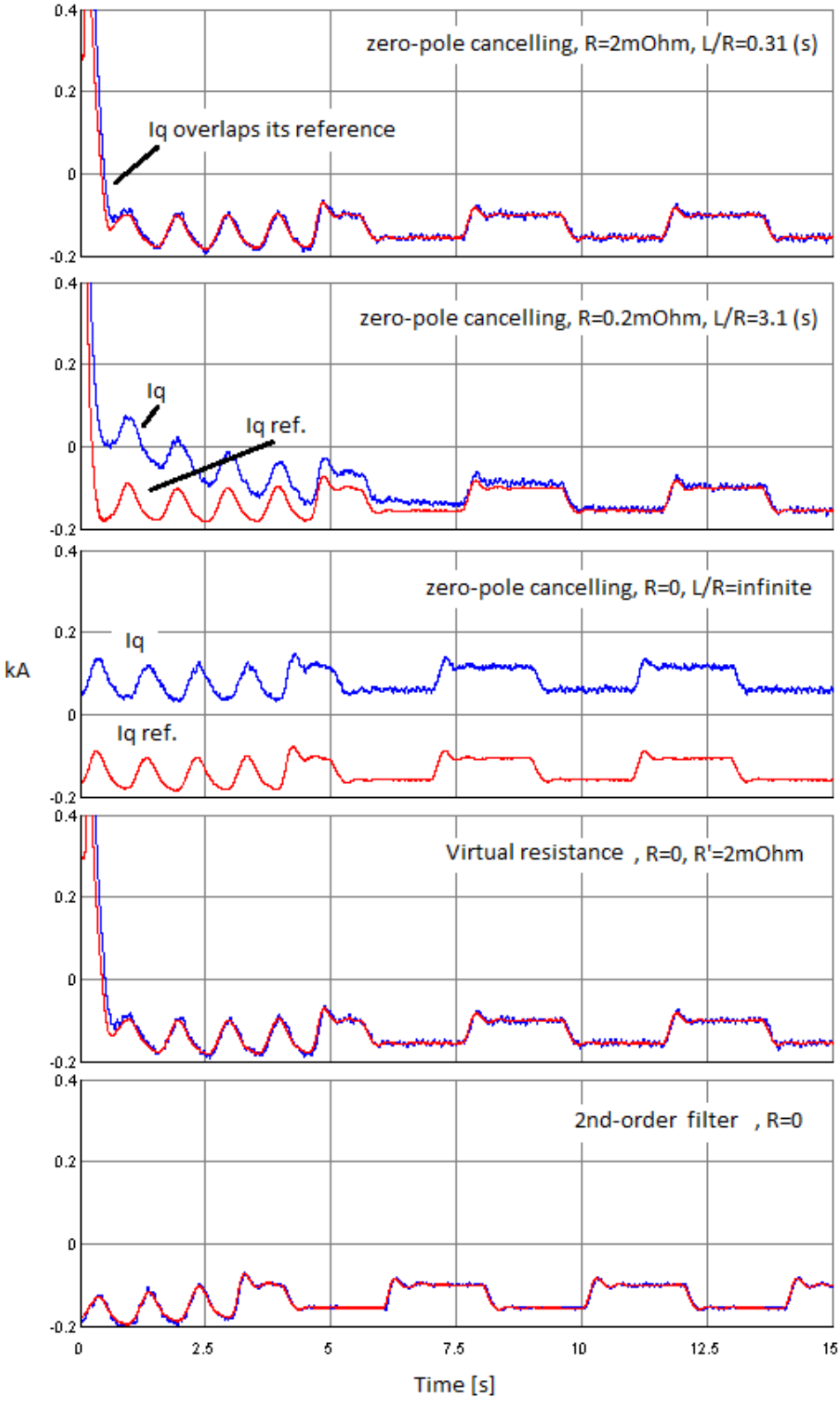

Fig. 3.14 The references and actual values of the q-axis current under five different cases

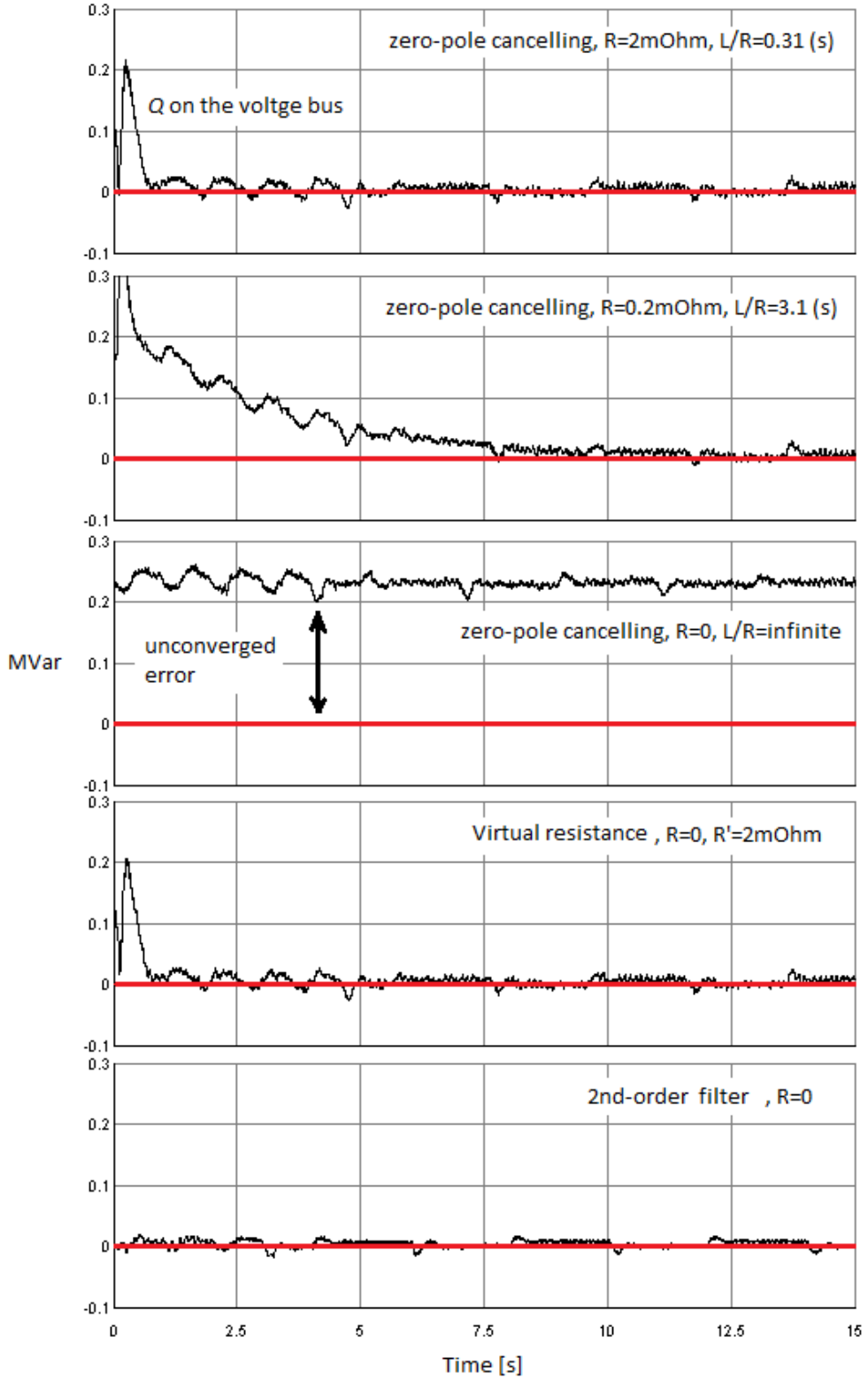

Fig. 3.15 The references and actual values of the reactive power *Q* under five different cases

Summary

This chapter studied how to determine the PI parameters in a dq decoupling control of VSC, especially when there is insufficient converter interface resistance. When the interface resistance *R* and inductance *L* are given, zero-pole cancelling is a popular method to calculate PI parameters. The risks associated with a cancelled pole, in this method, has never been fully discussed before. In this research, using the state-space model, the controllability, observability and the stability of the cancelled pole are studied. The results show that, using the zero-pole cancelling method, the hidden dynamics related to the cancelled pole dominates control performance and makes it converge slowly, or not at all, when there is insufficient *R*. Two methods are proposed to solve this problem, namely the virtual resistance method and the second-order filter. The former relocates the cancelled pole in the s-plane, and the latter removes the hidden dynamics. Both proposed methods can achieve good control performance; regardless of the value of *R*.

CHAPTER 4 INTERMITTENCY, FLUCTUATION AND ENERGY QUALITY OF VARIANT RENEWABLE ENERGY SOURCES

Abstract- This chapter studies the power characteristics of solar, wind and wave energy in terms of their fluctuation and intermittency based on a mixture of real data from experiments and synthetic data from modelling and simulations. In considering the uncontrollable variation of these power sources, the concept of energy quality is proposed to assess how friendly a power flow is to the grid. This is analogous with the conventional concept of power quality used to assess voltage/current waveforms. Energy quality involves two aspects, namely power level and power harmonics. The mathematical definitions and impacts on the grid, of both aspects, are discussed.

4.1 Characteristics of Solar, Wind and Wave energy

4.1.1 Introduction

There are many renewable energy sources, however, this study focuses on the power characteristics of solar, wind and wave power for two reasons. First, compared with other renewable power sources, these three, in common, have a lack of controllability of the variant prime mover power. Second, there are strong correlations between these three renewables. On Earth, the wind is driven by the uneven heating due to incident solar energy, and wave power derives from wind power captured by the surface of a body of water. Accordingly, the

wind and waves could be viewed as the cumulative results of solar power, respectively. It is interesting to study and compare the power characteristics of them in this chain of energy accumulation.

Fig. 4.1 The chain of the renewable energy accumulation

In this study, the power variation of these renewables is classified into fluctuation and intermittency, for they have different characteristics, influences and solutions. Fluctuation is the short-term power variation, in seconds to minutes, that raises problems of frequency stability in the local grid, and thermal excursions and over rating of equipment. Intermittency is the variation and, specifically, the availability, when the power level goes to zero, of the long-term average power, in minutes to hours. This has huge impact on secondary frequency regulation, the steady-state operation of the grid and electricity market operation. The power characteristics of solar, wind and wave energy are discussed below.

4.1.2 Solar Energy

To illustrate the power characteristics of solar energy, two groups of data, for solar power generation, are presented. One group of data is sourced from Elia, the Belgian electrical transmission system operator [93]. It is the real-time estimated data, in 2017, of solar power generation in Belgium; collected at 15 minute intervals. Fig. 4.2 shows solar power generation on 6 consecutive days in February (winter) and August (summer). Fig. 4.3 zooms-

in on the data for 2nd Feb. and 2nd Aug. Another group of data is sourced from Solar Power Data for Integration Studies, the National Renewable Energy Laboratory (NREL), USA, which is synthetic but with the higher resolution of 5 min [94]. Fig. 4.4 shows the solar photovoltaic (PV) power generation in the North Carolina, during 6 consecutive days from 0:00-hours 25th June to 23:55-hours 30th June, 2012. Fig. 3.5 zooms-in on the data for 25th and 30th during daylight-hours only.

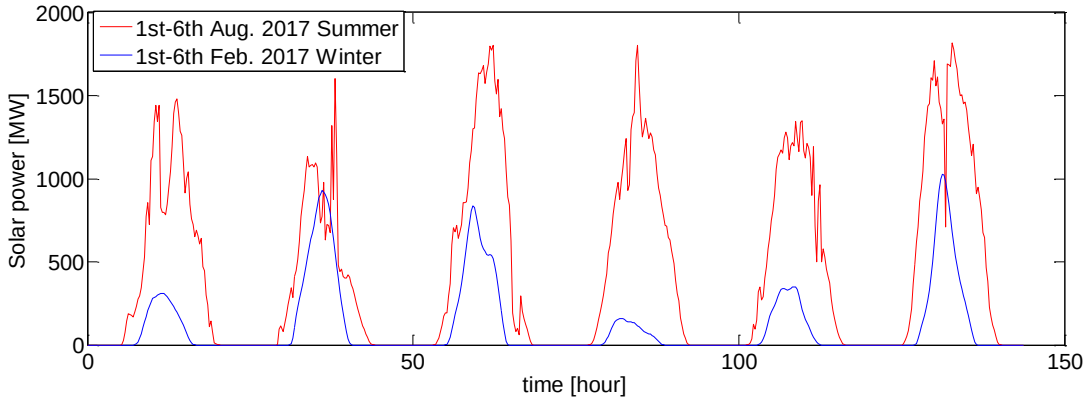

Fig. 4.2 National solar power generation data in six days, Belgium 2017

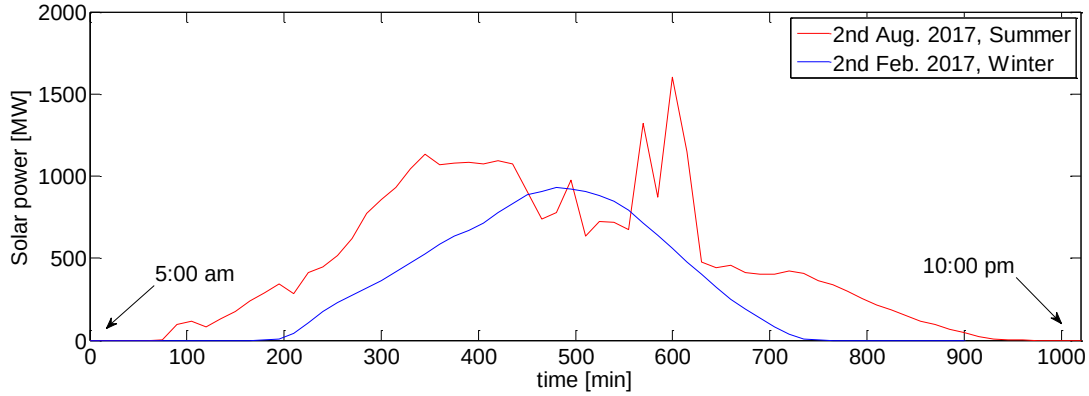

Fig. 4.3 Zoom-in of the solar power data at 2nd Feb. and 2nd Aug., Belgium 2017

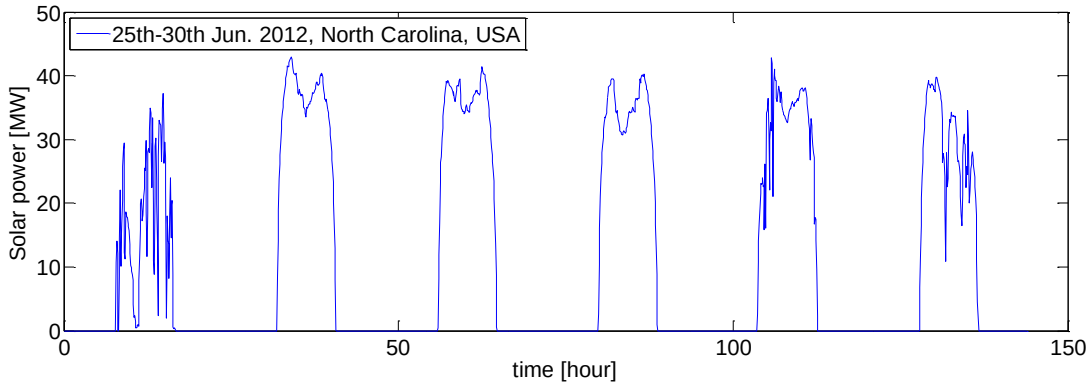

Fig. 4.4 The synthetic solar PV power plant data in five days in the North Carolina, USA

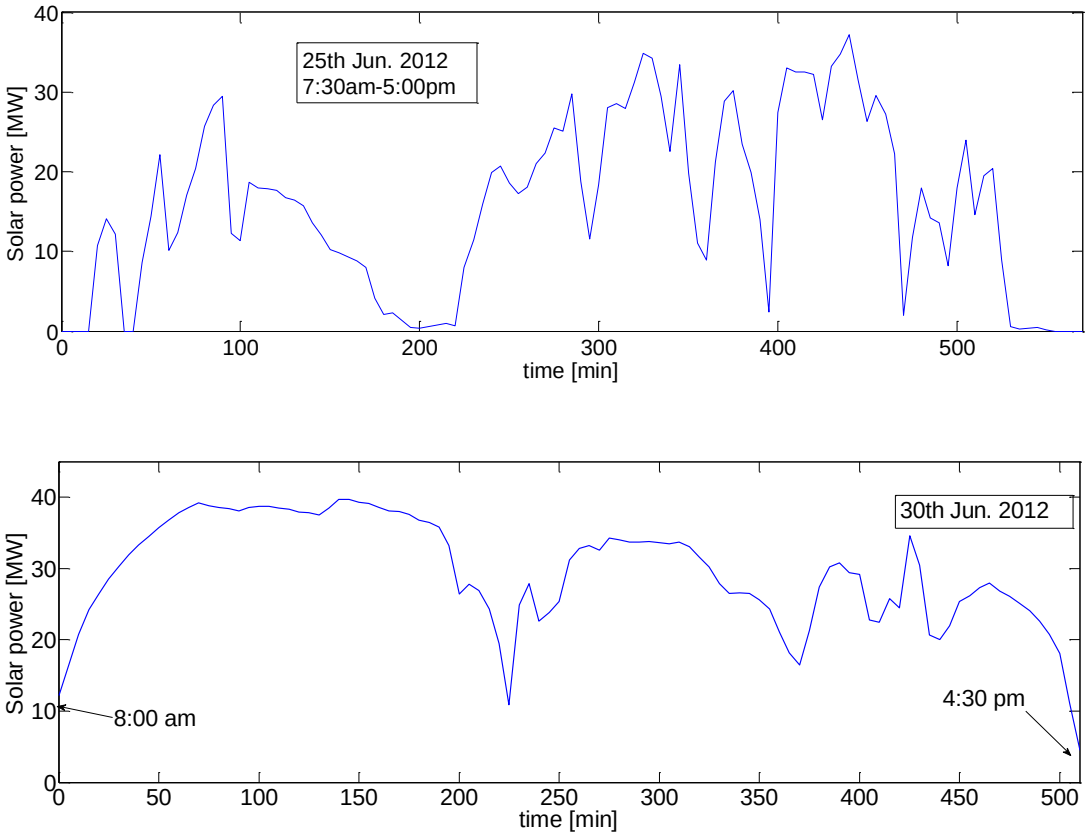

Fig. 4.5 Zoom-in of the solar power data at 25th and 30th June, 2012, the North Carolina, USA

As can be seen from Fig. 4.2 and 4.4, the solar power waveform has a significant intermittency due to the day-night cycle. The average availability of the solar power through

a day in these cases is about 35%~55%, depending on the season, because the sunlight incident on solar-PV panels must be above a threshold value to generate electricity. The solar power also fluctuates in short-term periods due to cloud movements and other weather events. The zoom-in waveforms presented in Fig. 4.3 and 4.5 have been averaged at 15- and 5-minute intervals, respectively. A significant power fluctuation can be observed, even at these resolutions. An enormous quantity of data from the same sources shows similar power characteristics throughout the year.

Solar energy is, indisputably, very intermittent on a day-to-day basis, and also has low-frequency fluctuations on a minute-to-minute basis directly corelated to changing weather events.

4.1.3 Wind Energy

To illustrate the power characteristics of wind energy, long-term and short-term data is presented in days and minutes with different resolutions to show its intermittency and fluctuation, respectively. The long-term data presented in Fig. 4.6 shows the wind power generation from OeMAG, Germany [95] during six days in Feb. and Aug. The mean wind power is measured every 15 minutes.

Two groups of short-term data of wind speed and power generation are presented in Fig. 4.7(a)(b). The real-time wind speed data is obtained from the Aeroelastic Computer-aided Engineering Tool for horizontal axis wind turbines, and then the relevant single-machine wind power data is generated by the RTDS wind generation model built into this study; based on existing modules. The machine model is rated at 350kW. The resolution of the wind speed

data is very high, at about 0.1s, which could be regarded as continuous. One group of data presented in (a) lasts 180s and another group presented in (b) lasts 240s.

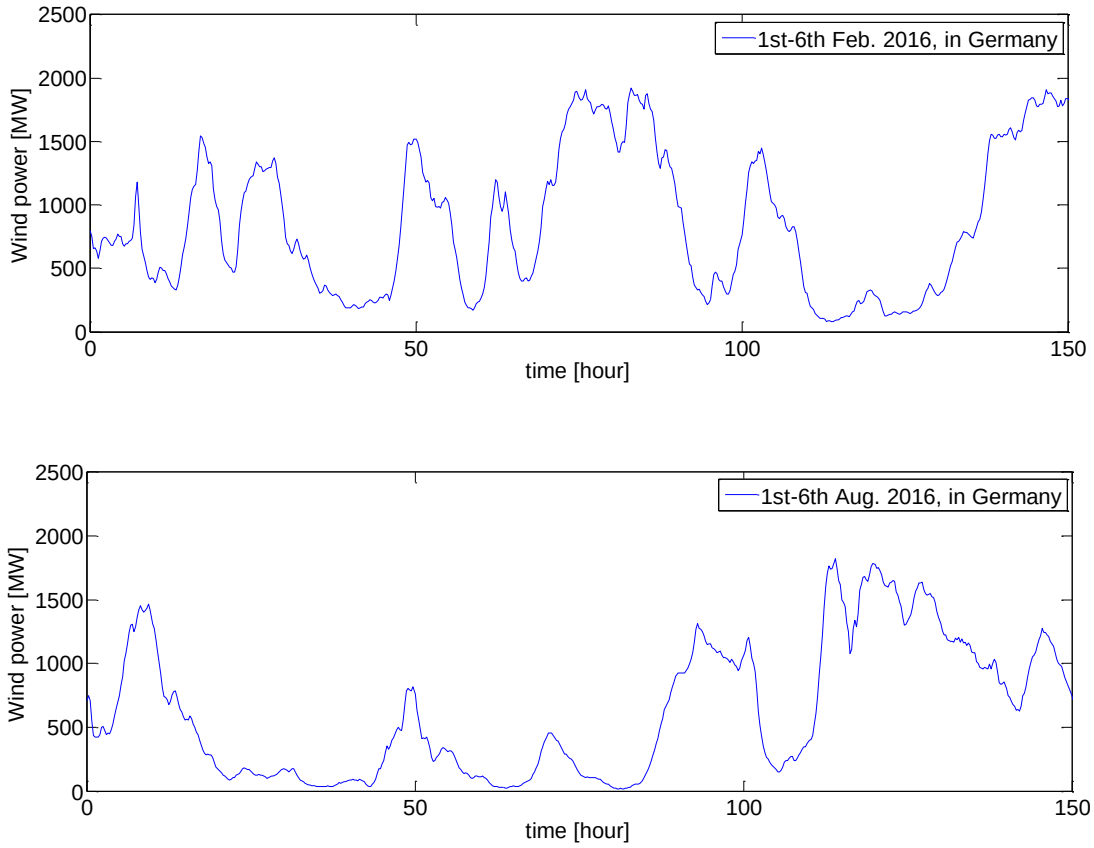

Fig. 4.6 Historical wind power generation during six days from OeMAG, Germany

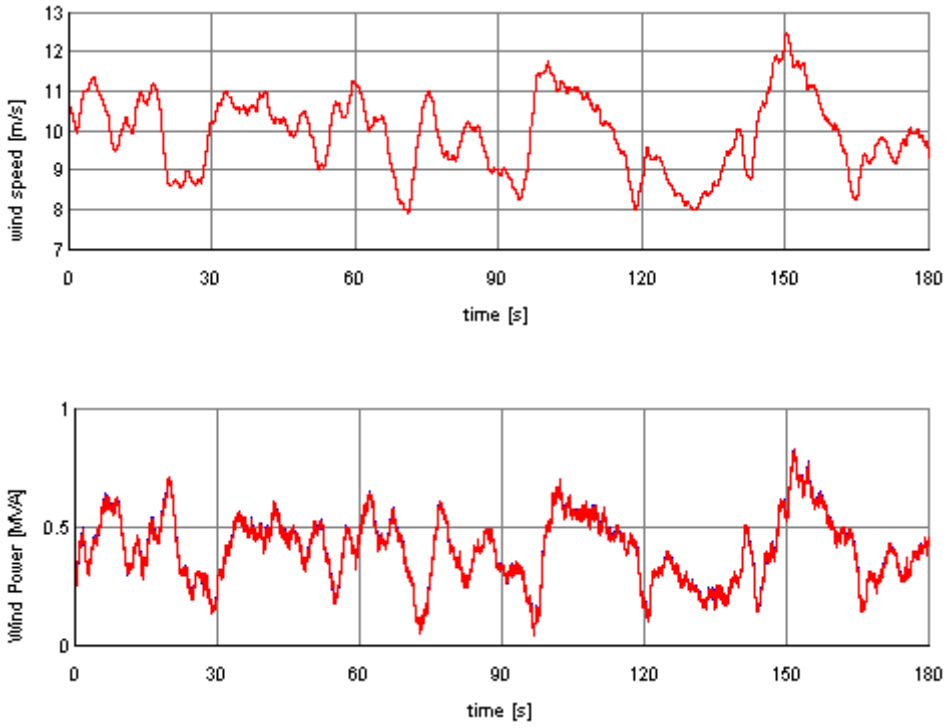

Fig. 4.7(a) The short-term real-time wind speed and power #1 in 180s

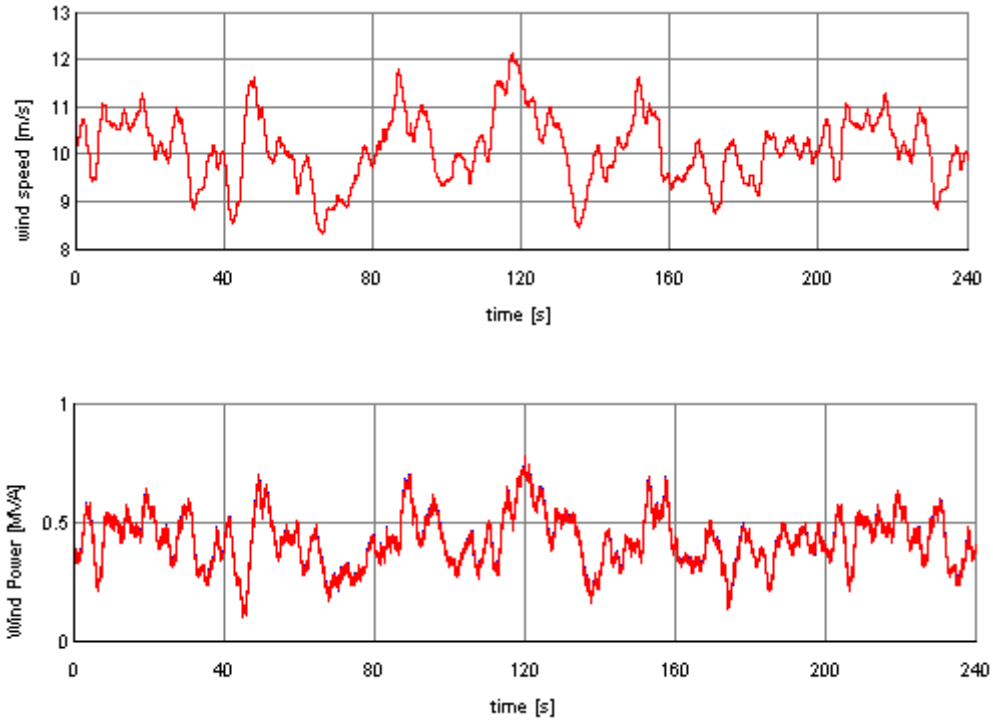

Fig. 4.7(b) The short-term real-time wind speed and power #2 in 240s

From Fig. 4.6, it's seen that the wind energy is very intermittent throughout the day, but it does not have an obvious periodic variation as does solar energy. In a time-scale of minutes, Fig. 4.7 shows that the wind power generation of a single-machine is very fluctuating in a typical range of 0.2~1.8 per unit. Nor is there any obvious periodic change in this fluctuation. It should be noted that this is only the case when the wind turbine operates in the linear range and pitch control is not activated. When wind capture is saturated, the peaks of the fluctuating waveforms, shown in Fig. 4.7, would be automatically levelled by the pitch control.

4.1.4 Wave Energy

Compared with solar and wind, the development of wave power generation is still at an early stage and far from commercialization. For this reason, there is a lack of the wave power data from practical and grid-integrated projects. In academia, however, the nature of the ocean wave has been studied by many previous works and methods have been developed to generate or synthesize the time series of the wave power generation according to the wave spectrum. The wave spectrum is the power spectral density of wave surface displacement (wave height), which is dependent on the wave climate. Most wave power is within the frequency range of 0.05~0.25 Hz, which is equivalent to a period range of 4~20 seconds. The typical period range of the power capture function of a PTO device is 5~12 seconds.

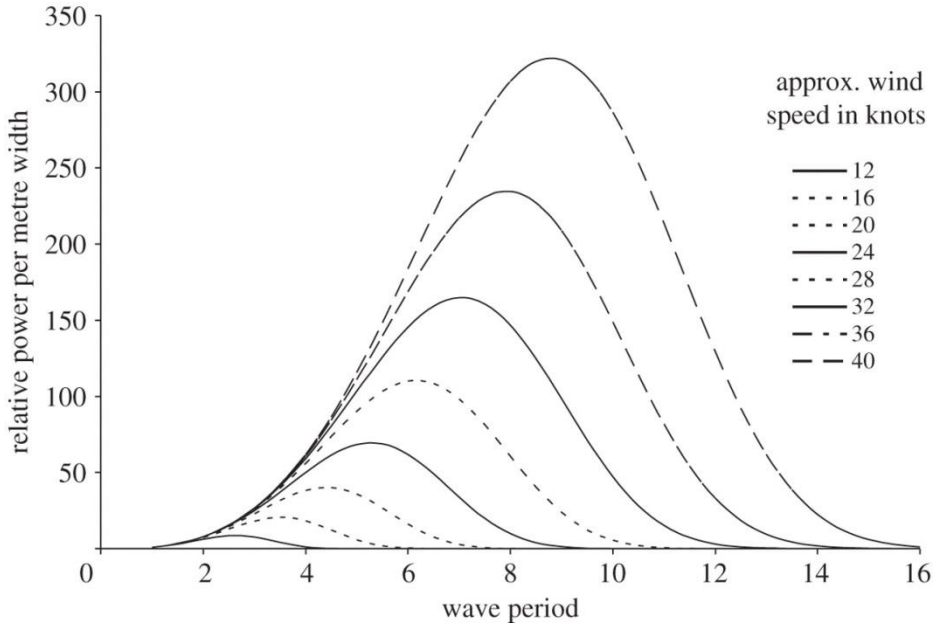

Fig. 4.8 A typical group of wave spectrums for various wind speeds [67]

From the wave spectrum, the wave power is known for its severe periodic fluctuations. These fluctuations in seconds have large magnitudes of about 2.0 per unit, however, the long-term average power of a wave is relatively steady. There is a seasonal change of the long-term power level of waves, which are bigger in winter than in summer.

4.2 The Energy Quality of Variant Energy Sources

4.2.1 The Concept of Energy Quality

Power quality is a well-known concept in the electrical power system. It involves three aspects of the requirements for electricity in the grid: voltage level (magnitude), frequency, and waveforms (harmonics) of voltages and currents. Since the voltage level and the frequency can also be viewed as waveform characteristics, the conventional concept of power quality can be interpreted as a set of requirements of the voltage and current waveforms. The

term “power quality”, however, does not relate to the requirements of the waveform of power.

In this study, the concept of Energy Quality is proposed to describe how friendly, to the grid, is the waveform of power . Compared with voltages and currents, the desired waveform of power is not sinusoidal AC, but DC. Compared with power quality, therefore, the energy quality is a set of requirements of DC waveforms. There are two significant aspects: the power level (magnitude) and power fluctuations (harmonics).

4.2.2 Power Level

The first aspect of energy quality, the power level, is defined as the per-unit average power at any time, and the base power is selected as the rated output power of the renewable power generation unit. The power level of a power waveform in a period time of T is defined, mathematically, as

$$\overline{P}_T(t) = \frac{1}{T}\int_{t-T}^{t} p(\tau) \cdot d\tau \qquad (4.1)$$

where $p(\tau)$ is the per unit power output. For example, normalizing Fig. 4.3 shows the power level of the solar energy when T=5 mins.

To describe the intermittency of a renewable energy source, T is usually set in the range minutes to hours; depending on the needs of applications. A zero-power level means the renewable power source is not available at that time, such as at night for solar power generation. The power level reflects the long-term stability of a power source, and it is desirable to maintain the power level as close as possible to 1.0. Large variations add burdens

to other power sources in the grid and increases waste of the capacity of electrical machines and devices.

4.2.3 Total Power Harmonic Distortion

The second aspect of energy quality, power fluctuation, can be described by the Total Power Harmonic Distortion (TPHD), which can be considered as an extension of the conventional concept, the total harmonic distortion (THD), to the waveforms of power flows. THD of a voltage is defined, mathematically, as

$$\mathrm{THD(t)} = \frac{\sqrt{\sum_{k=2}^{\infty} V_k^2}}{V_1} = \sqrt{\frac{\lim_{T\to\infty} \frac{1}{T}\int_{t-T}^{t} v(\tau)^2 d\tau}{V_1^2} - 1} \qquad (4.2)$$

where V_k is the rms value of the k-th order harmonic of the voltage waveform, V_1 is the rms value of the fundamental, and $v(\tau)$ is the total voltage waveform. Practically, the period T cannot go to infinity but is set to a large value. For a periodic voltage/current waveform, its frequency spectrum is discrete, in which the fundamental is the desired component and the other high-order harmonics are the distortion. There are two important points to be noted when THD is extended to TPHD, to describe the power waveform. First, in most cases, the power waveform is not periodic, thus the discrete frequency spectrum is replaced with a continuous power spectral density. Second, as for power, an ideal waveform is its power level as a DC constant, and all the other harmonics, regardless of frequencies, are regarded as part of the distortion, which provides zero long-term power output. Accordingly, TPHD of a power waveform in a period time of T is defined, mathematically, as

$$\mathrm{TPHD}_T(t) = \frac{\sqrt{2\int_{0^+}^{\infty} S_T(\omega,t)d\omega}}{\bar{P}_T(t)} \tag{4.3}$$

$$S_T(\omega,t) = \frac{1}{T}\left|\int_{t-T}^{t} p(\tau)e^{-j\omega\tau}d\tau\right|^2 \tag{4.4}$$

$S_T(\omega,t)$ is the power spectral density of the power waveform.

According to the Parseval's theorem of the power spectral density, the integration of spectral density and frequency is equal to the integration of the square of the waveform to time, so it can be derived that

$$2\int_{0^+}^{\infty} S_T(\omega,t)d\omega = \int_{-\infty}^{\infty} S_T(\omega,t)d\omega - \int_{0^-}^{0^+} S_T(\omega,t)d\omega$$

$$= \frac{1}{\mathrm{T}}\int_{\mathrm{t-T}}^{\mathrm{t}} \mathrm{p}(\tau)^2 \cdot \mathrm{d}\tau - \bar{P}_T{}^2(t) \tag{4.5}$$

$$\mathrm{TPHD}_T(t) = \sqrt{\frac{\frac{1}{\mathrm{T}}\int_{\mathrm{t-T}}^{\mathrm{t}} \mathrm{p}(\tau)^2 \cdot \mathrm{d}\tau}{\bar{P}_T{}^2(t)} - 1} = \sqrt{\frac{T \cdot \int_{\mathrm{t-T}}^{\mathrm{t}} \mathrm{p}(\tau)^2 \cdot \mathrm{d}\tau}{(\int_{\mathrm{t-T}}^{\mathrm{t}} \mathrm{p}(\tau) \cdot \mathrm{d}\tau)^2} - 1} \tag{4.6}$$

Equation (4.6) gives a useful method to calculate TPHD from the real-time measuring of power flow. A larger TPHD indicates a more sever fluctuation in power, and the power waveform is more distorted from its power level.

In this study, the TPHD is developed from the extension of the conventional THD. However, it is interesting to notice that the proposed TPHD is equal to the coefficient of variation of the

same power waveform. In statistics, the coefficient of variation c_v is defined as the ratio of the standard deviation σ to the mean value μ.

$$c_v = \frac{\sigma}{\mu} = \frac{\sqrt{E(X^2) - \mu^2}}{\mu} = \sqrt{\frac{E(X^2)}{\mu^2} - 1} \tag{4.7}$$

where $E(X^2)$ is the mean value of the squares of data. For the power waveform as a continuous time function from (t-T) to t, we have

$$E(X^2) = \frac{1}{\mathrm{T}} \int_{\mathrm{t-T}}^{\mathrm{t}} \mathrm{p}(\tau)^2 \cdot \mathrm{d}\tau \tag{4.8}$$

$$\mu = \overline{\mathrm{P}}_{\mathrm{T}}(\mathrm{t}) = \frac{1}{\mathrm{T}} \int_{\mathrm{t-T}}^{\mathrm{t}} \mathrm{p}(\tau) \cdot \mathrm{d}\tau \tag{4.9}$$

After appropriate substitution, it is easy to see that TPHD and c_v are the same.

We have discussed using the TPHD of continuous power waveform to describe the power fluctuation in a period of time *T*. In fact, the power intermittency, interpreted as the long-term power variation, could also be described by TPHD with a big enough *T* enlarged to hours. When studying power change over a long time, it is inconvenient and unusual to see the power presented in a continuous time function, but more likely in a group of sampled, averaged, and discrete data. It is necessary to find the discrete expression of TPHD to use TPHD to describe the power intermittency. As has been demonstrated above, TPHD is equal to the coefficient of variation c_v. Thus, for a group of discrete power data $\{p_i | i = 1,2, \dots, N\}$, the TPHD is presented in the discrete form as

$$\mathrm{TPHD}_N = \sqrt{\frac{\frac{1}{N}\sum_{i=1}^{N} p_i^2}{(\frac{1}{N}\sum_{i=1}^{N} p_i)^2} - 1} = \sqrt{\frac{N \cdot \sum_{i=1}^{N} p_i^2}{(\sum_{i=1}^{N} p_i)^2} - 1} \qquad (4.10)$$

Table. 4.1 Summary of the comparison between energy quality and power quality

	Power quality analogy	Energy quality	Continuous form	Discrete form
Magnitude	Voltage level	Power level	$\overline{\mathrm{P}}_{\mathrm{T}}(\mathrm{t}) = \frac{1}{\mathrm{T}}\int_{\mathrm{t-T}}^{\mathrm{t}} \mathrm{p}(\tau) \cdot \mathrm{d}\tau$	$\overline{\mathrm{P}}_{\mathrm{N}} = \frac{1}{\mathrm{N}}\sum_{i=1}^{N} p_i$
Harmonics	THD	TPHD	$\mathrm{TPHD}_T(t) = \sqrt{\frac{T \cdot \int_{\mathrm{t-T}}^{\mathrm{t}} \mathrm{p}(\tau)^2 \cdot \mathrm{d}\tau}{(\int_{\mathrm{t-T}}^{\mathrm{t}} \mathrm{p}(\tau) \cdot \mathrm{d}\tau)^2} - 1}$	$\mathrm{TPHD}_N = \sqrt{\frac{N \cdot \sum_{i=1}^{N} p_i^2}{(\sum_{i=1}^{N} p_i)^2} - 1}$

Summary

In this chapter, a mix of real, simulated and synthetic data has been presented in large and small timescale to discuss the characteristics of the time series of the solar, wind and wave power generation in terms of their intermittency and fluctuation. Solar power is significantly intermittent on a diurnal cycle and also fluctuates on a minute-to-minute basis. Wave power is significantly fluctuating with a typical wave period of 4-20s, however, wave power has very little intermittency and very high availability through a year. Wind power has moderate intermittency and fluctuation; lying in between solar and wind. To describe these power

variations mathematically, the concept of energy quality has been proposed; analogous to conventional power quality used to describe voltage/current waveforms. The two indices of energy quality, namely the power level and the total power harmonic distortion (TPHD), were defined.

CHAPTER 5 ENERGY FILTERS

Abstract- Filters are common and useful in both the area of signal processing and power systems to control and manage waveforms. Passive and active power filters are conventionally used in a power system to improve the waveforms of voltages and currents, but they have never yet been applied to the waveforms of power flows. In this chapter, an energy filter is proposed as a tool to control and manage the waveforms of power flows as part of the concept of energy quality, which was discussed in Chapter 4. The proposed energy filters can process and smooth the power flows as conventional filters do to electric signals, voltages and currents; and they are particularly useful in handling the power fluctuation and oscillation caused by fluctuating renewable power sources. Electrical energy storage (EES) systems are briefly reviewed at the beginning of this chapter, as they are necessary parts for building energy filters. A time domain demonstration of energy filters in different topologies and the relevant quantitative analysis is presented.

5.1 Introduction

One key problem in the control and operation of the power system is to achieve the balance between the generation and the loads. This problem is becoming more challenging as the penetration of the intermittent and fluctuating renewable power sources keeps increasing; this not only increases the uncertainty of generation, but also reduces the inertia and damping of the whole power system. For this reason, managing and controlling the uncertain and fluctuating power flows from renewable power sources is vital and in this study energy filters are proposed to address this.

In signal processing, low-pass filters remove the unwanted high-frequency components from the signals. For example, most of the measured signals have to go through the filters to eliminate the high-frequency noises before they reach the receiver. Practically speaking, the signals become more smoothed after the filters. This process shares a similar objective with the power smoothing control, in which the high-frequency power fluctuations and oscillations are removed and the smoothed power flow should remain with the same average level after this removal. In power systems, both the passive and active "power filters" are well-known tools that manage and control the quality of voltage and current waveforms; however, this does not apply to the waveforms of power flows. The ideal waveform of a voltage or current is sinusoidal in a single frequency, while that of a power flow is expected to be a constant DC. However, the concept of the use of a filter has not yet been used in the management of the power flows.

A group of control systems based on EES is proposed in this study and they are virtually operated as low-pass filters of power flows. They are named as energy filters (EFs) to avoid confliction with the existing power filters used for AC voltages and currents. One advantage of the proposed energy filter, as will be discussed in detail later, is that it can be built on most of the light EES systems, such as SMES, flywheels, ultracapacitors, and batteries, independently from its control methods. For this reason, the proposed filter is also called the "general energy filter" (GEF) in the published paper of this work [68]. Like filters used in signal processing, the energy filters also have their transfer functions, cut-off frequencies and Bode plots. They could be very useful in power smoothing control and tracking without measurements of the input power. Comparatively, the proposed energy filters are able to manage and control the power flows and improve their energy quality as discussed in the last

chapter, as the conventional passive and active power filters can improve the power quality of voltages and currents.

5.2 A Simplified Power-based Model of EES

Energy follows the law of conservation which cannot be eliminated, or created like signals. For this reason, the energy filter must consist of an EES system as a pool for the fluctuating power flow, which is expected with zero average values. In the following sections, firstly, the mainstream EES systems are briefly reviewed and classified, particularly in terms of their efficiency and capacity. Then, a simplified and power-based model of an EES system is built as the preparation for the development of the energy filters.

5.2.1 EES Classification: Light and Heavy Storage

In this research the mainstream EES systems are classified into six groups in a new framework of light and heavy storage: thermal, chemical, electrochemical (batteries), electromagnetic, kinetic mechanical and potential mechanical energy storage. They are further labelled as light or heavy storage in accordance with their efficiency, capacity and compatibility with energy filters.

Some literature studies [36, 96] give comparative reviews on different EES systems. In contrast to [36] solar fuel, as a solar-chemical energy conversion device, is not included in the framework in this research because it has very limited direct interactions with power systems. Flywheel energy storage (FES) is recognized as a kinetic mechanical energy storage device which is largely different from potential mechanical storage in terms of its characteristics. Besides the CAES and the PHS, the undersea storage is also new potential mechanical storage [97, 98] whose energy cycle efficiency is similar to that of PHS. As for

chemical storage, the conventional methods are mainly based on hydrogen electrolysis and fuel cells to achieve a bi-directional conversion between hydrogen and electrical energy. The latest development of a new method of converting CO_2into $CH_4$by consuming electricity is also presented in [99]. Thermal energy storage (TES) for utility-scale applications is discussed in [100] whose cycle efficiency is approaching 66%.

Table 5.1 EES classification in the framework of light and heavy storage

Electric Energy Storage System			
Heavy Storage	**Potential mechanical** -Pumped-hydro -Compressed air -Undersea storage [19][20]	**Chemical** -Hydrogen -CO2-CH4 [21]	**Thermal** -PHES [22]
Light Storage	**Kinetic mechanical** -Flywheel	**Electrochemical** -Li-ion battery -Lead-acid, NiMH, … -Flow battery	**Electromagnetic** -Supercapacitor -SMES

In this research, the six groups of EES systems are labelled as either light or heavy storage as was indicated in Chapter 1 and at the beginning of this chapter. In order to develop energy filters, the total energy capacity, the response time and the energy cycle efficiency of the EES systems are three indexes of especial interest. Among the heavy storages, pumped-hydro storage and undersea storage have the highest energy cycle efficiency of about 85%. For CAES, it is about 42-54%; and that of the advanced adiabatic CAES can reach 70%. For the hydrogen fuel cells, it is between 20-66%. For most of the TES, it is about 30-60%. In conclusion, no heavy storage has a cycle efficiency higher than 85%. [36, 96] The response

time of the heavy storage is at least several minutes and not for fast responses. The total energy capacity of the heavy storage is about 0.5-8 GWh for the pumped-hydro; 10 kWh for the over-ground small CAES; 1 GWh for the underground large-scale CAES; and up to 39 MWh under development for the fuel cells. In conclusion, it is from the tens of MWh to several GWh for most of the heavy storage. On the other hand, as has been discussed in detail in Chapter 2, the light storage normally has the energy cycle efficiency of over 90% and can reach up to 97%. It has quick responses and the response time goes from milliseconds to less than one second. The total energy capacity of light storage is mainly between 0.1 kWh to 8 MWh, which is one to a hundred thousand times smaller than heavy storage. [36]

The differences between light and heavy storage are concluded as below. Heavy storage usually has a bigger total energy capacity, slower response and lower energy cycle efficiency. Furthermore, the chemical storage is difficult to bi-directionally interact with the power system for the charging and discharging processes must be conducted based on different and separated devices. By comparison, the light storage has a smaller capacity, faster responses and higher energy cycle efficiency. It is also more compatible with the power system for it can easily achieve bi-directional power flows. For these reasons, the light and heavy storage will be used in different applications. The light storage is preferred in the short-term and small-scaled applications, such as the supplementary damping of power oscillations, primary frequency stabilization and creating virtual inertia. The heavy storage, on the other hand, is preferred for long-term and large-scale applications such as peak load shifting, economic operations of the grid, secondary frequency regulation and the utility scale long-term energy storage. Especially in the light storage applications, the directions of power flows change rapidly and the control and operation of EES must be fast and accurate; thus, the high energy

cycle efficiency and the fast response are critically in demand. Since the proposed energy filter shares characteristics with short-term applications, the power-based model is mainly developed for the light storage; yet for completeness the PHS and CAES can also be described by this model.

5.2.2 The Simplified Power-based Model

A simplified power-based model is developed in this subsection based on the classification of EES above. This model can be used to describe not only light storage, but also PHS and CAES inclusively. Generally speaking, the dynamics of an EES device can be described by three variables: the flow variable φ, the potential variable σ, and the inertia of potential K_σ. Table 5.2 shows these three general variables in different EES systems. The ratio of the actual energy stored in the EES to the rated energy E_0 is called the storage level α. For the light storage (except the battery), PHS and CAES, there is

$$\varphi = K_\sigma \frac{d\sigma}{dt} \tag{5.1}$$

$$P_S = \sigma \cdot \varphi \tag{5.2}$$

In the above equations, P_S is the transferred power between the EES devices and the power system.

Regarding to Table 5.2, these mathematical relationships could be verified straightforwardly for the FES, supercapacitor and SMES-based EES.

Table 5.2 Potential and flow variables in different EES systems

Energy storage type	**Potential** $\boldsymbol{\sigma}$	**Flow** $\boldsymbol{\varphi}$	**Inertia of potential** $\boldsymbol{K_\sigma}$	**Rated stored energy** $\boldsymbol{E_0}$	**Storage level** $\boldsymbol{\alpha}$
Supercapacitor	u_C	i_C	C	$\frac{1}{2}K_\sigma\sigma_0^2$	$\frac{\sigma^2}{\sigma_0^2}$
SMES	i_L	u_L	L		
Flywheel	ω	T	J		
Compressed air	p_C	V_φ	$(N_A V_0)$ $/(R\rho_A T_A)$		
Pumped-hydro	h	G_φ	$\rho_w g S$		
Battery	electrochemical potential	electron/ion flow rate		E_0	$f_\alpha(SoC)$ $\approx SoC$

* Nomenclature of variables is presented in Appendix D.

For the CAES, the inertia K_σ is not only related to the volume V_0, but also to the environmental temperature T_A and the gas density ρ_A. These two cannot be regarded as constants but variables that may change every several hours. For the PHS, the inertia K_σ is proportional to the surface area of the water, that is neither always constant with a time-variant water level. These non-linearity and parameter uncertainties call for extra considerations when it comes to the PHS, CAES and other heavy storage; these have not been covered in this research yet but could be investigated in the future.

The inertia of potential that makes the rated stored energy of the batteries also shares a similar form with other energy storage listed in Table 5.2. The storage capacity or the rated stored energy is given by the manufacture. The storage level of a battery is related to its SoC

which is given by (5.3), in which a_1 and a_0 are two constants obtained from the open-circuit experiments. [101] In most cases, a_0 is much larger than a_1 ($a_1 \ll a_0$), thus the storage level is equivalent to the SoC, especially when the SoC is not too small.

$$\alpha_{Battery} = f_\alpha(SoC) = \frac{a_1 SoC^2 + 2a_0 SoC}{a_1 + 2a_0} \approx SoC \tag{5.3}$$

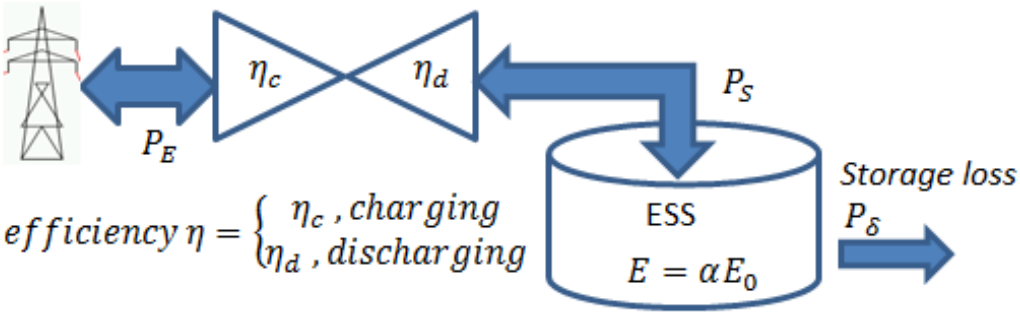

Fig. 5.1 An illustration of the power-based model

The power-based model of an EES listed in Table 5.2 can be illustrated by Fig. 5.1, in which P_δ is the storage loss and η is the energy round-trip efficiency. According to these power flow relationships, there are

$$\frac{dE}{dt} = E_0 \frac{d\alpha}{dt} = P_S - P_\delta \tag{5.4}$$

$$P_S = \begin{cases} \eta_c \cdot P_E & charging \\ \dfrac{1}{\eta_d} \cdot P_E & discharging \end{cases} \tag{5.5}$$

In cases when P_δ is small enough to be ignored with given self-discharge rates and time scales, by substituting (5.1), (5.2) to (5.4), there is

$$E = \int \sigma \cdot K_\sigma \frac{d\sigma}{dt} dt = \frac{1}{2} K_\sigma \sigma^2 \tag{5.6}$$

So except the batteries, for all the EES systems listed in Table 5.2, the storage level α is linear with σ^2 when the inertia of potential K_σ is considered as a constant parameter.

The storage level, potential, flow and inertia variables presented in Table 5.2, together with the equations (5.4) and (5.5) build a simplified power-based model of an EES system, which lays the foundation for the development of energy filters in the next section.

5.3 Development of Energy Filters

5.3.1 Definition of the Energy Filter

The modular block that eliminates components of undesirable frequencies from a signal is called a **filter**. In a more general context, as a fundamental kind of signal processor, a filter completely or partially suppresses some aspects of a signal. Conventionally in a power system, the **power filter** eliminates undesirable components in the voltage and current waveforms to improve the power quality. As proposed in this study, an **energy filter** is a filter that eliminates undesirable power components with zero-average values in power flows to improve the energy quality. As discussed in Chapter 4, compared with power quality which assesses the voltages and currents, the energy quality will assess the power flow waveforms.

The energy filters developed in this study belong to a particular family of EES control systems. There are a variety of energy filters based on different filter orders and topologies. In the following subsections, the first-order series, parallel and hybrid energy filters are presented. The high-order cases are also discussed. The energy cycle efficiency in these cases is assumed as 1.0 and the storage loss is neglected. The impacts of the conversion losses on the energy filters are discussed in section 5.3.6.

5.3.2 Series Energy Filter (SEF)

A series energy filter directly controls its output power, which is its distinctive difference from the parallel energy filter to be discussed in the next subsection. In a SEF, the fluctuating input power and the smoothed output power are separated by the energy storage device. Fig. 5.2 shows the topology of the SEF. Examples of the SEF include the generator with a rotor flywheel and the back-to-back converter, in which the rotor flywheel and the DC capacitor work as the energy storage, respectively. In the given example of the capacitor storage, since the DC-link voltage can only change in a small range, the capacitor needs to be very large to store and release enough energy. We can also use a DC/DC converter to decouple the voltage of the DC-link and that of the capacitor storage, so that the capacitor voltage can change in a large range. In the latter case, the whole system is still a SEF as long as the output power of this energy filter is directly controlled by the inverter.

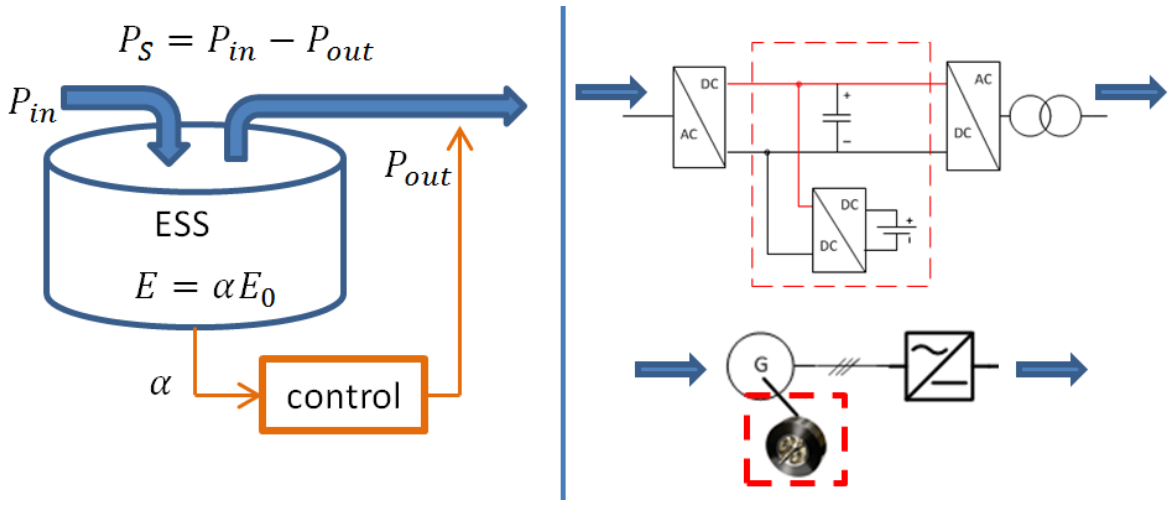

Fig. 5.2 The examples and topology of the SEF

When the storage loss is ignored, from (5.4) we have

$$E_0 \frac{d\alpha}{dt} = P_S = P_{in} - P_{out} \tag{5.7}$$

The control reference of P_{out} is determined as

$$P_{out}^*(t) = \frac{E_0}{T}(\alpha(t) - \alpha_0) + P_0 \tag{5.8}$$

in which α_0 is the rated storage level and P_0 is a long-term estimation of the output average power; P_0 is determined from either online/offline estimation methods or the historical data of sites. It is considered as a piecewise constant in this study, which changes slowly along with the long-term average level of the input power. It is assumed that the real-time output power tracks the reference so fast that $P_{out}^* = P_{out}$. From (5.8) and (5.7), there are

$$T \frac{dP_{out}}{dt} = P_{in} - P_{out} \tag{5.9}$$

$$\frac{P_{out}}{P_{in}} = \frac{1}{sT + 1} \tag{5.10}$$

From (5.8), the real-time storage level α and its sensitivity are

$$\alpha(t) = \frac{T}{E_0}(P_{out}(t) - P_0) + \alpha_0 \tag{5.11}$$

$$\frac{d\alpha}{dP_{out}} = \frac{T}{E_0} = \frac{1}{E_0 \omega_0} \tag{5.12}$$

Conclusively, (5.10) is the transfer function of the first-order SEF; T is the time constant which could be arbitrarily set; (5.8) is the control reference of the output power. To achieve this control, it only needs to measure the storage level α.; (5.11) promises that α would swing around the rated value; and (5.12) shows how sensible the storage level is when the output

power of the energy filter changes. This is called the storage level sensitivity. From (5.12) we can see that a larger time constant and a smaller rated capacity lead to a larger sensitivity.

As has been said, the first feature of the SEF is that it directly controls its output power. The second feature and also a big advantage is that there is no need to measure the input power to build it. These two features are important when compared with the parallel energy filter. With the cut-off frequency $\omega_0 = 1/T$, the SEF is virtually operated as a low-pass filter of power flows. The high-frequency fluctuation of the unknown input power is filtered out by the EES, while the output power is smoothed.

5.3.3 Parallel Energy Filter (PEF)

By contrast with the SEF, the output power of a PEF is not directly controlled and the input and output power are not separated but more in coherence. The smoothed output power could be regarded as a summation of the fluctuating input power and the compensating power from the EES, both of which are connected to the power bus in parallel. Fig. 5.3 shows the topology of the PEF. Examples of PEF structures include flywheel storage or the inverter-based battery storage system on the power bus in parallel with any fluctuating renewable generation.

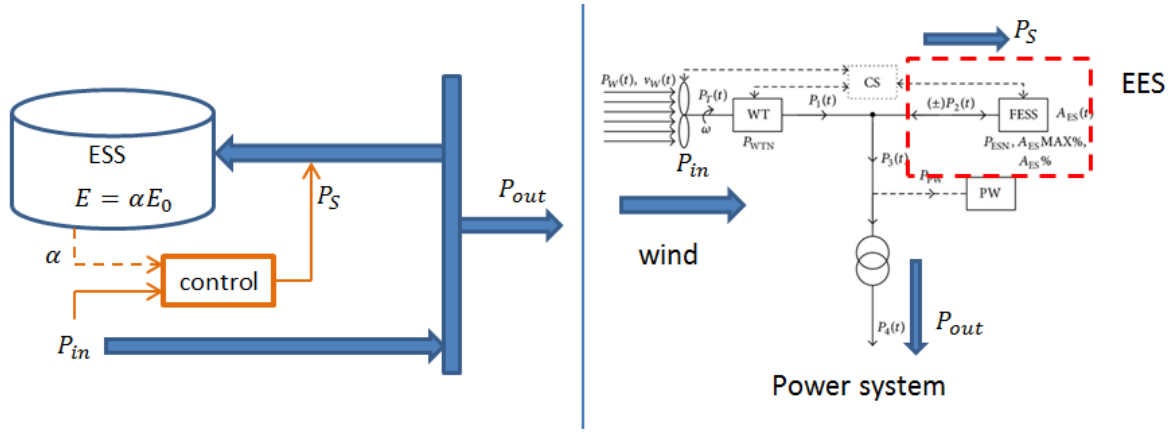

Fig. 5.3 The examples and topology of the PEF

The controller always gives the reference of P_{out}. However, a PEF directly controls only P_s, not P_{out}, so the input power P_{in} must be measured in a PEF to obtain the control reference of $P_s^* = P_{in} - P_{out}^*$. There are two candidates for the control references of P_S based on whether the storage level α needs to be measured.

Single-measurement control

In the single-measurement control only the input power P_{in} is measured and it doesn't require the information of α or E_0. However, in this method the storage level is completely not controllable.

According to Fig. 5.3, the power flows still can be described by equation (5.7). However, the power directly controlled by the energy filter is not P_{out} but P_S. The control reference of P_S now is

$$P_S^*(t) = \left(1 - \frac{1}{Ts+1}\right) * P_{in}(t) \tag{5.13}$$

Once again it is assumed that the voltage and current loops are so fast that $P_S = P_S^*$. According to (5.7) and (5.13), the transfer function of PEF is still presented as (5.10). However, without the controllability of the storage level α, we only know its derivative as

$$E_0 \frac{d\alpha}{dt} = T \frac{dP_{out}}{dt} \tag{5.14}$$

$$\alpha = \frac{T}{E_0} P_{out} + \alpha_{ini} \tag{5.15}$$

The initial state of the storage level α_{ini} appears by integrating (5.14), which is excluded by the control loop and makes α vulnerable to the disturbance. For this reason, this control method is undesirable in most cases, unless additional protection and monitoring of α is applied. This method however, is of simple structure and control and could be useful when the fluctuating power is not filtered out by the EES but another power source. Details of this are discussed in section 5.6.1.

Double-measurement control

In the double-measurement control, both the input power P_{in} and the storage level α are measured, and it is also necessary to know E_0. The advantage is it can control α within the accepted range. Based on Fig. 5.3, the control reference is set as

$$P_S^*(t) = -\left[\frac{E_0}{T}(\alpha(t) - \alpha_0) + P_0\right] + P_{in}(t) \tag{5.16}$$

Under this control reference, the transfer function, the storage level $\alpha(t)$ and its sensitivity to the output power are equivalent with (5.10)-(5.12).

A method to estimate P_0 assumes that it equals to the average value of P_{in} in the long term. Based on this assumption, the control reference (5.16) could be written as

$$P_0 = \frac{1}{T_{in}s + 1} * P_{in}(t) \tag{5.17}$$

$$P_S^*(t) = -\frac{E_0}{T}(\alpha(t) - \alpha_0) + \left(1 - \frac{1}{T_{in}s + 1}\right) * P_{in}(t) \tag{5.18}$$

in which T_{in} is the average input time constant that is much larger than T.

5.3.4 Hybrid Energy Filter (HEF)

For the SEF and the PEF, the fluctuating input power can go through only one pathway. Comparatively, an HEF is in an over-position of both of these, it has two pathways for the input power. Fig. 5.4 shows the topology and an example of the HEF. The example is a renewable power generation system consists of two PMSGs controlled by full rated converters as the series pathway and a group of induction generators directly connected to the power bus as the parallel pathway. It is similar with the wave farm system discussed in Chapter 6. The series pathway is in the form of a SEF that directly controls its output power $P_{out,s}$. The parallel pathway directly connects the input power to the power bus. Similar to the PEF, the total output power P_{out} on the power bus is not directly controlled.

The control reference of $P_{out,s}$ is

$$P_{out,s}^*(t) = \left[\frac{E_0}{T}(\alpha(t) - \alpha_0) + P_0\right] - P_{in,p}(t) \tag{5.19}$$

The control of the HEF is similar to that of the PEF; it requires the information of the storage level α, the power flow through the parallel pathway $P_{in,p}$ and the rated storage capacity E_0.

As a hybrid, the HEF takes advantages from both the series and parallel EF. It does not need to measure the input power through the series pathway, while the EES system does not have to prepare the transmission capacity for the power through the parallel pathway.

With the assumption that $P^*_{out,s}(t) = P_{out,s}(t)$ and according to (5.7), the transfer function, the storage level and the sensitivity to the output power are equivalent to (5.10) - (5.12).

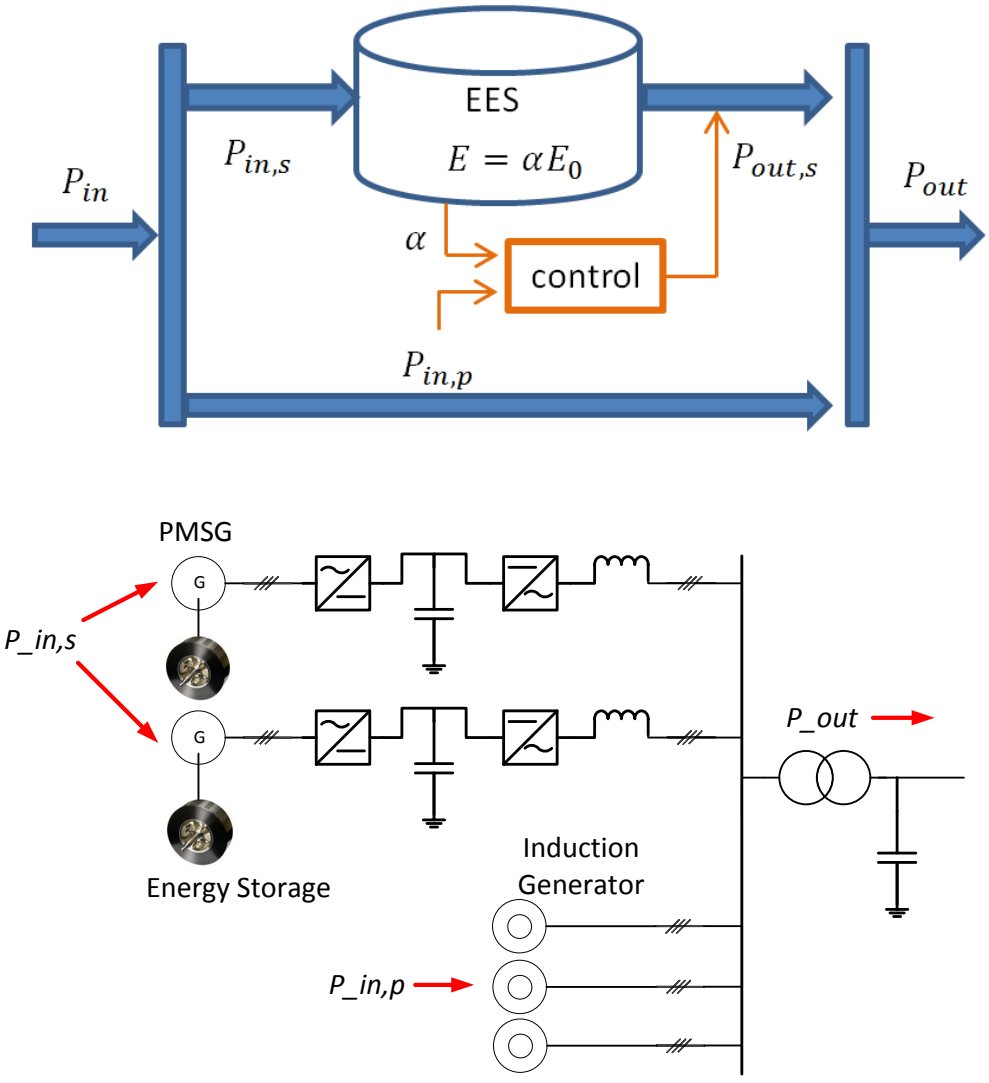

Fig. 5.4 The topology and an example of the HEF

5.3.5 Second-order HEF

The energy filters discussed above are first-order. The second-order energy filter can be achieved by simply changing the control reference of the output power of the EES. The HEF is studied as an example case in this subsection.

Based on Fig. 5.4, the control reference of $P_{out,s}$ to achieve a second-order HEF is written in the s-domain as

$$P_{out,s}^{*}(s) = \left[\frac{E_0}{2T}\left(\frac{1}{Ts+1}\cdot\alpha(s) - \frac{\alpha_0}{s}\right) + \frac{P_0}{s}\right] - P_{in,p}(s) \tag{5.20}$$

Again, based on (5.7) and the assumption that $P_{out,s}^{*} = P_{out,s}$, the transfer function of a second-order HEF is

$$\frac{P_{out}}{P_{in}} = \frac{\frac{1}{2T^2}}{s^2 + \frac{s}{T} + \frac{1}{2T^2}} \tag{5.21}$$

It is in the standard form of a second-order low-pass filter with a damping ratio of $\xi = 1/\sqrt{2}$ and a cut-off frequency of $\omega_0 = 1/\sqrt{2}T$. The damping ratio is set as its minimum value without the resonance.

At steady-state, the storage level α is

$$\alpha = \frac{2T}{E_0}(P_{out} - P_0) + \alpha_0 \tag{5.22}$$

The storage level sensitivity is

$$\frac{d\alpha}{dP_{out}} = \frac{2T}{E_0} = \frac{\sqrt{2}}{E_0\omega_0} \tag{5.23}$$

In section 5.4, simulation results demonstrate that the second-order energy filter has better power smoothing effects than the first-order filter. The drawback is that the storage level is more sensitive to the output power.

5.3.6 Model Uncertainty Due to the Conversion Loss

In a real energy filter, the conversion loss appears when the energy cycle efficiency is not 100%. It raises non-linearity and uncertainty of the power-based model. According to (5.5), when the conversion loss is taken into account, the dynamics of α become

$$\frac{E_0}{k_\eta} \cdot \frac{d\alpha}{dt} = E_0' \frac{d\alpha}{dt} = P_{in} - P_{out} \tag{5.24}$$

$$k_\eta = \begin{cases} \eta_c & charging \\ \dfrac{1}{\eta_d} & discharging \end{cases} \tag{5.25}$$

Accordingly, the conversion loss leads to an uncertain and time-variant E_0', whose average value is $\overline{E_0'} \in [\eta_d E_0, \frac{E_0}{\eta_c}]$. Physically, this means: when the energy storage module releases/absorbs electrical power, the equivalent inertia of the energy storage becomes smaller/larger. Based on the simulation experiences in this study, E_0 itself is a good approximation of $\overline{E_0'}$ with little impact on the behaviours of energy filters, as long as the round-trip efficiency is higher than 90%. This approximation has been validated in simulations of energy filters using flywheel, ultracapacitor and Li-ion battery energy storage. Details of these simulations are presented in Section 5.4. This indicates a critical limitation of the energy filter, which in most cases can only be built on light storage with high efficiencies. The feasibility of EES systems to build an energy filter decreases dramatically when the

round-trip efficiency is so low that the transfer functions and mathematical relationships discussed above no longer stand.

5.4 Case Studies of Energy Filters

In this section, the proposed energy filters are demonstrated in different cases by simulations on RTDS. In the following cases, the structure of the hardware, the real-time storage level, and the input and output power of each kind of energy filter are presented. The output power of the energy filters goes to an infinite grid. Although theoretically, an energy filter can be built based on a variety of EES systems, not all the possible cases but a selection of energy filters with different topology, order, EES and control are presented in this study. Simulation parameters of models presented in Fig. 5.5, 5.8 and 5.11 are listed in Appendix B.

5.4.1 First-order SEF Based on the Supercapacitor

An SEF is built on supercapacitor energy storage in this subsection. The EES is connected to the DC side of a back-to-back VSC. The rated storage capacity $E_0 = \frac{1}{2}CV_c^2$ is 0.22 kWh, $V_c = 4\ kV$ and $C = 100mF$. The input power fluctuation is sinusoidal and its frequency is 0.5 Hz, which equals the cut-off frequency of the SEF. The supercapacitor energy storage is controlled to keep the DC voltage constant so that the input and output power of the energy filter are independent. The purpose of this simulation is to demonstrate that the energy filter does work as a low-pass filter of the power flow. The Bode plot of the SEF is shown in section 5.4.4. The real-time power flows are presented in Fig. 5.6, in which there is a 45° phase shift between the input and output as indicated by the theory.

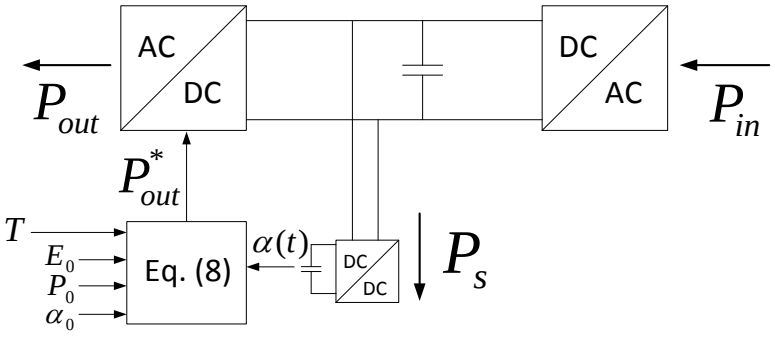

Fig. 5.5 The control and the topology of an SEF based on the supercapacitor energy storage

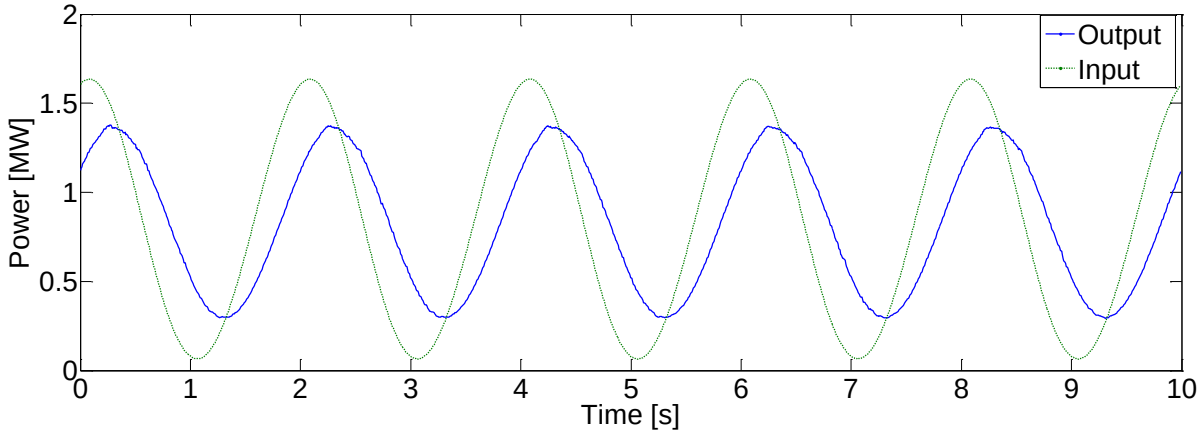

Fig. 5.6 The output and input power of the SEF $f_{in} = f_{cut}$

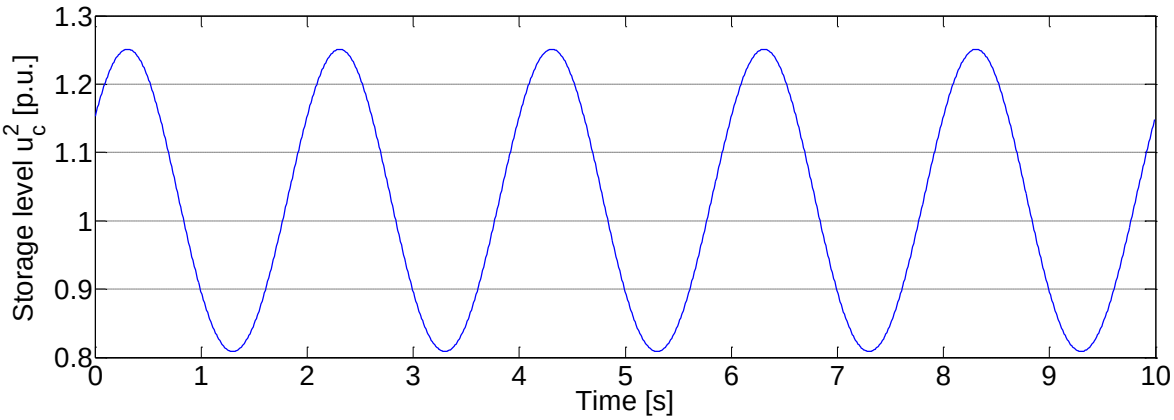

Fig. 5.7 The square of the per-unit capacitor voltage: the storage level of the SEF

5.4.2 First-order PEF Based on the Battery

A PEF is built based on Li-ion battery storage, which is in parallel connected to the power bus with an induction generator as the fluctuating input power. The rated storage capacity E_0 of the battery is 2.16 MWh. A single-frequency fluctuating input power is injected through the parallel induction generator with a period of $\frac{1}{f_{in}} = 7200s$. The cut-off frequency of the energy filter is $f_{cut} = 0.1f_{in}$. Fig. 5.9 shows the fluctuating input and the smoothed output of the PEF.

In comparison with other EES systems, the SoC of a battery cannot be over 1.0, even temporarily. This feature is reflected in Fig. 5.10, which indicates a drawback of the battery-based energy filter that the rated storage capacity must be bigger than that of other light storage.

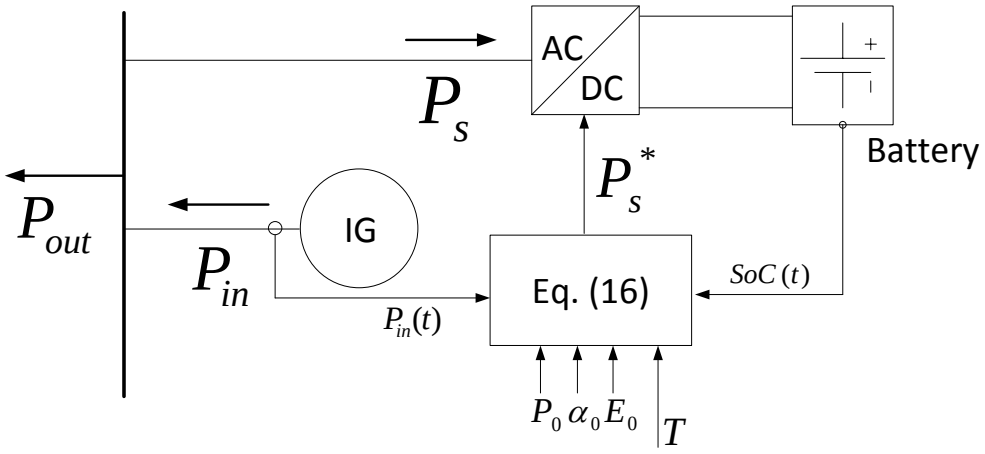

Fig. 5.8 The control and the topology of a PEF based on the battery energy storage

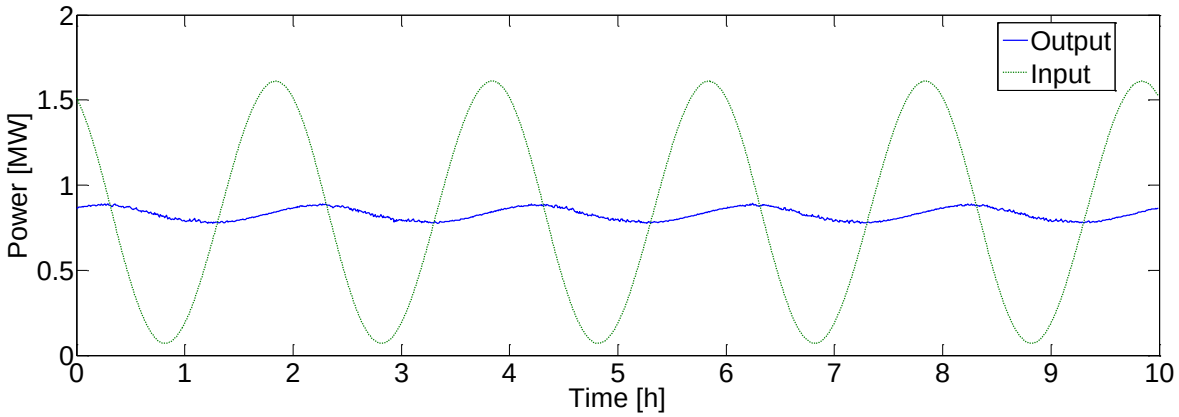

Fig. 5.9 The output and input power of the PEF $f_{in} = 10f_{cut}$

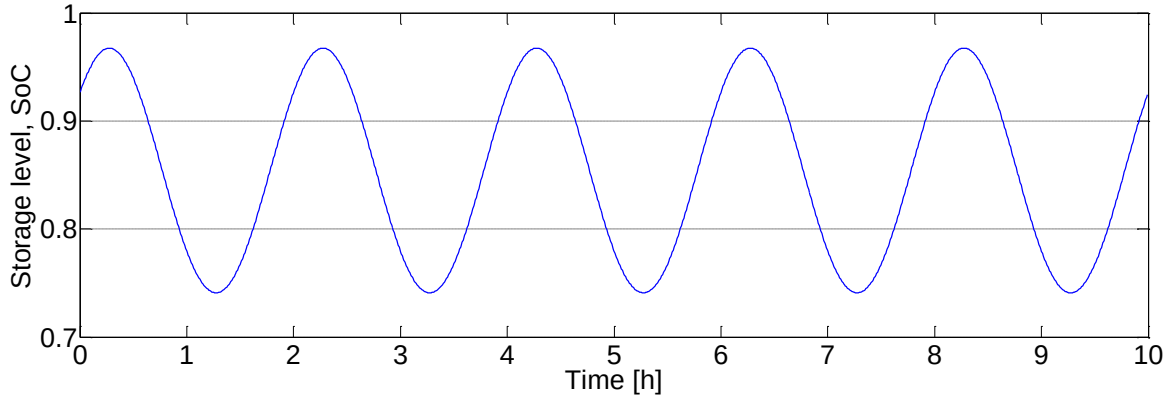

Fig. 5.10 The SoC of the battery: the storage level of the PEF

5.4.3 First and Second-order HEF Based on FES

A HEF is developed based on flywheel energy storage under the first and second-order controls, respectively. The purpose of this simulation is to demonstrate the power smoothing capability of energy filters of different orders. The series pathway is a variable speed induction generator with the rotor flywheel. The parallel pathway is a fixed speed induction generator directly connected to the power bus. Fluctuating power flows lasting 60 seconds are fed through both the pathways and there is a 25% step rise of the power level at $\mathrm{t} = 25\mathrm{s}$. The central frequency of the input power spectrum is 0.2 Hz; E_0 of the rotor flywheel is 1.94 kWh. The cut-off frequency of the HEF is 0.02 Hz.

As can be seen from Fig. 5.12 to 5.14, under both of the controls, the smoothed output power of the energy filter tracks the average level of the total input power, which is not measured and is unknown. Given a step rise of the input power, the storage level rises accordingly. Comparatively, the output power of a second-order energy filter is better smoothed, but its storage level is more sensitive to the average level of the output power. The selection of the order of the energy filter depends on a trade-off between the smoothness of the output power and the sensitivity of the storage level.

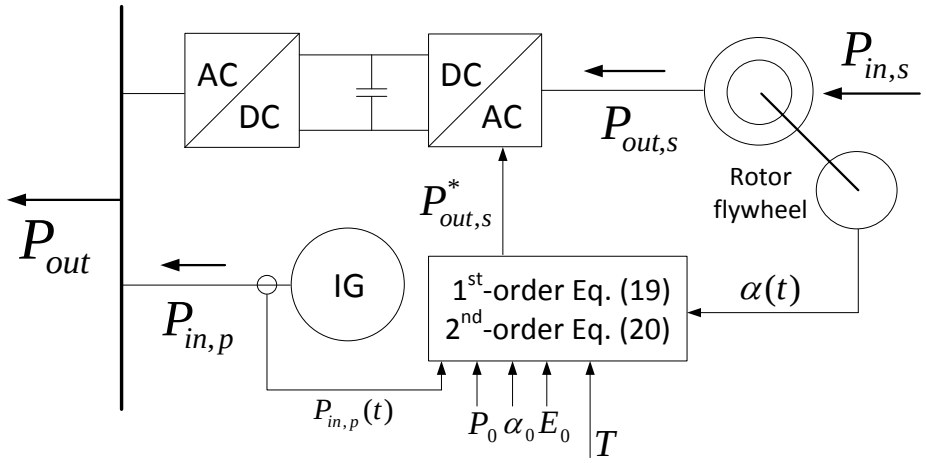

Fig. 5.11 The control and the topology of a HEF based on the rotor flywheel

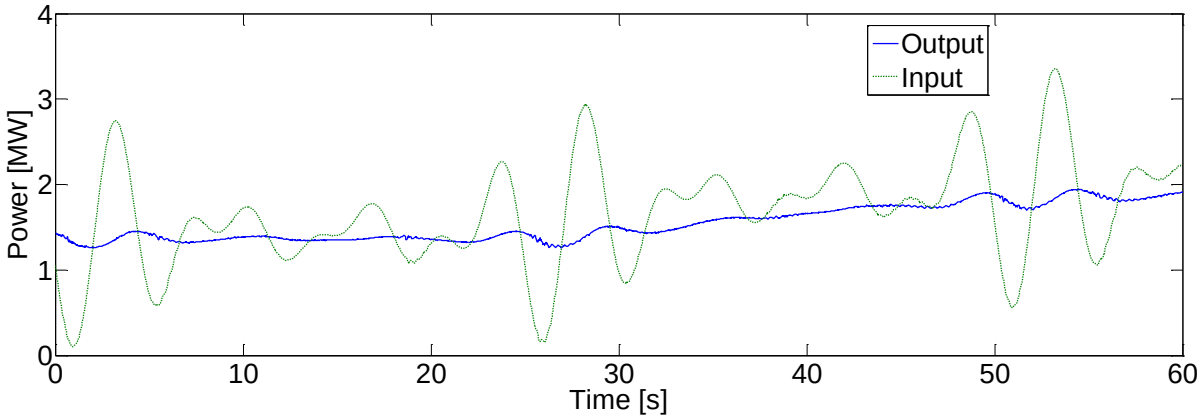

Fig. 5.12 The total output and input power of the first-order HEF

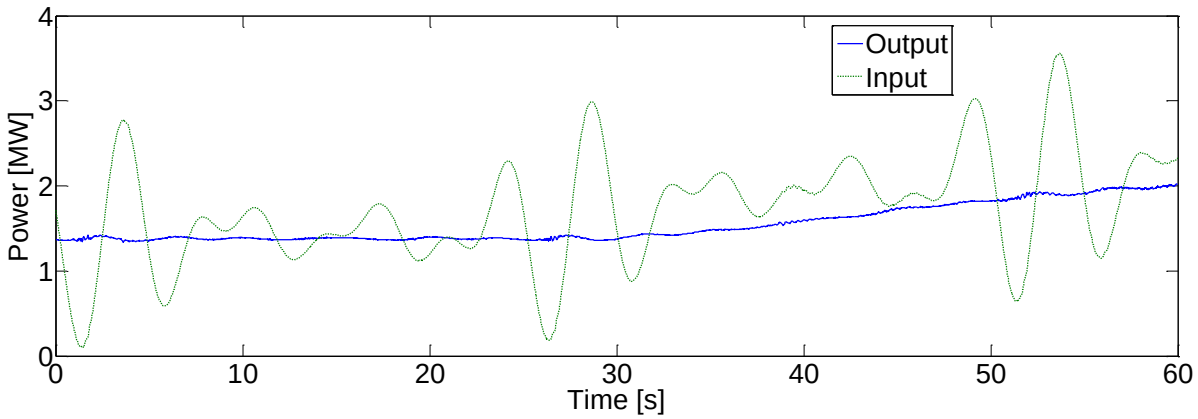

Fig. 5.13 The total output and input power of the second-order HEF

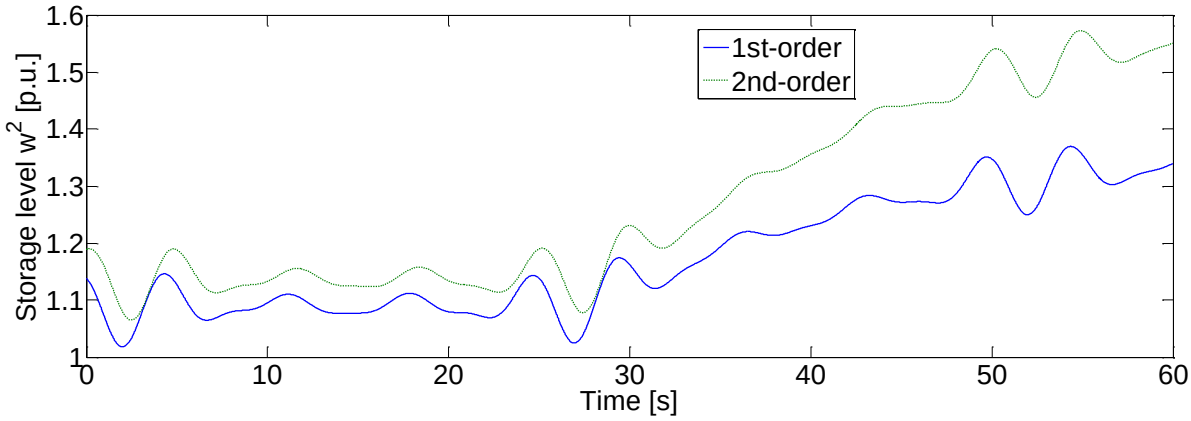

Fig. 5.14 The square of the per-unit flywheel rotor speed: the storage level of the HEF

5.4.4 Frequency Domain Responses of the Energy Filter

The frequency domain responses of both the first and second-order energy filters are shown in Fig. 5.15. The simulation results are obtained from the FES-based HEF under two control methods of different orders. The cut-off frequency is $f_0 = 0.1\,Hz$. For comparison, the theoretical results are pictured based on equations (5.10) and (5.21). In the Bode plots, the simulation results well match the theoretical results. However, in the magnitude responses, the simulation results are a bit smaller when compared to the theoretical lines, due to the storage and conversion losses of the energy filters. The comparative results show that the proposed energy filters work virtually as the low-pass filters of fluctuating input power flows.

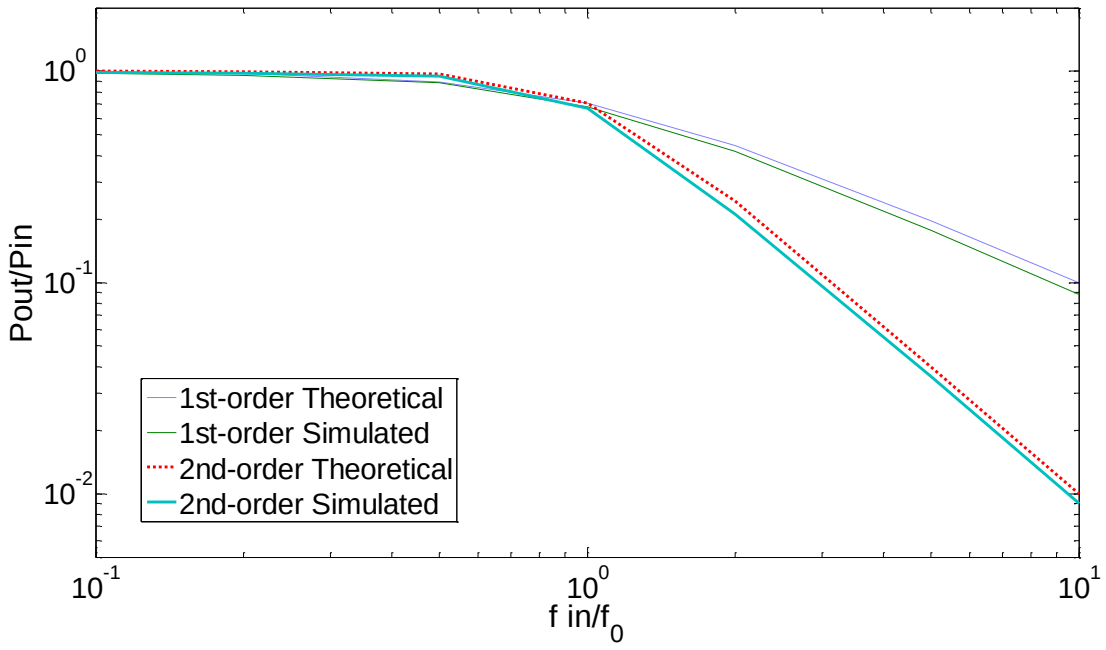

Fig. 5.15 (a) Magnitude responses of the first and second-order HEF

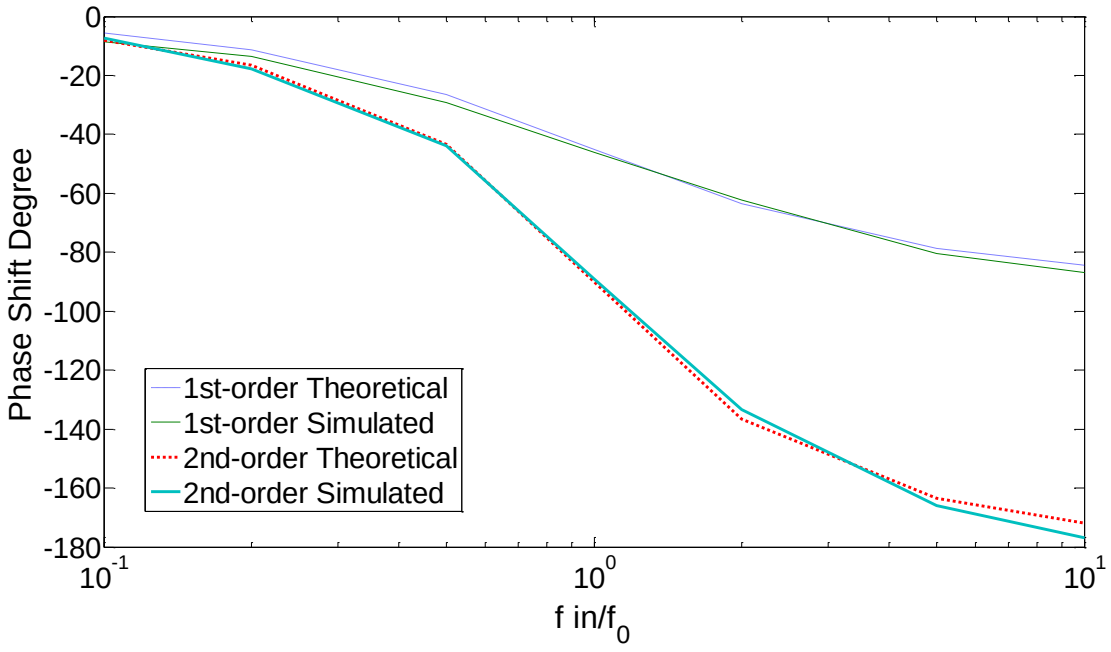

Fig. 5.15 (b) Phase responses of the first and second-order HEF

5.5 Adaptive EF to the Variant Input Power Level

5.5.1 Development of the Adaptive Energy Filter

The control methods of EFs with different topologies and orders presented in section 5.4 cause the EFs to have the input-output relationships which are strictly equivalent to the classical low-pass filters; however, this occurs at a cost. From the above discussions on the storage level sensitivity and the simulation results given in Fig. 5.7, 5.10 and 5.14, an inevitable steady-state bias of the storage level exists and it is proportional to the difference between the actual output power of the EF and the estimated long-term average output power P_0, which is called the output power error. When P_0 is poorly estimated, a big output power error would lead to a large bias of the storage level from its rated value and may stop the whole system from working correctly. From (5.12) and (5.23), it is known that a big inertia of the EF helps to decrease the bias of the storage level. However, in engineering practices the rated storage capacity E_0 cannot be made too large without limitations. To keep the storage level within the acceptable range, not too large or small, P_0 has to be well estimated depending on the real-time input power level.

In this section, a control method of the EF adaptive to the change of P_0 and so the input power level, is developed. The adaptive energy filter (AEF) does not need to estimate P_0 and it promises a zero steady-state bias of the storage level; which means at the steady state, the storage level fluctuates around its rated value no matter how the wave climate changes. Meanwhile, the transient characteristic of the control system is still equivalent to a low-pass filter.

Looking at the first-order SEF for the studied case, the control law of the output power in per-unit values now is

$$P_{out}^{*}(t) = \frac{E_0}{T} e_\alpha(t) + \hat{P}_0 \tag{5.26}$$

$$e_\alpha(t) = \alpha(t) - \alpha_0 \tag{5.27}$$

$e_\alpha(t)$ is the bias of the storage level; and $\hat{P}_0$ is given by the adaptation law; which is

$$\hat{P}_0 = P_r + \frac{1}{T_\alpha} \int e_\alpha(t)\, dt \tag{5.28}$$

where P_r is the installed capacity of the power source, which is a constant helping the starting process of the control system and does not change when the average input power level changes; T_α is a time constant.

By substituting the adaptation law, the adaptive control law of the output power in s-domain is

$$P_{out}^{*}(s) = \left(\frac{E_0}{T} + \frac{1}{sT_\alpha}\right) e_\alpha(s) + \frac{P_r}{s} \tag{5.29}$$

First, we prove that the transient behaviour of the energy filter under this adaptive control is still a low-pass filter. By assuming $P_{out}^{*}(t) = P_{out}(t)$ and referring to (5.7), we have

$$(1 + Ts)P_{out} = P_{in} + \frac{T}{T_\alpha} e_\alpha \tag{5.30}$$

As long as the following condition is fulfilled

$$P_{in} \gg \frac{T}{T_\alpha}|e_\alpha| \tag{5.31}$$

we then have the input-output transfer function exactly the same as (5.10). According to the simulation results in section 5.5.2 and particularly presented in Fig. 5.21, in per-unit values, P_{in} is fluctuating around 1.0, and $|e_\alpha|$ is usually smaller than 0.4.

Second, we study the transient and steady-state bias of the storage level of the AEF. From the adaptive control law (5.29), we have

$$e_\alpha = (P_{out} - P_r) \cdot \frac{s}{\frac{E_0}{T}s + \frac{1}{T_\alpha}} \tag{5.32}$$

So, the initial value and the steady-state value of $e_\alpha(t)$ in time domain with a step input of the power difference are

$$e_\alpha(t=0) = \lim_{s\to\infty} e_\alpha = \frac{T}{E_0}(P_{out} - P_r) \tag{5.33}$$

$$e_\alpha(t\to\infty) = \lim_{s\to 0} e_\alpha = 0 \tag{5.34}$$

and the time constant of the convergence of e_α from its initial value to the steady-state zero is

$$\tau_\alpha = \frac{E_0}{T/T_\alpha} \tag{5.35}$$

From the above, under adaptive control, the transient bias of the storage level is still proportional to the output power error and consequently the storage level sensitivity is $\frac{T}{E_0}$, the same as given in (5.12). However, regardless of the output power error, this transient bias would approach zero with the time constant τ_α.

The above discusses the adaptive SEF. For the energy filters in other topologies, the adaptive control methods can be similarly derived from (5.16) and (5.19) by replacing the estimated P_0 with the adapted $\hat{P}_0$.

Based on Fig. 5.3, the control law of the adaptive PEF is (presented in s-domain)

$$P_S^*(s) = -\left[\left(\frac{E_0}{T} + \frac{1}{sT_\alpha}\right)e_\alpha(s) + \frac{P_r}{s}\right] + P_{in}(s) \tag{5.36}$$

Based on Fig. 5.4, the control law of the adaptive HEF is

$$P_{out,s}^*(s) = \left[\left(\frac{E_0}{T} + \frac{1}{sT_\alpha}\right)e_\alpha(s) + \frac{P_r}{s}\right] - P_{in,p}(s) \tag{5.37}$$

Based on Fig. 5.2, for a second-order adaptive SEF, the control law is

$$P_{out}^*(s) = \left(\frac{1}{Ts+1}\cdot\frac{E_0}{2T} + \frac{1}{sT_\alpha}\right)e_\alpha(s) + \frac{P_r}{s} \tag{5.38}$$

5.5.2 Comparative Case Studies of the AEF

The highlighted advantage of the AEF is that it promises a zero bias of the steady-state storage level, theoretically. In practice, since both the input power level and the real-time input power are changing, the steady state cannot be truly achieved; and the storage level would be swinging around its rated value. Based on the classic EFs discussed in section 5.3, the AEF introduces one more control parameter, the time constant ratio $\frac{T}{T_\alpha}$ with a pair of its contradictive requirements. On one hand, from (5.31), it is desirable that the time constant

ratio is small, so that the term $\frac{T}{T_\alpha}|e_\alpha|$ is ignorable and has no significant impacts on the input-output characteristics of the whole EF system as a low-pass filter and consequently the power smoothing effect. On the other hand, from (5.35), it is desirable that the time constant ratio is large, so τ_α is small and the bias of the storage level converges to zero quickly. To demonstrate the proposed AEF and study the trade-off between the power smoothing effect and the convergence of e_α, four cases of the first-order HEF under different control laws are studied comparatively in this subsection.

The control laws used in these four cases are: 1) the non-adaptive control; 2) the adaptive control with a time constant ratio of 0.1; 3) the adaptive control with a time constant ratio of 1.0; and 4) the adaptive control with a time constant ratio of 10.0. The rated storage capacity E_0 of the rotor flywheel is 1.94 kWh. The cut-off frequency of the energy filter is 0.02 Hz. The sinusoidal mechanical torques are applied to one machine in the series pathway and three machines in the parallel pathway, to emulate the fluctuating input power. Their per-unit magnitudes and frequencies (Hz) are [0.9 0.75 0.88 1.0] and [0.2 0.28 0.24 0.16], respectively. An additional power level, which is in square wave with the magnitude of the rated installed capacity of a single machine 0.35 MW and a low frequency of 0.01 Hz is added to the series channel of the energy filter, to provide a time-varying output power error for testing the adaptiveness of the control methods. More details of the simulation condition are listed in Appendix B.

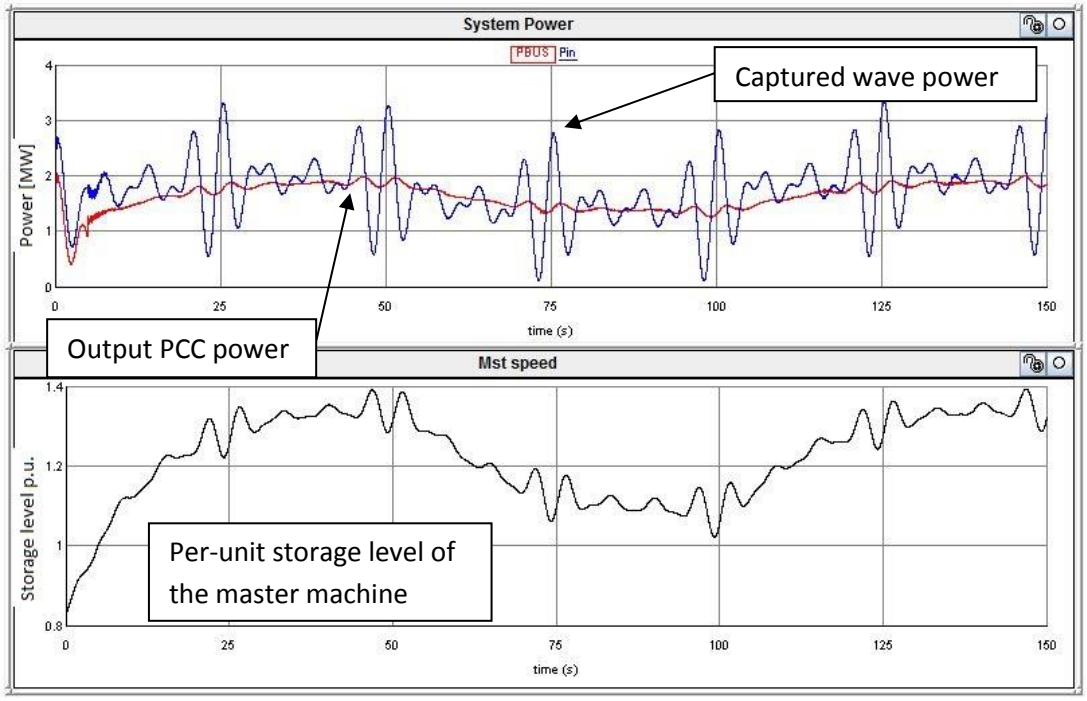

Fig. 5.16 Input-output power and $\alpha(t)$ of the non-adaptive HEF

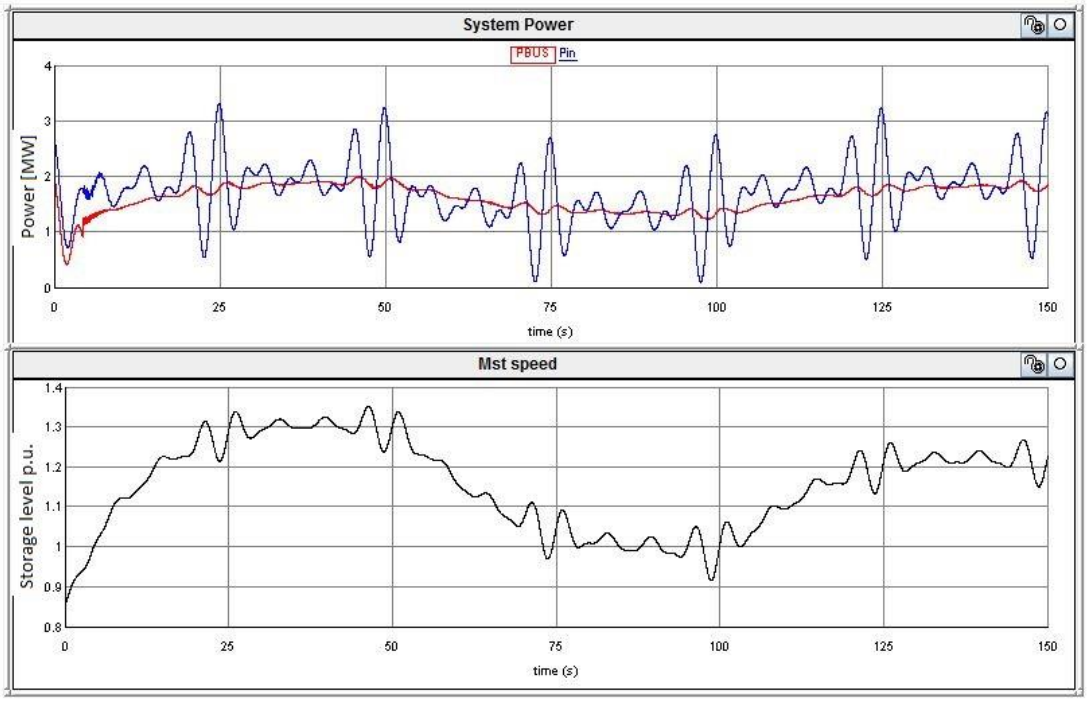

Fig. 5.17 Input-output power and $\alpha(t)$ of the AEF with T/Ta=0.1

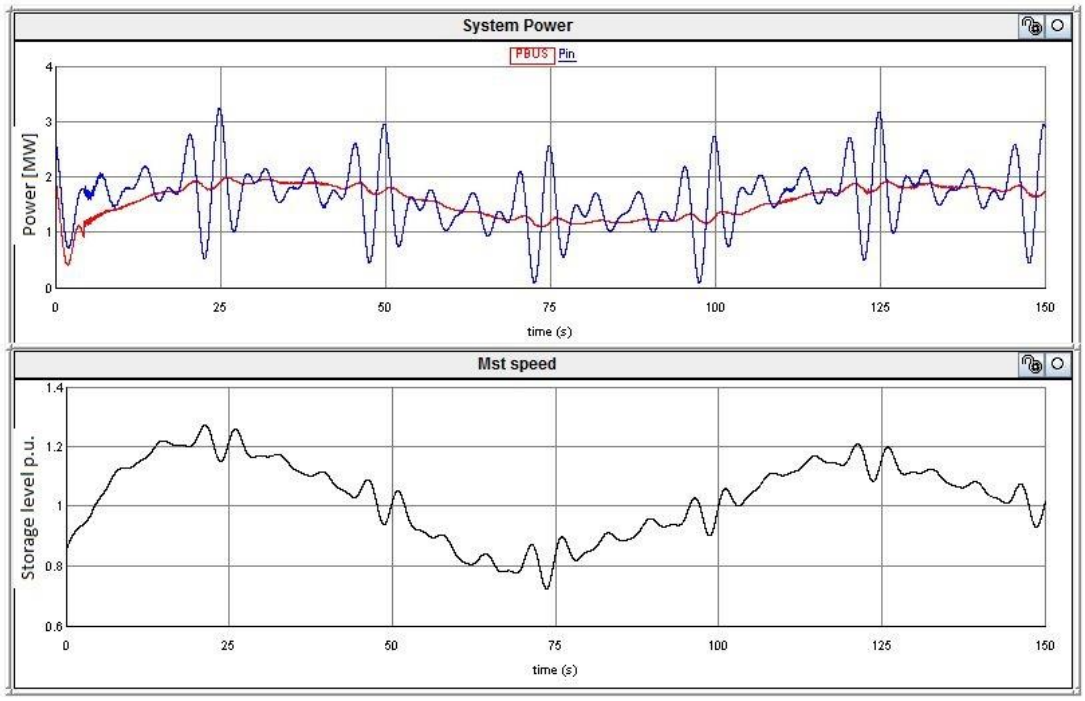

Fig. 5.18 Input-output power and $\alpha(t)$ of the AEF with T/Ta=1.0

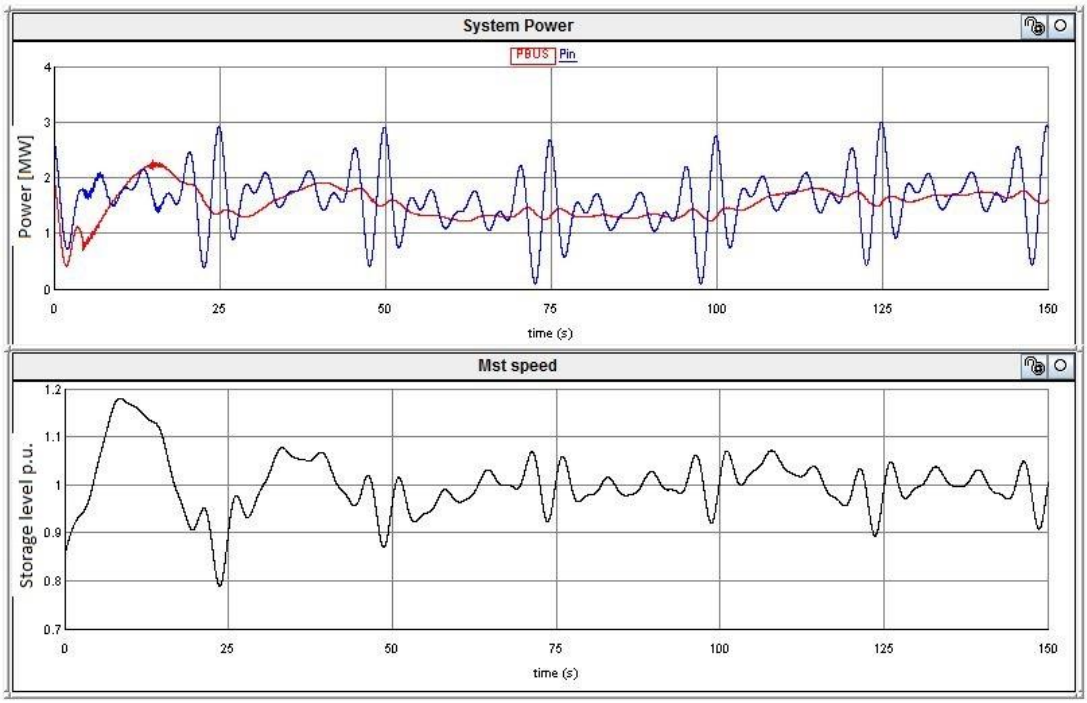

Fig. 5.19 Input-output power and $\alpha(t)$ of the AEF with T/Ta=10.0

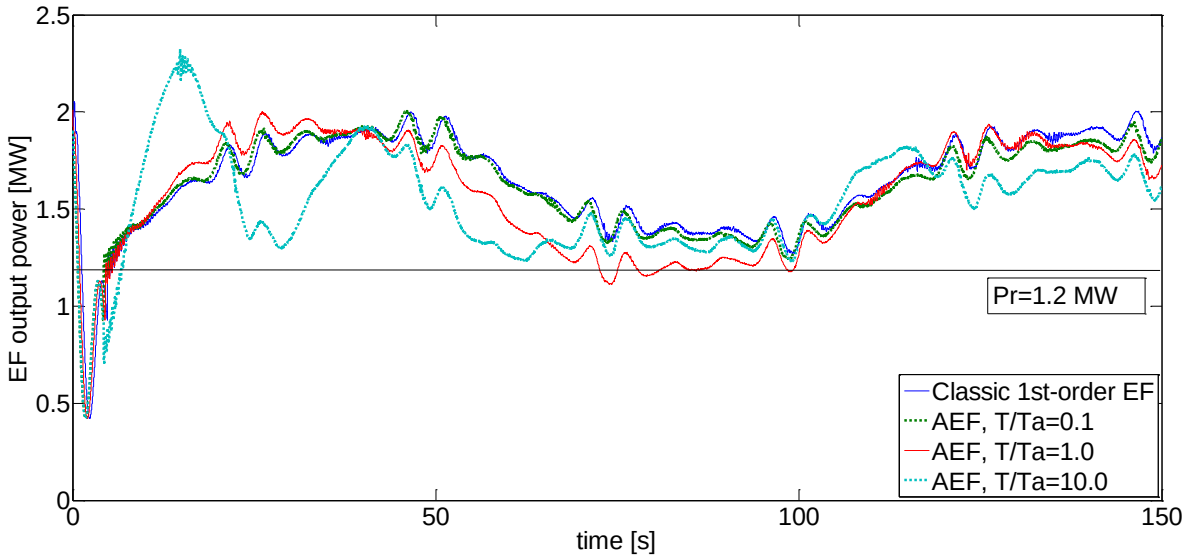

Fig. 5.20 The output power of the four cases in a comparative presentation

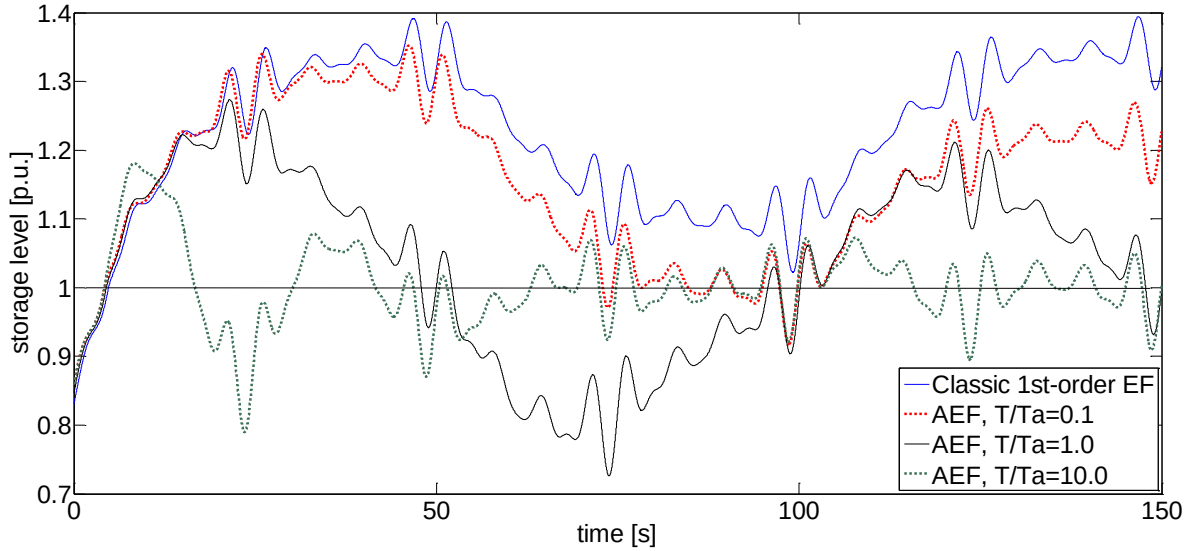

Fig. 5.21 The storage levels of the four cases in a comparative presentation

Fig. 5.16-5.19 show the power smoothing effects of all the four cases. In all these cases, the power flows are very much smoothed by the energy filters. Also, the storage level changes according to the variation of the output power and the control methods. Of particular interest, are the output power characteristics and the storage level bias, which are comparatively presented in Fig. 5.20 and 5.21. Under the non-adaptive control, there is always a storage

level biased from 1.0 per unit, which as can be seen is proportional to the output power error, as expected by the theoretical analysis. Under the adaptive controls and the same output power error condition, the storage level converges to 1.0 per unit. From Fig. 5.21, the AEF control with a larger time constant ratio makes the average of the storage level bias converge to 1.0 p.u. more quickly, but the output power is less smoothed. Especially in the case of *T/Ta*=10.0, from Fig. 5.20 it is seen that the output power is not so smoothed compared with that of other cases; especially at the beginning when there is a large gap between the output power and the average input power level, even though the storage level under this big time constant ratio converges to 1.0 very quickly. In this case study, the AEF control with *T/Ta*=1.0 seems like a good trade-off among the four cases, for it makes the storage level converge to 1.0 in a moderate speed and at a small cost of the output power characteristics.

5.6 Design of Energy Filters in Real Applications

Based on the above knowledge of EFs, this section concerns how to determine the topology and the control parameters in designing an EF in real applications.

5.6.1 Selection of the Topology

The selection of the topology of an energy filter is a trade-off of costs between the power conversion capacity and the power flow measurement.

The SEF is a desirable topology as it does not need to measure the input power. However, it needs a full-rated power converter to let all the smoothed output power go through it. It could be done at a small cost when the inherent inertia of energy conversion devices is enlarged and used as the EES. For example, the DC capacitor of a full-rated converter and the rotor inertia of a variable speed generator could be used as the inherent EES. There is no high extra cost

raised since the energy conversion device was part of the system. An extra cost would be raised when the energy conversion device was not part of the system.

The input power must be measured in the PEF. The advantage is that the EES and the power converter do not transmit the full-rated input power, but the compensating power instead to the power bus, so both of them could be scaled down. Particularly the PEF under the single-measurement control is not desirable, as it cannot regulate the storage level. However, as discussed in section 5.3.3, it is useful to build a PEF with no EES and the compensating power is fed by a power source. In Fig. 5.22, the converter at the weak grid side is under the PEF's control to filter out the input power fluctuations from the IG when the compensating power is fed by the strong grid.

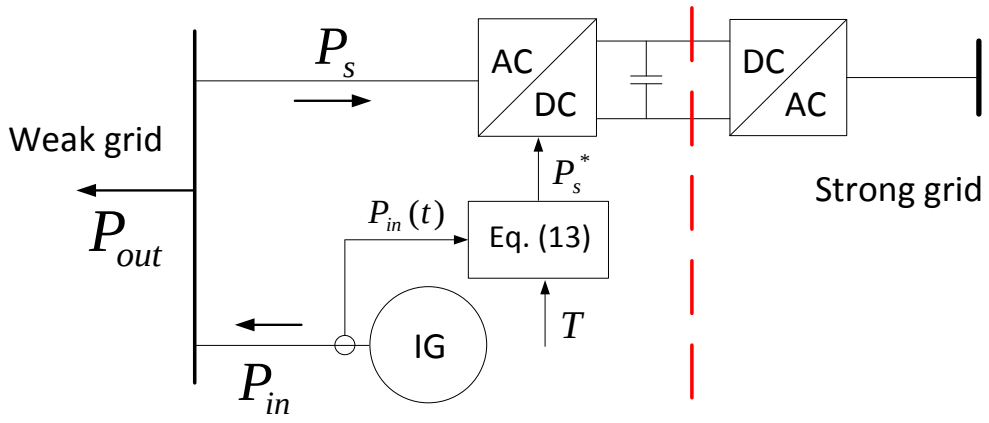

Fig. 5.22 A PEF under single-measurement control with no EES

The HEF takes the advantages of both the SEF and PEF. In a HEF the total input power is separated into two flows going through the series and the parallel pathway. The power flow through the series pathway does not need to be measured and the flow through the parallel

pathway does not go through the converter. This leaves a good flexibility for the construction of energy filters in real applications.

5.6.2 Control Parameters' Determination

The control parameters are determined based on the input power characteristics and the accepted range of the storage level, for its protection.

An energy filter control is determined by four parameters: T, α_0, P_0 and E_0. The first three of them could be independently selected and changed. The rated storage capacity E_0 is fixed once the EES is built.

The cut-off frequency and the transfer function of the energy filter are determined by the time constant T. With a given T, E_0 is selected solely based on the accepted range of the storage level sensitivity from (5.12) and (5.23). In order to regulate the storage level sensitivity within the safe range, a larger E_0 is required when input power fluctuation is slower and larger.

The rated storage level α_0 should usually be 1.0 to make a full use of the energy storage capacity. When the EES is a battery, however, α_0 should be smaller than 1.0 since the SoC of batteries cannot be over 1.0.

Summary

This chapter presents the development and analysis of energy filters. The filter is a conventional tool in signal processing and power quality management. In this study, the concept of a filter is used in power flow control and energy quality improvement. The

proposed energy filters can filter and track fluctuating and unmeasurable power flows as useful tools for renewable power integration. In nature, energy filters are control systems of light EES systems. The series, parallel and hybrid energy filters (SEF, PEF and HEF) are discussed and demonstrated via RTDS simulations, respectively. The topology, control and EES device are three key factors to be considered in designing an energy filter.

CHAPTER 6 OPERATION AND CONTROL OF A MASTER-SLAVE WAVE FARM SYSTEM

Abstract- Many studies on wave energy conversion (WEC) have already been conducted on the maximum power take-off (PTO) techniques of a single machine. However, there is a lack of research publications on the power quality and energy quality of a wave farm. Due to the pulsating nature of the ocean wave and the characteristics of the popular PTO devices, usually the generated electric power has severe fluctuations and poor power quality. This raises problems with the grid integration and thus existing solutions require extra energy storage systems and over-rated power electronic devices. In this chapter, a wave farm system in a master-slave electrical structure with rotor inertia energy storage is proposed; which can provide self-smoothed power output and needs a reduced number of power converters. Two control methods, namely, the moving average filter (MAF) method and the energy filter (EF) control method, are proposed for the smoothing control of wave farm output power. The two control methods are comparatively demonstrated on the proposed system. Simulations on RTDS show that the proposed master-slave wave farm structure and the two control methods are able to produce a smoothed electric power to the grid with good energy quality and efficiency under a heavily fluctuating raw wave power.

6.1 Introduction

In comparison with solar and wind, wave is the most fluctuating renewable energy with power fluctuations of large magnitudes and short periods. For this reason, a wave farm

system is selected for the application of the energy filter control proposed in Chapter 5.

In order to achieve good grid-side power and energy quality from a wave farm in a cost-effective way, at its electrical sector it would be necessary to: 1) reduce the number of power converters; and 2) provide a solution of long-life, compact and electrically controlled energy buffers without over-rated devices. In this chapter, a master-slave wave farm system and its control methods are proposed against these challenges with the following advantages: 1) the proposed system is able to deliver smoothed real power and controllable reactive power to the grid. 2) No over-rated devices or extra electrical energy storage (EES) is required since the rotor inertia is used as energy storage before the back-to-back converters. 3) The proposed system has a reduced number of converters as long as the PTOs are built based on rotating machines. 4) The EF control proposed in Chapter 5 is applied to the wave farm system, which can achieve a quantitative power smoothing effect and avoid mechanical measurements on the electric machines.

In this study, it is assumed that the captured wave power has no correlation with the rotor speed of electric machines but depends only on the mechanical dynamics. It is reasonable when hydraulic modules are used in PTO to largely decouple the interactions between the mechanical and electrical side. [53] Hydraulic-based PTOs are commonly seen in hinged contour devices and in some point absorbers using rotating machines. In cases like the OWC however, the efficiency of capturing the wave energy is very much related to the rotor speed; as it is similar to a wind turbine generator in nature and the rotor speed should follow the MPPT control to maximize the capture of the power. In paper [108] it is demonstrated that the loss of power capture efficiency of a MPPT controlled DFIG system could be very small (<1%) when the rotor speed oscillates around the optimum point of moderate magnitudes. As

yet, this assumption is unproved in cases like the OWC when the average rotor speed is away from the rated value. This part is discussed in 6.4.2.

6.2 The Master-slave Structure

This section starts with the proposed system consisting of 2 masters and 3 slaves (referred to as "2M3S system") as shown in Fig. 6.1. Slaves are induction machines directly connected to the power bus. Masters are PMSMs connected to the power bus via full rated converters with controllable power outputs. Power outputs from all the masters and slaves are collected at the point of common coupling (PCC) as a smoothed summation by appropriate control of the masters and then transmitted to the onshore grid, via the undersea cable HVAC or HVDC, depending on the distance to the coast and the power capacity of the system. [102]

6.2.1 Slaves

The slaves are a group of wave power generation units directly connected to the PCC without energy buffers. They are expected to produce a fluctuating real power and possibly consume a variable reactive power depending on their PTO. All the mainstream PTOs mentioned in section 6.1 are applicable, though they could be further simplified since no energy buffer is required. For example, the mechanical control of the manifolds of Pelamis [103] and other similar hydraulic PTOs can be removed. For a point absorber, power converters are no longer necessary if they are used for fast energy storage and/or reactive power compensation. However, converters are still necessary if they control the electric machine to maximize the power take-off efficiency (e.g. OWC) or phase-order alteration (e.g. PTO with linear machines). The proposed system is compatible with all the mainstream PTOs, but friendlier

to hydraulic PTOs and directly connected induction generators (e.g. induction generators in the overtopping devices).

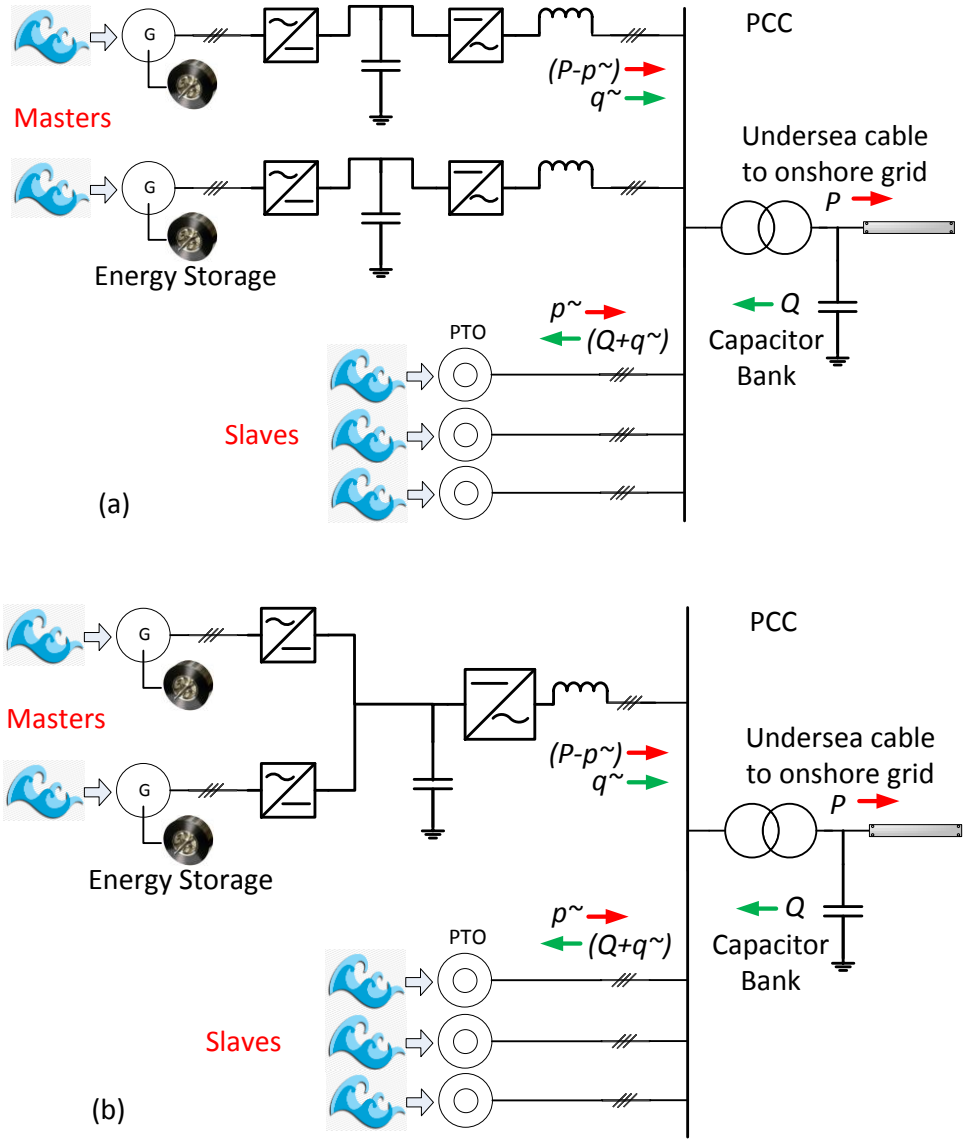

Fig. 6.1 An overview of the master-slave wave farm system of: (a) each master with converters; and (b) multiple masters with a common DC link. The *PQ* are the constant parts of the real and reactive power, respectively; *p*~ and *q*~ are the time-varying components.

6.2.2 Masters

Masters are wave power generators which deliver controlled power to the PCC. The difference between the power delivered to the PCC and the wave power captured is balanced by the energy buffer, which is in this study implemented by the rotor inertias of the masters. As discussed later, flywheels could be added on rotors (rotor flywheels) to increase the energy storage capacity, depending on how large the master inertia is itself and the capacity ratio between the masters and slaves. Compared to other energy buffer solutions, the energy buffers using rotor inertias of the masters have the following advantages: 1) long life of energy recharge cycle. By contrast, considering the period of wave energy recharge is short (5-12s), a battery with the same storage capacity could be worn out in days (even hours); 2) high energy density and compact design; and 3) the power is smoothed from the stator of the machines, thus no device needs to be over-rated. The power from the masters could be transmitted to the PCC through either independent converters or a common DC link. In both cases, the power flow is controlled by the machine side rectifiers and the DC voltage is maintained by the grid side inverter(s).

The proposed master-slave system has the following two features: 1) firstly, the master is only compatible with rotating machines; 2) secondly, for some PTOs like the OWC, there are requirements on the rotor speed of the machines for the maximum PTO efficiency, which may lead to conflicting with the requirements of the energy storage. However, this can be solved by setting the rated speed at an optimal point and the real-time speed oscillates around this point at a small cost of efficiency loss. It has been demonstrated in papers [104] and [105].

6.2.3 Operations and Engineering Feasibility

The total power output is smoothed by controlling the energy buffers of the masters. Slaves deliver all the wave power they harvest to the PCC; while masters only deliver controlled power, to keep the total power output tracking a smoothed reference given by the wave farm control. In the case where slaves consume variable reactive power *Q* due to the periodic wave drive, the master power converters are in charge of the dynamic *Q* compensation, while the capacitor bank on the PCC covers the fixed major part of the reactive power. Compared with previous studies in which every PTO device requires a power converter, the proposed system allows a few of the master converters to improve the power quality of the whole system with a vast number of slaves. It reduces the total installation and maintenance cost.

The engineering feasibility of the rotor flywheel is demonstrated as below. The rotor inertia must be large enough to hold the temporally stored energy within a reasonable range of speed variation; meanwhile, it must also be small enough to be feasible and cost effective. For the given maximum, minimum and rated mechanical speed of master rotors ω_{max}, ω_{min}, ω_{rat} and the required energy storage capacity E_0, the rotor inertia *I* must be larger than

$$I > \max\left\{\frac{2E_0}{(\omega_{max}^2 - \omega_{rat}^2)}, \frac{2E_0}{(\omega_{rat}^2 - \omega_{min}^2)}\right\} \tag{6.1}$$

The required inertia of a PTO is usually small enough in engineering practice that it can be provided by the rotor with a coupled flywheel of a reasonable size. In this study, each wave power generator is rated at 350 kW, which is about the same order as that in the existing projects introduced in Chapter 2. For example, the stability of a 2.8 MW, 2M6S (with 2 masters and 6 slaves) system with master rotor inertias of 300 kg/m^2 is demonstrated in this

study. For comparison, the rotor inertia of a 350-kW generator is 86.6 kg/m^2 [106]; thus only an extra rotor flywheel with an inertia of 213.4kg/m^2 is needed. For a cylinder shape flywheel, its inertia can be derived as

$$I_{flywheel} = \frac{1}{2}\pi\rho h R^4 \tag{6.2}$$

where ρ is the material density; h the thickness; and R the radius. Obviously the inertia can be made big enough effectively by enlarging the radius. In this case a solid steel ($\rho = 8.0\ g/cm^3$) flywheel with $h = 0.5\ m$ and $R = 0.43\ m$ is required, which is a feasible size to be installed in most of the existing WECs.

Based on this topology, a bigger wave farm with a higher installed capacity can be achieved by increasing the masters and slaves proportionally.

6.3 Converter and System Layer Control

The objective of the converter's control and that of the system's control in a wave farm system are different. The former is to make the voltage, current and power provided by the converters track the given references; while the latter is to determine these references at a system level. In this section, firstly, a discussion is presented on two different reactive power controls of the converters, based on the state-of-the-art *dq* decoupling control method. [104] Then, the two system control methods are presented.

6.3.1 Converter Control: unity power factor versus constant PCC voltage

The converter's control can be separated into four items depending on which side and which axis it is on. They are:

- ***Grid side d-axis control:*** this is to balance the input and output power of the back-to-back converter by stabilizing the DC link voltage.
- ***Grid side q-axis control:*** this is to control the grid side reactive power according to the local voltage or power factor requirement.
- ***PTO side q-axis control:*** this is to control the electric torque and consequently the power from/to the machine.
- ***PTO side d-axis control:*** this is to control the excitation mode of the machine. In this paper, the PM machines are used and the minimum current mode is selected by referring the d-axis current to zero.

At the grid side, the q-axis controls the reactive power *Q* and usually there are two strategies. One strategy keeps a constant power factor, which in a popular case is unity. With this strategy, however, the wave farm is not able to stabilize the PCC voltage when the real power changes. The other strategy keeps the PCC voltage constant, which as yet requires a larger converter capacity.

In this study, the unity power factor control is adopted. Generally, when a relatively small-scale power source is connected to a PCC with other units, it is asked to give a constant power factor and the PCC voltage is regulated by other devices such as a STATCOM or large-scale synchronous generators. For example, when a wave farm is integrated with an offshore wind farm, it is the wind farm that supports the PCC voltage according to the UK grid code. [107]

6.3.2 System Control #1: moving average filter

The system controller's job is to generate an appropriate reference for the total power output of the wave farm, which would be allocated to master converters as their inputs.

The key question is how to ensure this reference tracks the average of the total harvested wave power, otherwise, the average storage level will keep going up or down until the system is disconnected from the grid. The wave farm should in the long term deliver the average of the power which it absorbs from the wave P_{avg} to the grid and leave the power fluctuation in the buffers. A natural idea is to use the MAF, which is a data processor calculating the average of a sampled time series within a fixed-length moving window as has been described in [104]. The MAF process is determined by two parameters: the sampling frequency, and the length of the moving window.

Accordingly, this method needs to measure the total harvested wave power at the primary side of the wave farm. For slaves, this can be done by measuring the generated electric power instead with a reasonable assumption that it is the same as the mechanical power from the wave. It is desirable because the electric power measurement is much easier and cheaper than the mechanical power. However, for the masters, the mechanical power measurement at the primary side is inevitable, which is a severe drawback of this method.

Since the slaves generate fluctuating power P_{slv}, the masters are controlled to generate the difference $P_{mst} = P_{avg} - P_{slv}$, which is dynamically allocated among all the masters. The allocation follows the principle that those masters with a higher storage level take more shares, which mathematically is

$$P_{mst,i} = \frac{\omega_i^2}{\sum_{i=1}^{M} \omega_i^2} \cdot P_{mst} \tag{6.3}$$

where $P_{mst,i}$ is the real power reference for i^{th} master; ω_i the rotor speed of i^{th} master; and M is the total number of masters.

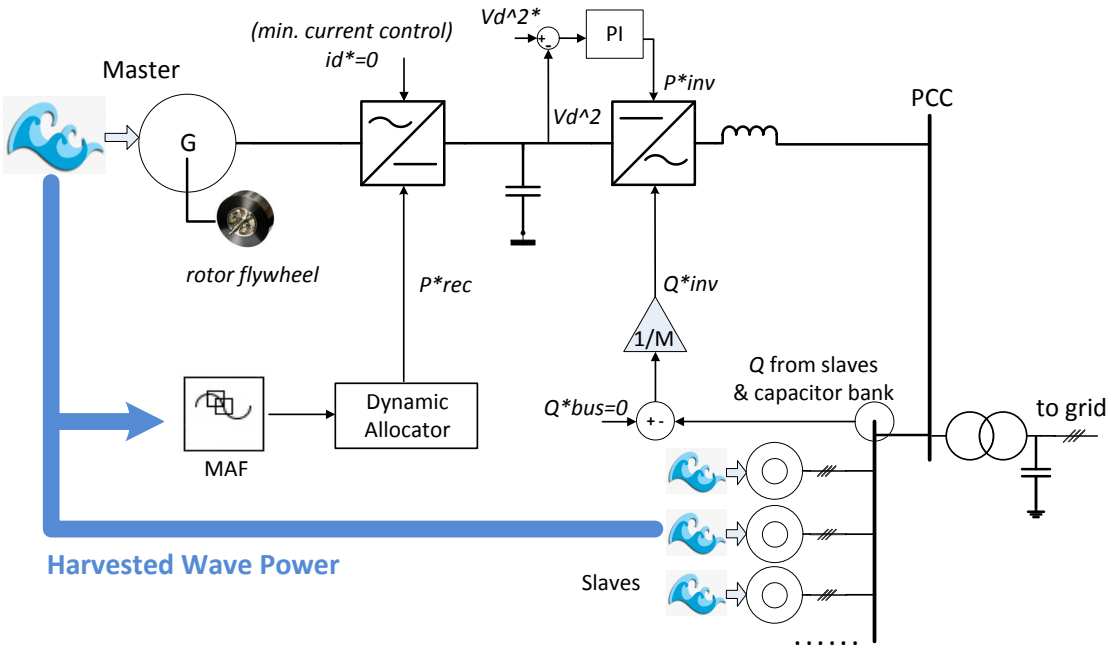

Fig. 6.2 System control based on the MAF

6.3.3 System Control #2: energy filter control

The MAF method suffers the drawback of having to measure the mechanical power on every master machine, which is difficult to be implemented in an offshore environment. To avoid this disadvantage, this subsection applies the hybrid EF as proposed in Chapter 5, to the wave farm system.

Fig. 6.3 shows the power flow through the proposed master-slave system in a per-unit value. The P_{in} is the total harvested wave power; P_{bus} is the total output power; $H\frac{d}{dt}\sum\omega_i^2$ represents the rotating kinetic power stored by the master rotors, where H is the inertia constant of master rotors.

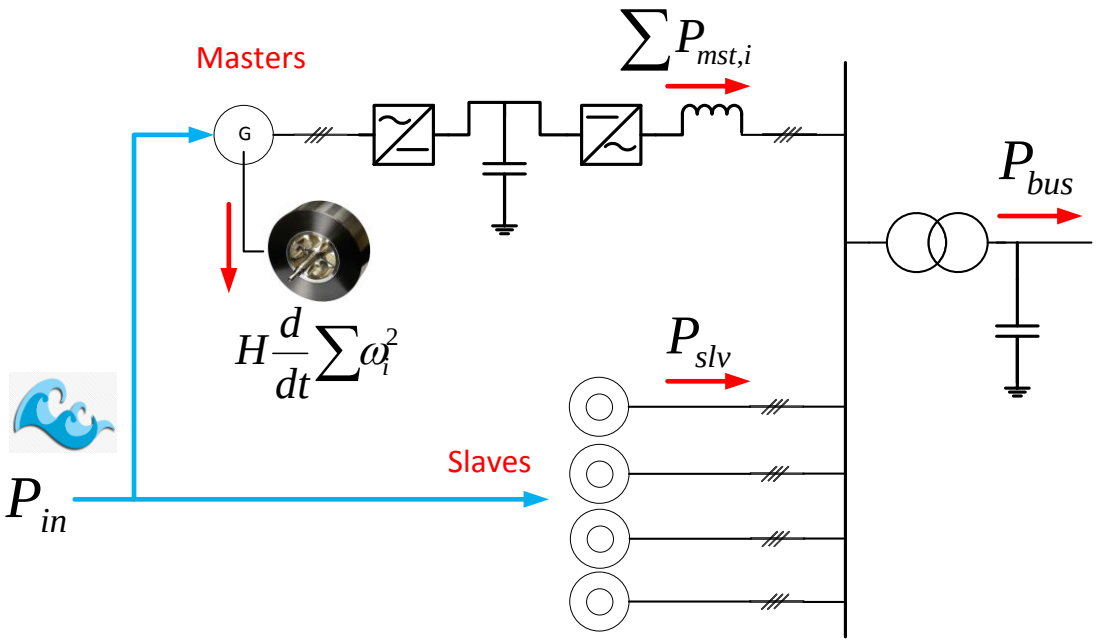

Fig. 6.3 Power flow through the proposed master-slave system

By ignoring the power loss, we have

$$P_{in} = H\frac{d}{dt}\sum \omega_i^2 + P_{bus} \tag{6.4}$$

For the system level control, it is reasonable to assume an immediate tracking of the power reference which could be promised by the converter control. With this assumption, we define the total power output P_{bus} is controlled as (in per unit)

$$P_{bus} = P_{bus}^{ref} = \frac{H}{T}\sum(\omega_i^2 - \omega_0^2) + P_0 \tag{6.5}$$

where T is the time constant; ω_0 and P_0 the rated master rotor speed and rated total power output, respectively. With this, (6.4) can be re-written as

$$P_{in} = T\frac{d}{dt}P_{bus} + P_{bus} \tag{6.6}$$

or in the s-domain as

$$\frac{P_{bus}}{P_{in}} = \frac{1}{Ts+1} \tag{6.7}$$

It has a form of a first-order lowpass filter (LPF). Thus, the proposed system behaves like an LPF of the power flow. It smoothies the power output with a controllable time constant T. The control function of the total power output given by (6.5) is in the form of a rising straight line through the rated operating point $(\sum \omega_0^2, P_0)$ with a slope of H/T, as shown in Fig. 6.4.

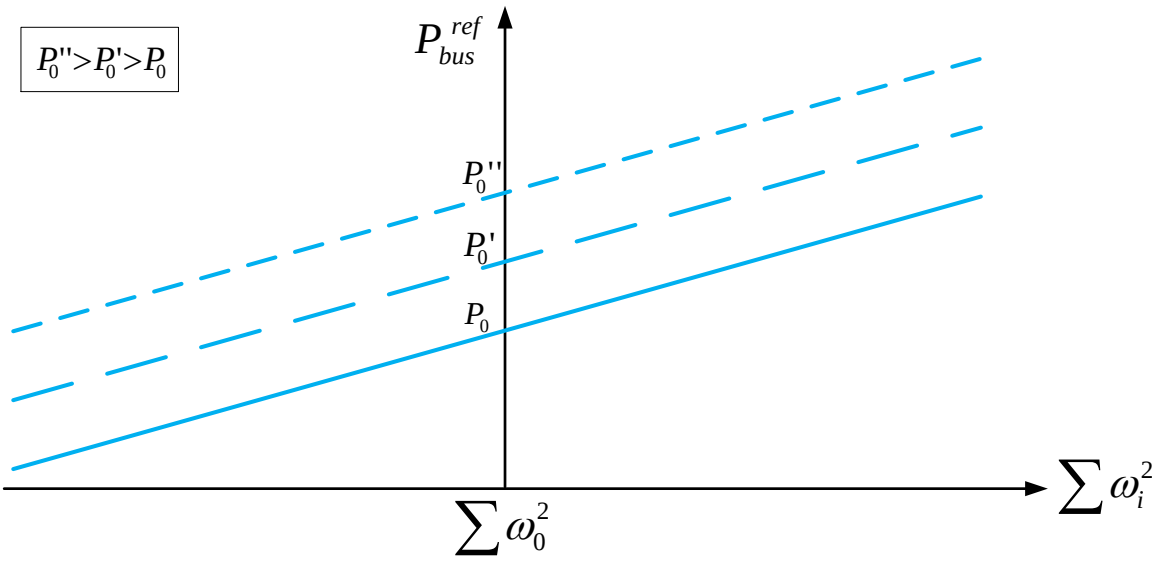

Fig. 6.4 The EF control characteristics with different rated total power output P_0, which is determined according to the local wave climate profile on a sea-state-to-sea-state basis

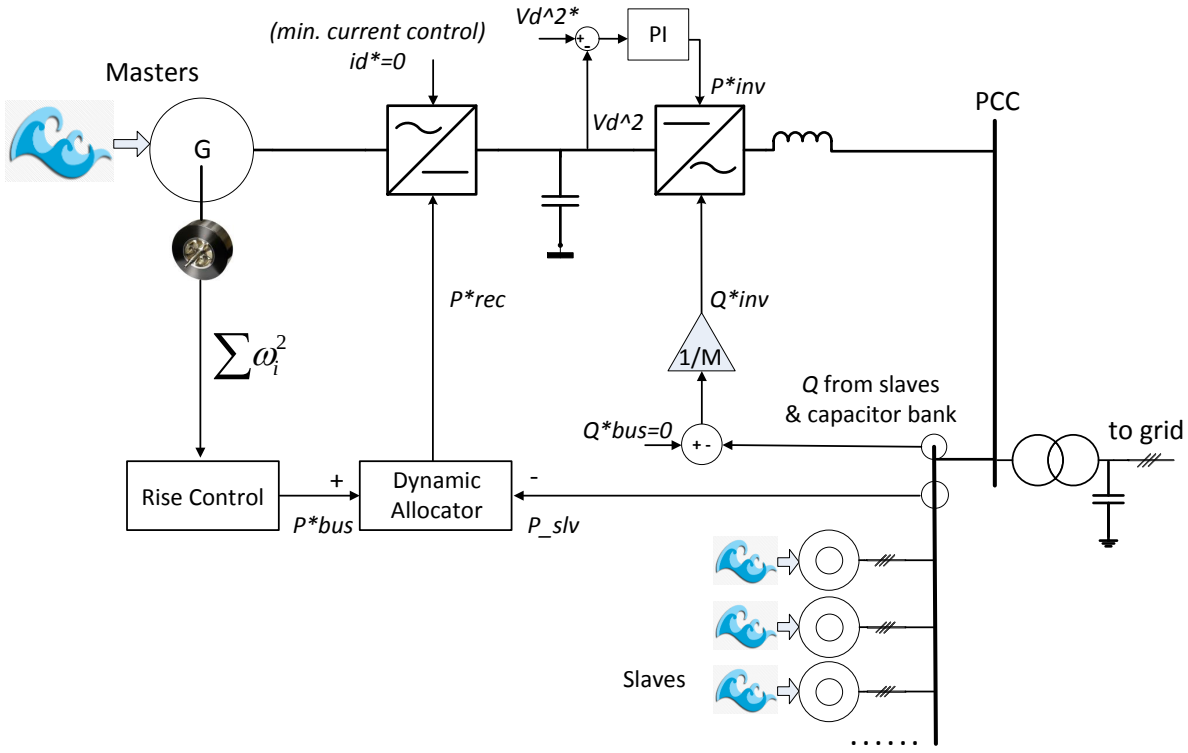

Fig. 6.5 System control diagram based on the EF control method

Equation (6.5) defines the control law of the total power output of the system, which is allocated to all masters as

$$P_{mst,i} = \frac{\omega_i^2}{\sum_{i=1}^{M} \omega_i^2} \cdot (P_{bus}^{ref} - P_{slv}) \tag{6.8}$$

The complete control system is shown in Fig. 6.5.

By contrast with the MAF method, the EF control method enjoys the advantage that it does not need to measure the mechanical power, but only needs to measure the master rotor speeds and the electrical power outputs of the slaves, both of which can be easily obtained.

6.3.4 Further Discussions on the EF Control

Equations (6.5) and (6.8) together determine the power control of each master. As can be seen, with the measured rotor speed and inertia, the system performances under this control law are dependent on two control parameters: the time constant T and the rated total output power P_0.

The P_0 is a constant obtained according to the local wave power profile. This could also be a piece-wise constant changing on a sea-state-to-sea-state basis.

The selection of T is a trade-off between the power smoothing effect and the sensitivity of the rotor speed. From (6.5), the sensitivity of the rotor speed is defined as

$$\frac{d\sum \omega_i^2}{dP_{bus}} = \frac{T}{H} \tag{6.9}$$

This describes how much the master rotor speeds would leave from their rated values when the total power output of the wave farm changes. Accordingly, T must be large enough to achieve a good power smoothing effect, yet small enough to avoid a too large sensitivity of the rotor speed. Large rotor inertia is also helpful to suppress the sensitivity.

6.4 Case Studies

A wave farm system with 2 masters and 6 slaves (2M6S) based on independent converters was built and simulated on RTDS. The model consists of wave generators, master converters, a transformer, the capacitor bank, undersea cable and the local grid, in the structure as illustrated in Fig. 6.1. The cable model is an equivalent Π circuit and the parameters refer to the real project Wave Hub in the UK. [53] The local grid is modelled as an infinite voltage

source with a short-circuit ratio (SCR) of 10.0. A group of sinusoidal mechanical torques with different frequencies and magnitudes are applied to the generators to model the interactions between the devices and the wave under regular and strong wave conditions. The frequencies are selected within a typical range of the wave period. Detailed simulation parameters are given in Appendix C.

The simulation cases are arranged as follows. Firstly, the system operations under the MAF and EF control methods are compared. The 300 s real-time simulation results presented in Fig. 6-8 consist of three sections: (1) the starting process; (2) the operations under the rated input wave power (regular wave); and (3) the operations under the increased input wave power with the same control parameters (strong wave). Secondly, a quantitative analysis on the selection of time constant T is presented. Finally, results of fault conditions are presented.

6.4.1 The MAF Method

In this case, the system operations under the MAF control are presented. The sampling frequency and the length of the moving window of the MAF process are 10 Hz and 12 s, respectively. The length of the moving window is selected as it is comparable to a typical wave period.

Fig. 6.6(a) shows the input wave power and the total output electric power of the wave farm system in 300 s. As can be seen, the total output power is smoothed when the input wave power fluctuates and the grid side reactive power is controlled at zero. After 150 s when the input wave power increases, it is seen that the system output power is able to track the average of the input power.

Fig. 6.7(a) presents the per-unit rotor speed of one master machine in the system, which timely varies to store and release the energy. The rotor flywheels of the master machines work as the energy buffers of the wave farm system.

Fig. 6.8(a) shows the real and reactive power on the grid side inverter of this master machine, which is timely changing to compensate for the fluctuating power from the slaves. In particular, its real power could become negative when the master machine is operated as a motor to absorb the peak power from the slaves. The average Q approaches zero since the capacitor bank is dimensioned to minimize the apparent power of the inverter.

6.4.2 The Energy Filter Control

The energy filter control is demonstrated with the same operating conditions. The system operations are presented in Fig. 6.6(b), 6.7(b) and 6.8(b) in comparison with those of the MAF. The time constant T is 12 s, the same as the length of the moving window in the MAF method.

As can be seen from the figures, the capabilities of power smoothing and zero reactive power maintenance of the energy filter are demonstrated. Conclusively, this method has similar control characteristics to the MAF method, while it avoids the mechanical power measurements on the master machines.

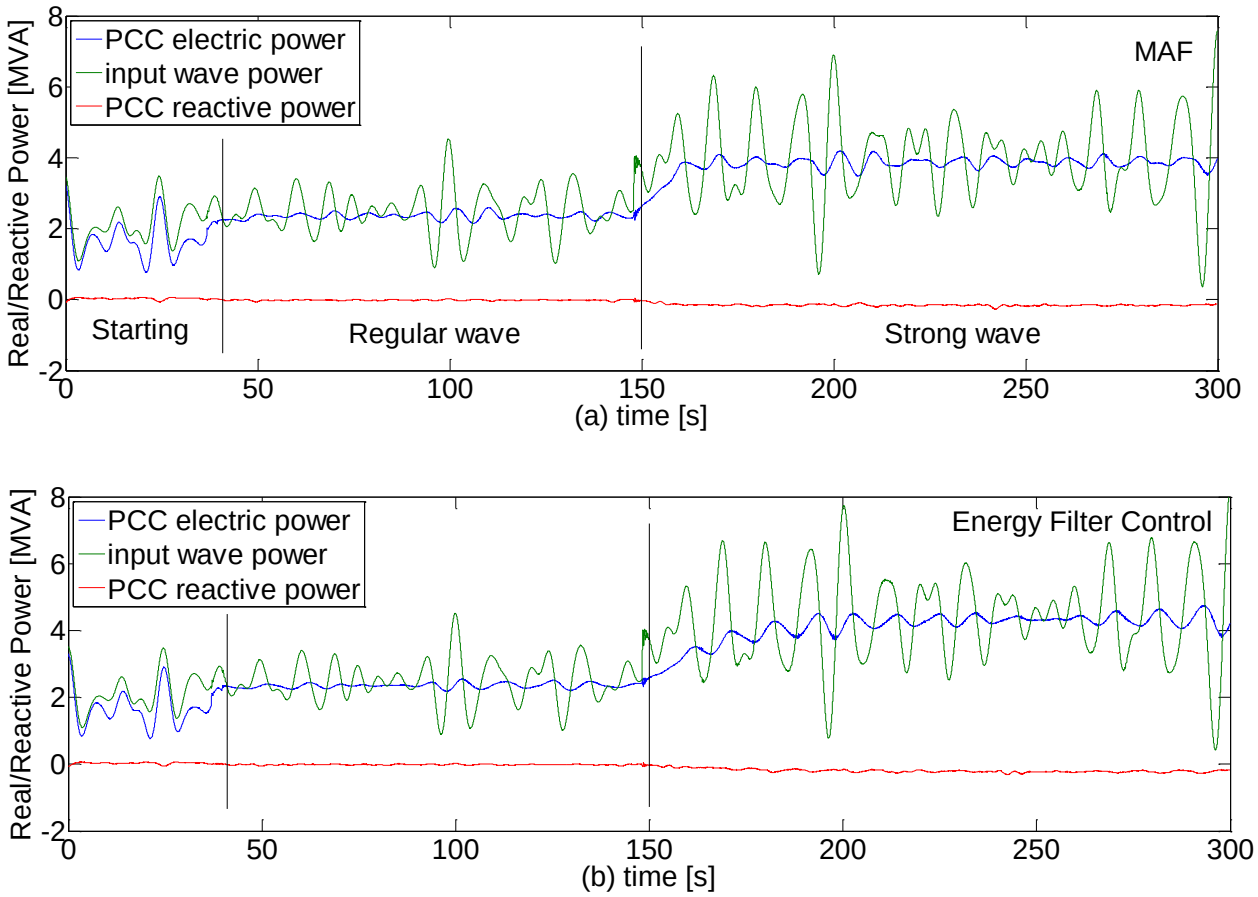

Fig. 6.6 The input wave power and the total output real and reactive power (*P*&*Q*) of the wavefarm system under: (a) MAF control and (b) energy filter control

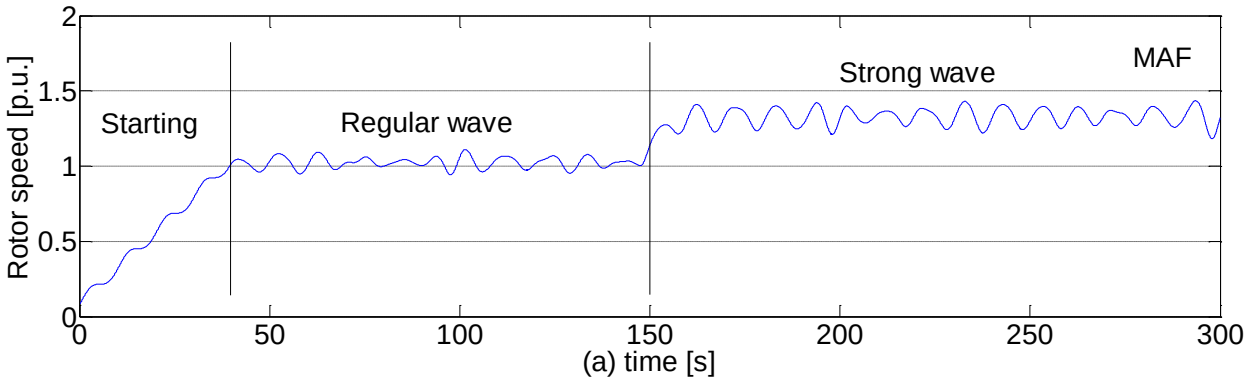

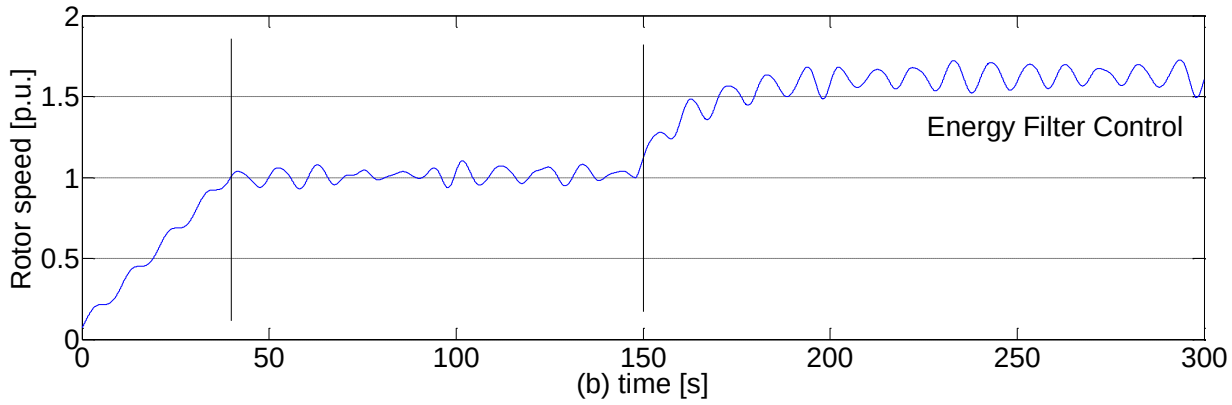

Fig. 6.7 The per-unit rotor speed of the master machine #1 under: (a) MAF control and (b) energy filter control

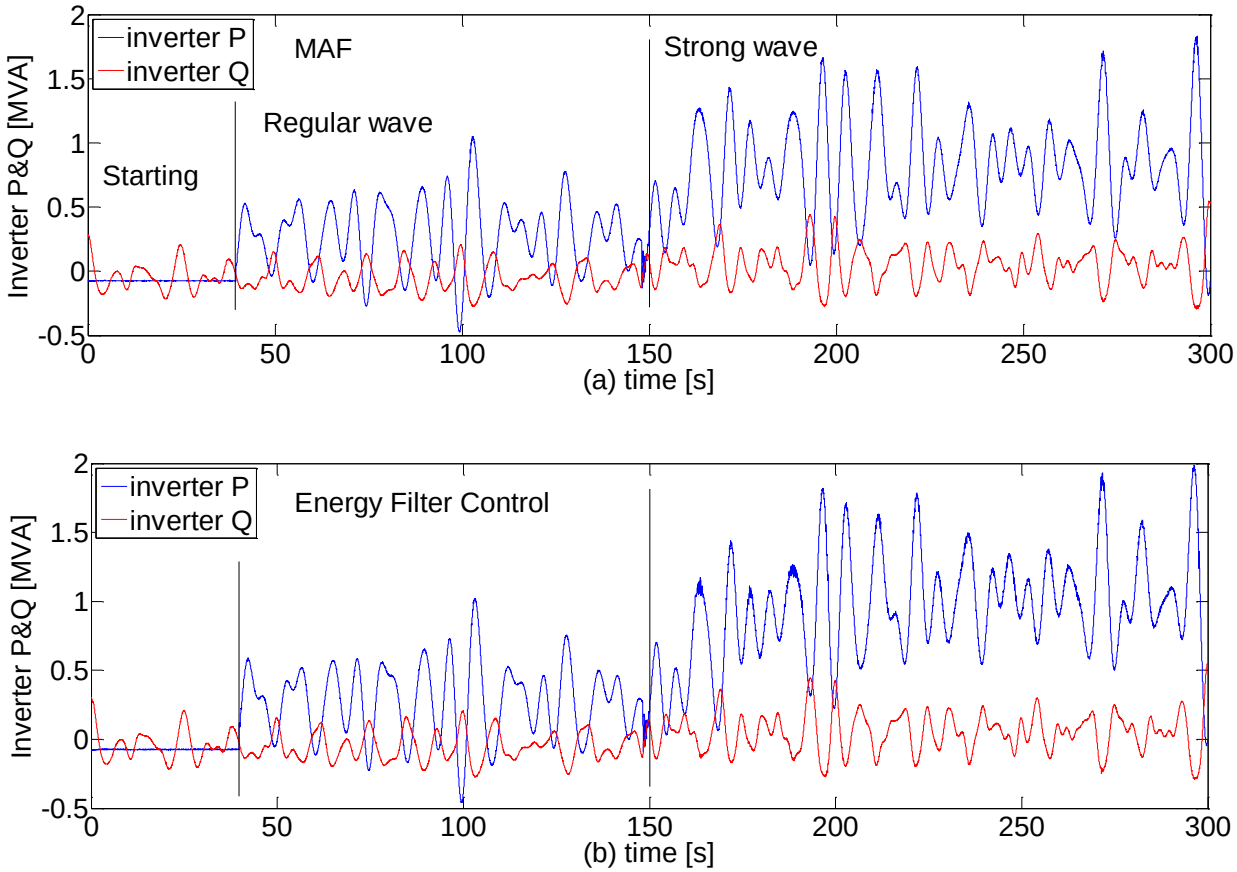

Fig. 6.8 The real and reactive power from the master inverter #1 to PCC under: (a) MAF control and (b) energy filter control

Table 6.1 presents a quantitative comparison between the two controls. Because of the randomness in the frequencies and phases of the driving torques, there is a marginal difference between the average input power under two controls. The power smoothing capability of the proposed system is quantified by the index σ, which is defined as the ratio between the standard deviations of the harvested wave power and that of the total output power. Accordingly, both control methods significantly reduce the standard deviation of the power flow; and the energy filter is better than the MAF with a larger σ and a better power smoothing capability.

Table 6.1 Real-time performances' comparison between the two control methods

Control method	avg. *Pin*	avg. *Pbus*	SD. *Pin*	SD. *Pbus*	$\boldsymbol{\eta_w}$	**σ**	**SD. $\boldsymbol{\omega}$**
MAF	2.418	2.379	0.6711	0.0855	98.40%	7.849	0.0708
Energy Filter	2.330	2.286	0.6905	0.0800	98.10%	8.631	0.0379

* *Pin* the input wave power (MW); *Pbus* the total output power on the PCC (MW); ω the per unit speed of #1 master rotor.

* avg. stands for the average value; SD stands for the standard deviation.

* η_w the wave farm system efficiency, which is the ratio of avg. *Pbus* over avg. *Pin*.

* σ the index of the power smoothing capability, which is the ratio of SD; *Pin* over SD; *Pbus*.

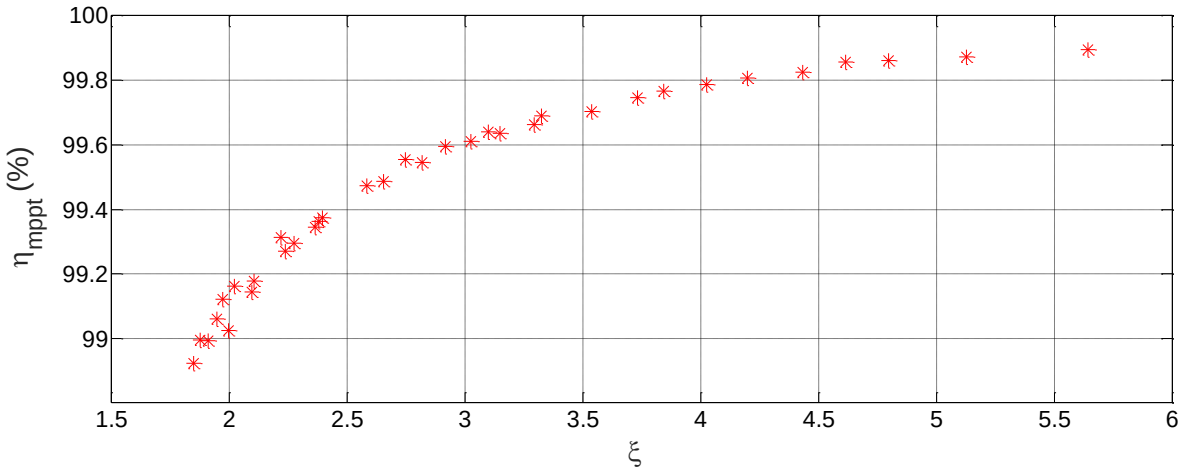

Fig. 6.9 The MPPT efficiency loss of OWC wave power generation under EF control

When PTO devices of master machines are OWCs, conventionally, rotor speeds must follow the MPPT control to maximize the power capture. When EF control is used to smooth the output power of the wave farm by manipulating rotor speeds of masters, rotor speeds go away from the optimum points set by the MPPT control. This leads to a loss of the MPPT efficiency, which is presented in Fig. 6.9. The MPPT efficiency η_{mppt} is the ratio of the total output energy of the wave farm in 300s under EF control over that under the MPPT control. The master-slave ratio ξ is defined as the installed capacity ratio of masters over slaves. As can be seen, the MPPT efficiency loss is less than 1% as long as $\xi > 2.0$.

6.4.3 Time Constant Selection of the EF Control

In order to study how the selection of the time constant in the EF control method affects the power smoothing capability and the rotor speed sensitivity, simulations are conducted with different values of *T*. Referring to (6.5) and (6.9), in these simulations the average input wave power is set as 10%, 20% and 30% larger than the rated total power output P_0 in the control law, respectively. This mismatch of P_0 in the control law and the actual average input wave

power is called the power error, for which the average master rotor speed would leave from 1.0 p.u. and the speed bias depends on the rotor speed sensitivity *T/H*. With a given power error, for each value of *T*, the statistical data is collected and averaged from 3 periods of 120 s steady state operations; $H = 21.15$.

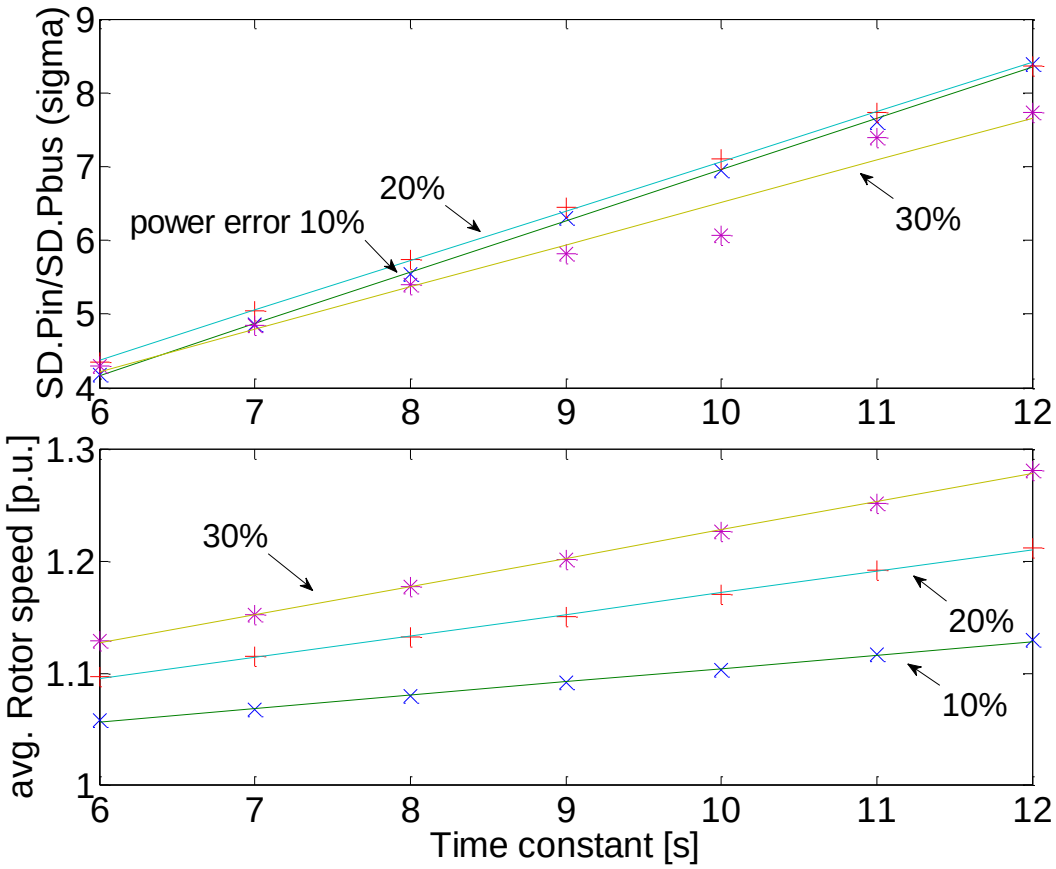

Fig. 6.10 The power smoothing capacity of the system assessed by sigma σ (above) and the rotor speed sensitivity assessed by the speed bias (below) under different values of *T* and power error

The simulation results of the actual data and their linear regression are presented in Fig. 6.10. It shows a clear positive and almost linear correlation between the time constant and both the smoothing effect and the speed sensitivity. As has been discussed, a larger time constant of

the system controller leads to both better power smoothing capability and larger speed bias of the master rotors. The selection of T would be a trade-off between these two variables according to a quantitative analysis, as given in Fig. 6.10. For example, when the estimated power error is under 30% and the maximum allowed average rotor speed is 1.2 per unit, the maximum T would be 9.

Summary

This chapter has proposed a master-slave wave farm system with the energy storage of rotor inertia. Two wave farm control methods have been proposed. The proposed system and the control methods are able to deliver smoothed real power to the grid and actively control its power factor at the point of common coupling. Due to the master-slave structure, the number of power converters in the wave farm could be reduced. Compared with the conventional energy buffers, the new wave farm system needs no extra energy storage system; it utilizes the rotor inertia of its own generators or added flywheels coupled on the rotors. Another advantage of the proposed system is that the power flow is smoothed at the stator of the electric machines; thus, no thermal excursion exists in the electrical sector of the wave farm and no VSC terminal needs to be over-rated. These advantages facilitate the construction of a wave farm with a large number of power take-off devices in a cost-effective way.

To make the total power delivered to the onshore grid track the average of the total input/captured wave power, two wave farm control methods have been proposed and demonstrated comparatively. There is the moving average filter (MAF) method, whose power smoothing effect is a standard to be compared with, but the inevitable mechanical power measurement of all the master generators is a drawback. The other method is the EF control

discussed in Chapter 5. This method needs no measurement of the mechanical power, but only needs to measure the rotor speed of the master machines and the electric power from the slaves; both of which can be easily obtained in engineering practices.

The proposed wave farm system has been simulated on the RTDS platform. The time domain simulations and the quantitative analysis have demonstrated the functionalities of both the control methods. Simulations of system faults have demonstrated the FRT capability regarding the UK grid code.

CHAPTER 7 CONCLUSIONS

7.1 Contributions and Concluding Remarks

This thesis has discussed the development of an EES-integrated fluctuating renewable power plant, which is related to the solar, wind and wave resources in nature and a group of EES technologies. The architecture of such a power plant is described via three layers: the converter layer, the unit layer and the system layer. In this research, the PI parameters' determination in the dq decoupling control of VSCs, the energy filter (EF) and the master-slave wave farm system are discussed in each of these three layers, respectively. In addition, the concept of energy quality is proposed to quantify the fluctuation and intermittency of variant power sources, for the first time to the best knowledge of the author. Overall, the original works presented in this thesis contribute to the further development and the increasing penetration of fluctuating renewable power generation.

Firstly, based on a comprehensive review of the modelling of VSC converter control systems, the PI parameters' determination in the dq decoupling control is studied with new mathematical insights; the limitations of the conventional method are indicated. Against these limitations, the second-order control and the virtual resistance control methods are proposed, which can calculate the desirable PI parameters according to given time-domain control objectives. Conclusions on this subject can be drawn as:

(1) The VSC converter-based control systems used in the fluctuating renewable power generation can be classified into four kinds when the converter is connected to: 1) the local grid; 2) a permanent magnetic synchronous machine (PMSM); 3) the stator of an induction machine; and 4) the rotor of an induction machine (DFIG). In these four kinds, the converters apply a different outer loop control but similar inner loop control.

(2) The conventional zero-pole cancelling method to determine the PI parameters is both controllable and observable in the state-space model analysis. However, the cancelled zero creates a hidden dynamic in the system.

(3) The hidden dynamic is asymptotically stable, but the time of convergence is related to the interface resistance of the converter; which could be the short-circuit resistor of a transformer, or the winding resistance of an electric machine. The smaller the interface resistance, the slower the hidden dynamic converges to zero. In most practical cases, there is usually a sufficient interface resistance so the hidden dynamic fades quickly enough and has no significant impacts on the control system. However in extreme cases, of for example a superconducting machine or transformer, the lack of interface resistance makes the hidden dynamic no longer convergent and simulation results show that there would be an uncontrollable bias in the dq currents.

(4) The second-order control method removes the hidden dynamic; and the virtual resistance method is able to reposition the pole of the hidden dynamic on the s-plane. Both of the methods are able to determine the PI parameters for the dq decoupling control with given time-domain objectives, with or without a sufficient interface resistance. Case studies are conducted to demonstrate the theoretical analysis and proposed methods.

Secondly, the conventional concept of power quality is well used to describe the magnitude, frequency and harmonics of voltage/current waveforms. In this research, for the first time, the power quality is generalized to the concept of energy quality, which is a useful tool to quantify the fluctuation and intermittency of a variant power flow. The proposed energy quality involves two aspects: the magnitude and harmonics of the power waveform. In mathematics, the former is described by the power level and the latter is described by the total power harmonic distortion (TPHD). Both the continuous and discrete forms of the power level and TPHD are given. It is mathematically demonstrated that the TPHD, which is originally generalized from the conventional total harmonic distortion (THD) in the framework of the power quality, actually equals to the coefficient of variance of the power waveform.

Thirdly, a family of EES-based control systems, designated as an energy filter, is proposed for the integration and control of the EES in the fluctuating power generation units. This control system could be implemented based on a variety of EES rather than limited to specific kinds. First, a simple but useful power dynamic model is proposed to summarize most of the mainstream EES systems and lay the foundation for the EF. Then, different EFs are developed in terms of their different topologies, orders and EES implementations. The transfer function of an EF is determined by its control parameters. Concluding remarks on this subject are drawn as:

(1) Mainstream EES technologies are classified into light and heavy storages. The light storages, which include flywheels, supercapacitors, superconducting magnetic energy storage (SMES) and light batteries, are more suitable for building an EF due to their high efficiency and fast response.

(2) The conversion loss of EES equivalently makes the inertia E_0 of the EF a changing parameter during the operation. For a light storage with efficiency of over 90%, this effect has no significant impacts on the system. However, when the EF is built on an EES with lower efficiency, the non-linearity caused by the changing parameter must be considered.

(3) On different topologies, series, parallel and hybrid EFs are proposed. The core difference between the series and parallel EFs is whether they can directly control the output power. The SEF can directly control the output power and it does not have to measure the input power. At a cost, the converters of the SEF have to transmit the full rated power. By comparison, the PEF cannot directly control the output power but only the EES power; and in order to control the output power indirectly it must measure the input power. The advantage of the PEF is that only the power fluctuations go through the converters. For these reasons, the topology selection is a trade-off between the power measurement difficulty and the converter capacity.

(4) The order and transfer function of the EF are solely determined by its control. With the same cut-off frequency, the second-order EF has a better power smoothing effect than the first-order EF, at a cost of higher storage level sensitivity.

Finally, based on all the knowledge presented above, a wave farm system in a master-slave structure is proposed for large-scale wave energy conversion in a grid-friendly and cost-effective way. The proposed wave farm system is able to largely smooth its total output power by controlling the rotor inertia of the master machines as self-energy storage devices.

The system could also reduce the number of converters in a wave farm with a large number of power generation units. At the system layer, the moving average filter (MAF) control and the EF control are studied comparatively. The fault case study shows that the system has the fault ride-through capability according to the UK grid code. Conclusively, the remarks on this subject are follows:

(1) Since the rotor inertia of the masters is used for self-energy storage, the masters have to be built based on PTOs using rotating electric machines (e.g. OWC, Pelamis). For point absorbers, the masters could be built when the primary linear movements are transferred to rotational movements through mechanical or hydraulic modules.

(2) The MAF control requires no historical data to estimate the power level of the wave resources. However, it needs to measure the electrical power of the slaves and the mechanical power of the masters. The latter is very difficult to obtain in engineering practices.

(3) The EF control is an application of the HEF to the master-slave wave farm system, where masters and slaves play the roles of the series and parallel pathways, respectively. By contrast with the MAF method, the EF control measures the rotor speeds instead of the mechanical power of the masters, which is more feasible for implementation; but this control depends on the estimated long-term average wave power of the site to set its operating point.

(4) With the conditions of the case studies, under both the MAF and EF control methods, the proposed wave farm system is able to generate a self-smoothed power flow with about 1/8 TPHD of the raw, fluctuating wave power captured.

7.2 Future Works

The correlation between the conventional power quality and the proposed energy quality has not been addressed in this study; although it is a deserving concept to be investigated in future works. For example, quantitative studies should be conducted on how the TPHD causes the frequency variation. The expected outcome could be a set of grid requirements to the TPHD of any power injection.

A series of extensive works on the proposed EF could be carried out in the future: 1) to develop an adaptive EF to its inertia, which could be useful when the inertia is changing (as the EES efficiency is low) or unknown; 2) to develop the EF for the smoothing of the fluctuating loads instead of power sources; 3) to make the EF applicable in smaller time scales by including the converter's dynamics into the modelling; and 4) a second-order EF with a small damping ratio can be made as a power oscillator at its resonant frequency, which may be useful in some special applications.

List of References

[1] "New Energy Outlook 2017," Bloomberg New Energy Finance, June 2017.

[2] N. Flourentzou, V. Agelidis, G. Demetriades , "VSC-based HVDC power transmission systems: An overview," IEEE Trans. on Power Electronics, vol. 24, no. 3, pp. 592-602, 2009.

[3] R. Pena, J. Clare, G. Asher, "Doubly fed induction generator using back-to-back PWM converters and its application to variable-speed wind-energy generation," IEE Proceedings-Electric Power Applications, vol. 143, no. 3, pp. 231-241, 1996.

[4] K. Ang, G. Chong, Y. Li, "PID control system analysis, design, and technology," IEEE Trans. on control systems technology, vol. 13, no. 4, pp. 559-576, 2005.

[5] W. K. Ho, C. C. Hang and J. H. Zhou, "Performance and gain and phase margins of well-known PI tuning formulas," in IEEE Transactions on Control Systems Technology, vol. 3, no. 2, pp. 245-248, Jun 1995.

[6] R. E. Precup, R. C. David, E. M. Petriu, M. B. Radac and S. Preitl, "Adaptive GSA-Based Optimal Tuning of PI Controlled Servo Systems With Reduced Process Parametric Sensitivity, Robust Stability and Controller Robustness," in IEEE Transactions on Cybernetics, vol. 44, no. 11, pp. 1997-2009, Nov. 2014.

[7] T. Kumbasar and H. Hagras, "A Self-Tuning zSlices-Based General Type-2 Fuzzy PI Controller," in IEEE Transactions on Fuzzy Systems, vol. 23, no. 4, pp. 991-1013, Aug. 2015.

[8] J. Rojas, D. Valverde-Méndez, V. Alfaro, "Comparison of multi-objective optimization methods for PI controllers tuning," in Proc. IEEE 20th Conference on Emerging Technologies & Factory Automation (ETFA), 2015, pp. 1-8.

[9] Z. Gaing, "A particle swarm optimization approach for optimum design of PID controller in AVR system," IEEE Trans. on energy conversion, vol. 19, no. 2, pp. 384-391, 2004.

[10] N. Nayak, S. Mishra, S. Choudhury, "Optimal design of VSC based HVDC using Particle Swarm Optimization technique," in Proc. Power, Control and Embedded Systems, 2012, pp. 1-5.

[11] R. N. Tripathi and T. Hanamoto, "FRIT based optimized PI tuning for DC link voltage control of grid connected solar PV system," IECON 2015 - 41st Annual Conference of the IEEE Industrial Electronics Society, Yokohama, 2015, pp. 001567-001572.

[12] S. Chacko, C. N. Bhende, S. Jain and R. K. Nema, "PSO based online tuning of PI controller for estimation of rotor resistance of indirect vector controlled induction motor drive," 2016

International Conference on Electrical, Electronics, and Optimization Techniques (ICEEOT), Chennai, 2016.

[13] H. M. Yassin, H. H. Hanafy and M. M. Hallouda, "Design and implementation of PI controllers of direct drive PMSG wind turbine system tuned by Linearized biogeography-based optimization technique," IECON 2016 - 42nd Annual Conference of the IEEE Industrial Electronics Society.

[14] N. Chaudhuri, B. Chaudhuri, R. Majumder, Multi-terminal Direct-current Grids: Modeling, Analysis, and Control. John Wiley & Sons, 2014.

[15] N. M. Kangwa, C. Venugopal and I. E. Davidson, "A review of the performance of VSC-HVDC and MTDC systems," 2017 IEEE PES PowerAfrica, Accra, 2017, pp. 267-273.

[16] L. Xiao, Z. Xu, T. An and Z. Bian, "Improved Analytical Model for the Study of Steady State Performance of Droop-Controlled VSC-MTDC Systems," in IEEE Transactions on Power Systems, vol. 32, no. 3, pp. 2083-2093, May 2017.

[17] A. Ortega, F. Milano, "Generalized Model of VSC-based Energy Storage Systems for Transient Stability Analysis," IEEE Trans. on power systems, vol. 31, no. 5, pp. 3369-3380, 2016.

[18] S. R. Arya, R. Niwas, K. Kant Bhalla, B. Singh, A. Chandra and K. Al-Haddad, "Power Quality Improvement in Isolated Distributed Power Generating System Using DSTATCOM," in IEEE Transactions on Industry Applications, vol. 51, no. 6, pp. 4766-4774, Nov.-Dec. 2015.

[19] M. I. Daoud, A. M. Massoud, A. S. Abdel-Khalik, A. Elserougi and S. Ahmed, "A Flywheel Energy Storage System for Fault Ride Through Support of Grid-Connected VSC HVDC-Based Offshore Wind Farms," in IEEE Transactions on Power Systems, vol. 31, no. 3, pp. 1671-1680, May 2016.

[20] P. Malysz, S. Sirouspour, A. Emadi, "An optimal energy storage control strategy for grid-connected microgrids," IEEE Trans. on Smart Grid, vol. 5, no. 4, pp. 1785-1796, 2014.

[21] M. Sandgani, S. Sirouspour, "Coordinated Optimal Dispatch of Energy Storage in a Network of Grid-connected Microgrids," IEEE Trans. on Sustainable Energy, vol. 8, no. 3, pp. 1166-1176, 2017.

[22] A. Barnes, J. Balda, A. Escobar-Mejía, "A semi-Markov model for control of energy storage in utility grids and microgrids with PV generation," IEEE Trans. on Sustainable Energy, vol. 6, no. 2, pp. 546-556, 2015.

[23] X. Zhao, Z. Yan, Xiao-Ping Zhang, "A Wind-Wave Farm System with Self-Energy Storage and Smoothed Power Output," IEEE Access, vol. 4, pp. 8634-8642, 2016.

[24] M. Eltawil, Z. Zhao, "Grid-connected photovoltaic power systems: Technical and potential problems—A review," Renewable and Sustainable Energy Reviews, vol. 14, no.1, pp. 112-129, 2010.

[25] A. Blavette, D. L. O'Sullivan, R. Alcorn, T. W. Lewis, M. G. Egan, "Impact of a Medium-Size Wave Farm on Grids of Different Strength Levels," IEEE Trans. on Power Systems, vol. 29, no. 2, pp. 917-923, March 2014.

[26] B. Singh, R. Saha, A. Chandra, "Static synchronous compensators (STATCOM): a review," IET Power Electronics, vol. 2, no. 4, pp. 297-324, 2009.

[27] T. Ma, M. H. Cintuglu and O. A. Mohammed, "Control of a Hybrid AC/DC Microgrid Involving Energy Storage and Pulsed Loads," IEEE Trans. on Industry Applications, vol. 53, no. 1, pp. 567-575, Jan.-Feb. 2017.

[28] Á. Ortega and F. Milano, "Modeling, Simulation, and Comparison of Control Techniques for Energy Storage Systems," IEEE Trans. on Power Systems, vol. 32, no. 3, pp. 2445-2454, May 2017.

[29] H. M. Hasanien, "A Set-Membership Affine Projection Algorithm-Based Adaptive-Controlled SMES Units for Wind Farms Output Power Smoothing," IEEE Trans. on Sustainable Energy, vol. 5, no. 4, pp. 1226-1233, Oct. 2014.

[30] F. J. Lin, H. C. Chiang, J. K. Chang and Y. R. Chang, "Intelligent wind power smoothing control with BESS," IET Renewable Power Generation, vol. 11, no. 2, pp. 398-407, 2017.

[31] A. M. Howlader, T. Senjyu and A. Y. Saber, "An Integrated Power Smoothing Control for a Grid-Interactive Wind Farm Considering Wake Effects," IEEE Systems Journal, vol. 9, no. 3, pp. 954-965, Sept. 2015.

[32] I. Ngamroo and T. Karaipoom, "Cooperative Control of SFCL and SMES for Enhancing Fault Ride Through Capability and Smoothing Power Fluctuation of DFIG Wind Farm," IEEE Trans. on Applied Superconductivity, vol. 24, no. 5, pp. 1-4, Oct. 2014.

[33] T. I. Bø and T. A. Johansen, "Battery Power Smoothing Control in a Marine Electric Power Plant Using Nonlinear Model Predictive Control," IEEE Trans. on Control Systems Technology, vol. 25, no. 4, pp. 1449-1456, July 2017.

[34] Z. Zhou, F. Scuiller, J. F. Charpentier, M. E. H. Benbouzid and T. Tang, "Power Smoothing Control in a Grid-Connected Marine Current Turbine System for Compensating Swell Effect," IEEE Trans. on Sustainable Energy, vol. 4, no. 3, pp. 816-826, July 2013.

[35] T. Martinsen et al., "Improved grid operation through power smoothing control strategies utilizing dedicated energy storage at an electric vehicle charging station," in CIRED Workshop 2016, Helsinki, 2016, pp. 1-4.

[36] X. Luo, J. Wang, M. Dooner, J. Clarke, "Overview of current development in electrical energy storage technologies and the application potential in power system operation," Applied Energy, vol. 137, pp. 511-536, 2015.

[37] Piller power systems products. Energy storage. n.d. <http://www.piller.com/205/energy-storage> [accessed 15.08.17].

[38] Beacon power technology. Beacon Power Corporation. n.d. <http://beaconpower.com/ resources/> [accessed 30.08.17].

[39] Farret FA, Simons MG. Integration of alternative sources of energy. John Wiley & Sons Inc.; 2006. page. 262-300.

[40] Shoenung SM. Characteristics and technologies for long- vs. short-term energy storage: a study by the DOE energy storage systems program. Technical report. SAND2001-0765. Sandia National Laboratories. United States Department of Energy. Published March 2001.

[41] J. W. Zha, N. Huang, K. Q. He, Z. M. Dang, C. Y. Shi and R. K. Li, "Electrospun poly(ethylene oxide) nanofibrous composites with enhanced ionic conductivity as flexible solid polymer electrolytes," in High Voltage, vol. 2, no. 1, pp. 25-31, 3 2017.

[42] Rastler D. Electricity energy storage technology options: a white paper primer on applications, costs, and options. Electric Power Research Institute (EPRI). Technical report. Published December 2010.

[43] Energy storage & renewables overview, solutions and customer case studies. Saft Batteries. n.d. <http://www.saftbatteries.com/market-solutions/energystorage-renewables> [accessed 29.08.17].

[44] Tweed K. UK launches Europe's largest energy storage trial. IEEE Spectrum. Published 1st August 2013. <http://spectrum.ieee.org/energywise/energy/ the-smarter-grid/uk-launches-europes-largest-energy-storage-trial> [accessed 05.09.17].

[45] Chen H, Cong TN, Yang W, Tan C, Li Y, Ding Y. Progress in electrical energy storage system: a critical review. Prog Nat Sci 2009;19:291–312.

[46] Beaudin M, Zareipour H, Schellenberglabe A, Rosehart W. Energy storage for mitigating the variability of renewable electricity sources: an updated review. Energy Sust Dev 2010;14:302–14.

[47] T. Kovaltchouk, B. Multon, H. Ben Ahmed, J. Aubry and P. Venet, "Enhanced Aging Model for Supercapacitors Taking Into Account Power Cycling: Application to the Sizing of an Energy Storage System in a Direct Wave Energy Converter," in IEEE Transactions on Industry Applications, vol. 51, no. 3, pp. 2405-2414, May-June 2015.

[48] J. M. Sandoval, M. J. Espinoza Trujillo, M. I. Flota Buñuelos, J. L. Duran Gómez, J. Y. Verde Gómez and D. E. Pacheco-Catalán, "Batteries-supercapacitors storage systems for a mobile

hybrid renewable energy system," 2013 IEEE Electrical Power & Energy Conference, Halifax, NS, 2013, pp. 1-4.

[49] Electrical energy storage: white paper. Technical report. Prepared by electrical energy storage project team. International Electrotechnical Commission (IEC), Published December 2011.

[50] Smith SC, Sen PK, Kroposki B. Advancement of energy storage devices and applications in electrical power system. In: 2008 IEEE Power Energy Soc. Gen. Meet. – Convers. Deliv. Electr. Energy 21st Century, IEEE; 2008. p. 1–8.

[51] X. P. Zhang and P. Zeng, "Marine Energy Technology [Sanning the Issue]," in Proceedings of the IEEE, vol. 101, no. 4, pp. 862-865, April 2013.

[52] Z. Zhang et al., "Adaptive damping power take-off control for a three-body wave energy converter," 2013 IEEE Energy Conversion Congress and Exposition, Denver, CO, 2013, pp. 321-328.

[53] T. Ahmed, K. Nishida and M. Nakaoka, "Grid power integration technologies for offshore ocean wave energy," 2010 IEEE Energy Conversion Congress and Exposition, Atlanta, GA, 2010, pp. 2378-2385.

[54] Sousa Prado, M. Goden, et al. "Modelling and test results of the Archimedes wave swing." Proceedings of the Institution of Mechanical Engineers, Part A: Journal of Power and Energy 220.8 (2006): 855-868.

[55] Mouslim, Hakim, et al. "Development of the french wave energy test site SEM-REV." Proceedings of the 8th European wave and tidal energy conference, Uppsala, Sweden. 2009.

[56] H. Polinder and M. Scuotto, "Wave energy converters and their impact on power systems," 2005 International Conference on Future Power Systems, Amsterdam, 2005, pp. 9 pp.-9.

[57] T. K. A. Brekken, H. T. Ozkan-Haller and A. Simmons, "A Methodology for Large-Scale Ocean Wave Power Time-Series Generation," in IEEE Journal of Oceanic Engineering, vol. 37, no. 2, pp. 294-300, April 2012.

[58] B. Guo, R. Patton, M. Abdelrahman and J. Lan, "A continuous control approach to point absorber wave energy conversion," 2016 UKACC 11th International Conference on Control (CONTROL), Belfast, 2016, pp. 1-6.

[59] B. Guo, R. Patton, S. Jin, J. Gilbert and D. Parsons, "Non-linear Modelling and Verification of a Heaving Point Absorber for Wave Energy Conversion," in IEEE Transactions on Sustainable Energy, vol. PP, no. 99, pp. 1-1.

[60] F. Wu, X. P. Zhang, P. Ju and M. J. H. Sterling, "Optimal Control for AWS-Based Wave Energy Conversion System," in IEEE Transactions on Power Systems, vol. 24, no. 4, pp. 1747-1755, Nov. 2009.

[61] Henderson, Ross. "Design, simulation, and testing of a novel hydraulic power take-off system for the Pelamis wave energy converter." Renewable energy 31.2 (2006): 271-283.

[62] D. P. Marčetić, I. R. Krčmar, M. A. Gecić and P. R. Matić, "Discrete Rotor Flux and Speed Estimators for High-Speed Shaft-Sensorless IM Drives," in IEEE Transactions on Industrial Electronics, vol. 61, no. 6, pp. 3099-3108, June 2014.

[63] D. Stojić, M. Milinković, S. Veinović and I. Klasnić, "Improved Stator Flux Estimator for Speed Sensorless Induction Motor Drives," in IEEE Transactions on Power Electronics, vol. 30, no. 4, pp. 2363-2371, April 2015.

[64] Z. Yan, Y. Xue, X. P. Zhang, "PI parameters determination in dq decoupling control of VSC terminals," 13th IET International Conference on AC and DC Power Transmission (ACDC 2017), Manchester, 2017, pp. 1-5.

[65] "First benchmark model for computer simulation of subsynchronous resonance," in IEEE Transactions on Power Apparatus and Systems, vol. 96, no. 5, pp. 1565-1572, Sept. 1977.

[66] C. K. Sao, P. W. Lehn, M. R. Iravani and J. A. Martinez, "A benchmark system for digital time-domain simulation of a pulse-width-modulated D-STATCOM," in IEEE Transactions on Power Delivery, vol. 17, no. 4, pp. 1113-1120, Oct 2002.

[67] Farley, F. J. M. "Opening remarks and the power spectrum of ocean waves." (2012): 203-207.

[68] Z. Yan, X. P. Zhang, "General Energy Filters for Power Smoothing, Tracking and Processing Using Energy Storage," in IEEE Access, vol. 5, pp. 19373-19382, 2017.

[69] J. S. Park, B. G. Gu, J. R. Kim, I. H. Cho, I. Jeong and J. Lee, "Active Phase Control for Maximum Power Point Tracking of a Linear Wave Generator," in IEEE Transactions on Power Electronics, vol. 32, no. 10, pp. 7651-7662, Oct. 2017.

[70] H. Mendonca and S. Martinez, "A resistance emulation approach to optimize the wave energy harvesting for a direct drive point absorber," in IEEE Transactions on Sustainable Energy, vol. 7, no. 1, pp. 3-11, Jan. 2016.

[71] H. M. Hasanien, "Gravitational search algorithm-based optimal control of archimedes wave swing-based wave energy conversion system supplying a DC microgrid under uncertain dynamics," in IET Renewable Power Generation, vol. 11, no. 6, pp. 763-770, 5 10 2017.

[72] N. Tom and R. W. Yeung, "Experimental Confirmation of Nonlinear-Model- Predictive Control Applied Offline to a Permanent Magnet Linear Generator for Ocean-Wave Energy Conversion," in IEEE Journal of Oceanic Engineering, vol. 41, no. 2, pp. 281-295, April 2016.

[73] J. Lekube, A. J. Garrido and I. Garrido, "Rotational Speed Optimization in Oscillating Water Column Wave Power Plants Based on Maximum Power Point Tracking," in IEEE Transactions on Automation Science and Engineering, vol. 14, no. 2, pp. 681-691, April 2017.

[74] F. Mzoughi, S. Bouallègue, A. J. Garrido, I. Garrido and M. Ayadi, "Stalling-free Control Strategies for Oscillating-Water-Column-based Wave Power Generation Plants," in IEEE Transactions on Energy Conversion, vol. PP, no. 99, pp. 1-1.

[75] M. Amundarain, M. Alberdi, A. J. Garrido and I. Garrido, "Modeling and Simulation of Wave Energy Generation Plants: Output Power Control," in IEEE Transactions on Industrial Electronics, vol. 58, no. 1, pp. 105-117, Jan. 2011.

[76] A. Blavette, D. L. O'Sullivan, R. Alcorn, T. W. Lewis and M. G. Egan, "Impact of a Medium-Size Wave Farm on Grids of Different Strength Levels," in IEEE Transactions on Power Systems, vol. 29, no. 2, pp. 917-923, March 2014.

[77] A. Blavette, D. L. O'Sullivan, R. Alcorn, M. G. Egan and T. W. Lewis, "Simplified Estimation of the Flicker Level Induced by Wave Energy Farms," in IEEE Transactions on Sustainable Energy, vol. 7, no. 3, pp. 1216-1223, July 2016.

[78] S. Armstrong, E. Cotilla-Sanchez and T. Kovaltchouk, "Assessing the Impact of the Grid-Connected Pacific Marine Energy Center Wave Farm," in IEEE Journal of Emerging and Selected Topics in Power Electronics, vol. 3, no. 4, pp. 1011-1020, Dec. 2015.

[79] L. Wang, H. W. Li and C. T. Wu, "Stability Analysis of an Integrated Offshore Wind and Seashore Wave Farm Fed to a Power Grid Using a Unified Power Flow Controller," in IEEE Transactions on Power Systems, vol. 28, no. 3, pp. 2211-2221, Aug. 2013.

[80] J. Sjolte, G. Tjensvoll and M. Molinas, "All-electric Wave Energy Converter array with energy storage and reactive power compensation for improved power quality," 2012 IEEE Energy Conversion Congress and Exposition (ECCE), Raleigh, NC, 2012, pp. 954-961.

[81] E. Tedeschi, M. Carraro, M. Molinas and P. Mattavelli, "Effect of Control Strategies and Power Take-Off Efficiency on the Power Capture From Sea Waves," in IEEE Transactions on Energy Conversion, vol. 26, no. 4, pp. 1088-1098, Dec. 2011.

[82] J. Du, D. Liang, X. Liu, "Performance Analysis of a Mutually Coupled Linear Switched Reluctance Machine for Direct Drive Wave Energy Conversions," in IEEE Trans. on Magnetics, early access.

[83] A. Wahyudie, M. Jama, T. B. Susilo, B. F. Mon, H. Shaaref, H. Noura, "Design and testing of a laboratory scale test rig for wave energy converters using a double-sided permanent magnet linear generator," IET Renewable Power Generation, vol. 11, no. 7, 2017, pp. 922-930.

[84] J. Robinson, G. Joos. "VSC HVDC transmission and offshore grid design for a linear generator based wave farm." in Proc. Electrical and Computer Engineering, CCECE'09. Canadian Conference on. IEEE, 2009, pp. 54-58.

[85] E. Lejerskog, C. Bostrom, L. Hai, R. Waters, M. Leijon, "Experimental results on power absorption from a wave energy converter at the Lysekil wave energy research site," Renewable Energy, vol. 77, 2015, pp. 9-14.

[86] L. Wang, S. Jan, C. Li, H. Li, Y. Huang, Y. Chen, S. Wang, “Study of a hybrid offshore wind and seashore wave farm connected to a large power grid through a flywheel energy storage system,” In Power and Energy Society General Meeting, July. 2011, pp. 1-7.

[87] A. Garces, E. Tedeschi, G. Verez, M. Molinas, “Power collection array for improved wave farm output based on reduced matrix converters,” In Control and Modeling for Power Electronics (COMPEL), 2010 IEEE 12th Workshop on, 2010, pp. 1-6.

[88] A. Blavette, D. L. O'Sullivan, T. W. Lewis, M. G. Egan, “Dimensioning the equipment of a wave farm: Energy storage and cables,” IEEE Trans. on Industry Applications, vol. 51, no. 3, 2015, pp. 2470-2478.

[89] E. Tedeschi, M. Santos-Mugica, “Modeling and control of a wave energy farm including energy storage for power quality enhancement: The Bimep case study,” IEEE Trans. on Power Systems, vol. 29, no. 3, 2014, pp. 1489-1497.

[90] S. Li, R. Challoo and M. J. Nemmers, "Comparative study of DFIG power control using stator-voltage and stator-flux oriented frames," 2009 IEEE Power & Energy Society General Meeting, Calgary, AB, 2009, pp. 1-8.

[91] G. Calderon Zavala, J. D. Mina Antonio, J. C. Rosas Caro, M. Madrigal Martinez, A. Claudio Sanchez and A. R. Lopez Nunez, "Simulation and Comparative Analysis of DFIG-based WECS Using Stator Voltage and Stator Flux Reference Frames," in IEEE Latin America Transactions, vol. 15, no. 6, pp. 1052-1059, June 2017.

[92] L. Tan, A. Gole, C. Zhao, “Harmonic Instability in MMC-HVDC Converters Resulting from Internal Dynamics,” IEEE Trans. on power delivery, vol. 31, no. 4, pp. 1738-1747, 2016.

[93] Solar-PV power generation data – Elia. <http://www.elia.be/en/grid-data/power-generation/Solar-power-generation-data/Graph> [accessed 03.09.17]

[94] Solar data power for integration studies. Grid modernization. NREL. <https://www.nrel.gov/grid/solar-power-data.html> [accessed 03.09.17]

[95] Winderzeugung. < http://www.oem-ag.at/de/oekostromneu/winderzeugung/> [accessed 04.09.17]

[96] D. Akinyele, R. K. Rayudu, "Review of energy storage technologies for sustainable power networks," Sustainable Energy Technologies and Assessments, vol. 8, pp. 74-91, 2014.

[97] A. H. Slocum, G. E. Fennell, G. Dundar, B. G. Hodder, J. D. C. Meredith and M. A. Sager, "Ocean Renewable Energy Storage (ORES) System: Analysis of an Undersea Energy Storage Concept," Proceedings of the IEEE, vol. 101, no. 4, pp. 906-924, April 2013.

[98] S. Jafarishiadeh, M. Farasat and A. M. Bozorgi, "Modeling, analysis and design of an undersea storage system," in 2016 IEEE Energy Conversion Congress and Exposition (ECCE), Milwaukee, WI, 2016, pp. 1-6.

[99] N. Dimitrijevic et al., "Role of water and carbonates in photocatalytic transformation of CO2 to CH4 on titania," Journal of the American Chemical Society, vol. 133, no.11, pp. 3964-3971, 2011.

[100] T. Desrues, J. Ruer, P. Marty, J. F. Fourmigue, "A thermal energy storage process for large scale electric applications," Applied Thermal Engineering, vol. 30, no. 5, pp. 425-432, 2010.

[101] W. Chang, "The state of charge estimating methods for battery: A review," ISRN Applied Mathematics, 2013.

[102] J. V. Kringelum, M. H. Donovan, O. B. Fosso, J. L. Garcia, A. Pozo, "Grid connection and macro-system integration of combined wind and wave devices," in Proc. Ecological Vehicles and Renewable Energies (EVER), IEEE, Monte-Carlo, Monaco, 27-30 March 2013, pp. 1-7.

[103] R. Henderson, "Design, simulation, and testing of a novel hydraulic power take-off system for the Pelamis wave energy converter," Renewable energy, vol. 31, no. 2, 2006, pp. 271-283.

[104] S. Ceballos, J. Rea, I. Lopez, "Efficiency optimization in low inertia wells turbine-oscillating water column devices," IEEE Trans. on Energy Conversion, vol. 28, no. 3, Sep. 2013, pp. 553 - 564.

[105] Z. Qin, F. Blaabjerg, "A rotating speed controller design method for power leveling by means of inertia energy in wind power system," IEEE Trans. on Energy Conversion, vol. 30, no. 3, Sep. 2015, pp. 1052 - 1060.

[106] A. Feijóo, J. Cidrás, C. Carrillo, "A third order model for the doubly-fed induction machine," Electric Power Systems Research, vol. 56, no. 2, Mar, 2000, pp. 121-127.

[107] S. Chondrogiannis, et al, "Modelling and GB grid code compliance studies of offshore wind farms with doubly-fed induction generators," in Proc. The 3rd IET International Conference on Power Electronics, Machines and Drives, 2006, pp. 22-26.

[108] X. Zhao, Z. Yan and X. P. Zhang, "A Wind-Wave Farm System With Self-Energy Storage and Smoothed Power Output," in IEEE Access, vol. 4, pp. 8634-8642, 2016.

PUBLICATIONS

Journal Papers

[1] Z. Yan and X. P. Zhang, "General Energy Filters for Power Smoothing, Tracking and Processing Using Energy Storage," in IEEE Access, vol. 5, pp. 19373-19382, 2017.

[2] X. Zhao, Z. Yan and X. P. Zhang, "A Wind-Wave Farm System With Self-Energy Storage and Smoothed Power Output," in IEEE Access, vol. 4, pp. 8634-8642, 2016.

[3] X. Zhao, Z. Yan, Y. Xue and X. P. Zhang, "Wind Power Smoothing by Controlling the Inertial Energy of Turbines With Optimized Energy Yield," in IEEE Access, vol. 5, pp. 23374-23382, 2017.

Conference Papers

[4] Z. Yan, Y. Xue and X. P. Zhang, "PI parameters determination in dq decoupling control of VSC terminals," 13th IET International Conference on AC and DC Power Transmission (ACDC 2017), Manchester, 2017, pp. 1-5.

Appendix A

Simulation parameters of the real-grid-STATCOM-motor system studied in Chapter 3.

Frequency of the system

$f_B = 50Hz$

***IEEE* benchmark synchronous generator**

Governor/Turbine IEEE Type 1, PSS IEE2ST, System Excitation IEEE Type ST1.

$S_n = 4MVA, V_{rms,line} = 11kV, H = 1.0s, D = 0.1\ (pu)$

Electrical parameters in per unit values

Xa=0.2327, Xd=1.7134, Xd'=0.4345, Xd''=0.3253,

Xq=1.6424, Xq'=0.6168, Xq''=0.3253, Ra=0.002,

Tdo'=6.174s, Tdo''=0.032s, Tqo'=0.388s, Tqo''=0.047s

Zero sequence impedances in per unit values

Zero sequence resistance 0.002, reactance 0.2327

Neutral series resistance 1.0e5, reactance 0.0

Transformer parameters

Rated capacity 1MVA, Primary L-L RMS voltage 11kV, Secondary 11kV

Positive sequence resistance 0.0pu, reactance 0.0328pu

Zero sequence resistance 0.0pu, reactance 0.0033pu

Shunt conductance at TRF Primary 0.01pu

Large-time-step grid load Motor

Mechanical parameters

$H = 0.6s, D = 0.0\ (pu)$

Electrical parameters

$S_n = 2MVA$, $V_{rms,line} = 11kV$

in per units,

Turns ratio, rotor over stator 1.0

Ra=0.0425, Xa=0.0870, Xmd0=2.9745, Rfd=0.15, Xfd=0.0658,

Rkd=0.05, Xkd=0.0739, Xkf=0.0

Neutral resistance 5.0e4, reactance 0.0

VSC interface transformer, each of

$S_n = 1MVA$, L-L RMS voltage, $V_1 = 6.35kV$, $V_2 = 0.467kV$

Short circuit resistance 0.0pu, reactance 0.1pu

STATCOM

Main parameters

Interface resistance $R_a = 0.0\Omega$, inductance $L_a = 0.62mH$ (vary in different cases)

AC L-N RMS voltage 0.5kV, RMS line current 0.6kA

DC +ve to -ve capacitance 5.0mF, series resistance 0.0

Valve parameters

Valve ON resistance 0.001 Ohms, OFF resistance 5.0e4 Ohms

Snubber series capacitance 0.2uF, resistance 300 Ohms

AC filter

R=0.0566 Ohms, L=4.508uH, C=1.405mF

Small-time-step Motor with variable load

$H = 3.053s$, $D = 0.0\ (pu)$

$S_n = 0.4MVA$, $V_{rms,line} = 0.825kV$

in per units, Turns ratio, rotor over stator 1.0

Ra=0.00365, Xa=0.06, Xmd0=3.0, Rfd=0.004, Xfd=0.1203

Appendix B

Simulation parameters of the EF systems studied in Chapter 5.

Frequency of the system

$f_B = 50Hz$

Infinite grid model

$V_{rms,line} = 11kV$

R=1.187 Ohm, L=18.89mH, impedance angle 78.69 degree

VSC interface transformer, each of

$S_n = 1MVA$, L-L RMS voltage, $V_1 = 6.35kV$, $V_2 = 0.467kV$

Short circuit resistance 0.0pu, reactance 0.1pu

Induction generator, each of

$H = 2.0s$, $D = 0.0\ (pu)$

$S_n = 0.4MVA$, $V_{rms,line} = 0.825kV$

in per units,

Turns ratio, rotor over stator 1.0

Ra=0.00365, Xa=0.06, Xmd0=3.0, Rfd=0.004, Xfd=0.1203

Back-to-back converter

Grid-side parameters

Interface resistance $R_a = 0.001\Omega$, inductance $L_a = 0.62mH$

Valve ON resistance 0.001Ohm, OFF resistance 5.0kOhm

Snubber series capacitance 0.2mF, resistance 30.0Ohm

AC L-N RMS voltage 0.5kV, RMS line current 0.6kA

Machine-side parameters

Interface resistance $R_a = 0.001\Omega$, inductance $L_a = 0.11mH$

Valve ON resistance 0.001Ohm, OFF resistance 5.0kOhm

Snubber series capacitance 0.2mF, resistance 30.0Ohm

AC L-N RMS voltage 0.5kV, RMS line current 0.6kA

DC link

$C_{positive} = C_{negative} = 10.0mF$

The neutral point is grounded.

Flywheel storage system

Flywheel

Total inertia $H = 20.0s$

Permanent magnet synchronous machine

$S_n = 0.35MVA$, $V_{rms,line} = 0.825kV$

in per units,

Stator leakage reactance 0.008, Stator resistance 0.0037

D-axis magnet reactance 0.36, damper leakage reactance 0.05, damper R 0.035

Q-axis magnet reactance 0.36, damper leakage reactance 0.045, damper R 0.028

Magnetic strength 1.0

Initial rotor speed 0.8

Li-ion battery model

Series resistance 0.0001Ohm

Capacity of a single cell 0.85 Ah

SoC in a single cell 50%

Cell matrix, series x parallel: 10000 x 300

Appendix C

Simulation parameters of the wavefarm system studied in Chapter 6.

Frequency of the system

$f_B = 50Hz$

Infinite grid model

$V_{rms,line} = 11kV$

R=1.187 Ohm, L=18.89mH, impedance angle 78.69 degree

Undersea cable

Represented by a Π circuit

R=0.2328Ohm, L=1.07mH, C=0.325uF

VSC interface transformer, each of

$S_n = 1MVA$, L-L RMS voltage, $V_1 = 6.35kV$, $V_2 = 0.476kV$

Short circuit resistance 0.0pu, reactance 0.1pu

Capacitor bank at the high-voltage side of transformer

$C_{bank} = 11.5\ \mu F$, Δ-connection

Slave machine (induction generator)

$S_n = 0.4MVA$, $V_{rms,line} = 0.825kV$, $H = 3.053s$, $D = 0.0\ (pu)$

in per units,

Turns ratio, rotor over stator 1.0

Ra=0.00365, Xa=0.06, Xmd0=3.0, Rfd=0.004, Xfd=0.1203

Back-to-back converter

Grid-side parameters

Interface resistance $R_a = 0.001\Omega$, inductance $L_a = 0.62mH$

Valve ON resistance 0.001Ohm, OFF resistance 5.0kOhm

Snubber series capacitance 0.2mF, resistance 30.0Ohm

AC L-N RMS voltage 0.5kV, RMS line current 0.6kA

Machine-side parameters

Interface resistance $R_a = 0.001\Omega$, inductance $L_a = 0.11mH$

Valve ON resistance 0.001Ohm, OFF resistance 5.0kOhm

Snubber series capacitance 0.2mF, resistance 30.0Ohm

AC L-N RMS voltage 0.5kV, RMS line current 0.6kA

DC link

$C_{positive} = C_{negative} = 10.0mF$

The neutral point is grounded.

Master machine (PMSG)

$S_n = 0.35MVA$, $V_{rms,line} = 0.825kV$, $H = 21.15s$, $D = 0.0\ (pu)$

in per units,

Stator leakage reactance 0.008, Stator resistance 0.0037

D-axis magnet reactance 0.36, damper leakage reactance 0.05, damper R 0.035

Q-axis magnet reactance 0.36, damper leakage reactance 0.045, damper R 0.028

Magnetic strength 1.0

Zero initial conditions

Appendix D

Nomenclature of Table 5.2

u_C	Capacitor voltage
i_C	Capacitor current
C	Capacitance
i_L	Inductor current
u_L	Inductor voltage
L	Inductance
ω	Rotor speed
T	Torque
J	Flywheel inertia
p_C	Compressed air pressure
V_φ	Volume flow
N_A	Avogadro constant
V_0	Container volume
R	Gas constant
ρ_A	Gas density
T_A	Environmental temperature
h	Water height
G_φ	Gravity flow
ρ_w	Water density
g	Gravitational acceleration
S	Cross-sectional area